PHOTOTHERMAL PROPERTIES AND APPLICATIONS OF GOLD NANORODS

BY

JINGYU HUANG

DISSERTATION

Submitted in partial fulfillment of the requirements
for the degree of Doctor of Philosophy in Chemistry
in the Graduate College of the
University of Illinois at Urbana-Champaign, 2014

Urbana, Illinois

Doctoral Committee:

Professor Catherine J. Murphy, Chair and Director of Research
Professor David G. Cahill
Professor Alexander Scheeline
Associate Professor Ryan C. Bailey

ABSTRACT

Gold nanorods (GNRs) with their special optical and photothermal properties have attracted attention recently for their potential applications in fields such as photothermal therapy, drug delivery, biomedical imaging and chemical sensing. These anisotropic gold nanocrystals have tunable surface plasmonic resonance (SPR) bands ranging from the visible to the near infrared region. Their small dimensions of less than 100 nm and inert reactivity as well as the ease of surface functionalization facilitate their interaction with biological substances for various purposes. Before these GNR-based techniques can be applied in clinical use, there is still a large number of fundamental problems that need to be addressed to better align material properties with the desired application metrics. This thesis focuses on the fundamental photothermal and optical properties of GNRs when interacting with laser beams, which includes developing photothermal molecular release systems for drug delivery; investigating the nanoscale thermal transport properties at the solid-liquid interfaces; and studying the light emission induced by hot electron-hole pairs in GNRs.

In the first chapter, the colloidal synthetic strategy of GNRs, developed by the Murphy research group, and their optical and photothermal properties are introduced. The as-synthesized GNRs bear a bilayer of surfactant molecules cetyltrimethylammonium bromide (CTAB) on the surface and exhibit two SPR peaks ranging from 500 to 900 nm depending on the aspect ratio of the GNRs. The surface of the GNRs can be modified by different ligands or polyelectrolyte

layers in the aqueous environment. GNRs can also be immobilized on different substrates for further studies and applications.

In the second chapter, a light-controlled molecular release system was developed. Model drug molecules (dyes) were loaded within a variable number of polyelectrolyte multilayers wrapped around GNRs. A NIR continuous-wave (cw) laser was used to heat the global sample solution to release the dye molecules, which was detected using fluorescent signals from the dyes. The photo-induced release rate depended on the quantity and type of polyelectrolyte trapping layers and could be tuned by a factor of 100. Comparison of the photo-triggered molecular release rate to a pure thermal experiment provides an estimate of the effective temperature of the GNR solution upon irradiation.

In the third chapter, since knowledge of the spatiotemporal temperature distribution around a laser heated nanoparticle is essential for the study of photothermal therapeutics and the interface is playing an important role in controlling nanoscale heat transfer, a transient absorption method was used to investigate the thermal conductivity and heat capacity of surfactant and polyelectrolyte coatings of GNRs in aqueous solution, following femtosecond pumping of the longitudinal localized surface plasmons. Surfactant and polyelectrolyte layer thicknesses are measured by dynamic light scattering (DLS). The cooling dynamics of GNRs are best measured by tuning the pump-probe laser wavelength to the absorption peak of the sample solutions. The heat capacity and thermal conductivity were calculated numerically based on a cylindrical heat transfer model. It was found that the thermal properties have significant dependence on: (1) the

external surfactant critical micelle concentration for CTAB-capped GNRs; and (2) the charge of the terminal capping layer for polyelectrolyte-capped GNRs.

In the fourth chapter, light emission from plasmonic GNRs in aqueous suspensions was studied with cw and pulsed-laser excitation, which could be widely applied in biomedical imaging. Resonant secondary light emission contributes significantly to the background commonly observed in surface-enhanced Raman scattering (SERS) and to the light emission generated by pulsed-laser excitation of metallic nanostructures that is often attributed to two-photon luminescence. We proposed an electronic Raman scattering mechanism to describe the origin of the light emission quantitatively by comparing intensity of anti-Stokes emission excited by 785 nm cw and subpicosecond laser pulses. The result indicated that anti-Stokes emission is consistent with electronic Raman scattering by a high-temperature distribution of electronic excitations predicted by a two-temperature model.

In the last chapter, femtosecond pulsed laser induced photothermal release of molecules was explored with surface-enhanced Raman scattering techniques. Distance-dependent SERS enhancement factors were first studied by immobilizing Raman reporters on different spacer layers. Laser pulse-triggered molecular release was monitored by SERS signals, since the SERS signal decreased significantly with the distance from the GNR surface. It was found the SERS signal decreases with the average power of laser pulses and the irradiation time. However, it is observed that laser pulses could also induce severe photobleaching of the Raman reporters, which should be considered in drug delivery to prevent the damaging of drug molecules.

ACKNOWLEDGMENTS

The time has come to finish my five-year academic experience in the Department of Chemistry at the University of Illinois at Urbana-Champaign. Though all these years on the way to my PhD degree, there are people to whom I owe many thanks.

First and foremost, I would like to express my thanks to my research advisor Professor Catherine Murphy. Since I joined the Murphy research group in 2009, her support and guidance have helped me go through the doctoral research and professional training, which will also benefit me in my future career. It is my great honor to be a part of her research group.

I would like to present thanks to my co-advisor Professor David Cahill for his direction and advice. He hugely expanded my scientific research perspective and professional skills. I feel really proud to have had the chance to work with him.

I also want to thank my other committee members. Professor Ryan Bailey recruited me to the Analytical Chemistry Division at UIUC. Professor Alexander Scheeline trained me for scientific presentation and writing when I first came to the US. As committee members, they constantly provided support for my PhD development.

I also owe many thanks to the members of Murphy research group and Cahill research group for their help and encouragement. The comfortable environment they built is essential for me to accomplish the study and research here. I also learned various new skills and experienced teamwork in such groups.

For all these years in Illinois, I also feel very fortunate to have friends around to give academic suggestions as well as to bring more entertainment to my life. I want to thank them for the support of my everyday life.

Last but not least, I am extremely thankful and grateful to my family in China. I want to thank my parents for their selfless dedication through all these years. Their education about principles and criteria of life has been embedded in my mind since I was a little child. I also want to thank my sister for her care and understanding for me. The support of my family is the drive for me to persist in my academic career as well as my future career.

Jingyu Huang

University of Illinois at Urbana-Champaign

June 2014

TABLE OF CONTENTS

CHAPTER 1

INTRODUCTION

1.1 OPTICAL AND PHOTOTHERMAL PROPERTIES OF GOLD NANORODS

Colloidal gold nanoparticles with bright colors were discovered centuries ago. They were used for glass staining and decoration; the 4th-century Lycurgus Cup is one of the most famous examples of an early application.[1] With the recent development of science and technology, colloidal gold nanoparticles have been studied and applied in a wide variety of areas, including electronics, sensors, biomedical therapeutics and catalysis,[2–5] due to their unique optical, electronic, chemical and physical properties. The properties of gold nanoparticles can be tuned by changing the size, shape, surface chemistry, or aggregation state. Apart from the traditional spherical shape, nanorods[6], nanoshells[7], nanocages[8], nanoplates[9] etc. can be fabricated by various methods.

When the dimension of metallic nanoparticles become less than or comparable to the electron mean free path (~100 nm), new properties appear comparing to bulk materials because of the restriction of the electron motion. When the oscillating electric field of propagating light passes through a gold nanoparticle, the free conduction band electrons of gold oscillate in the particle.[10] This collective resonant oscillation of electrons confined in the nanoparticle is called the localized surface plasmon resonance (SPR). If the frequency of light matches the resonance frequency of the electrons, the nanoparticles can have strong absorption and scattering of light. Colloidal gold nanoparticles exhibit bright colors because of the light scattering and absorption,

and the color of the particles depends on the wavelength of SPR. For example: gold nanospheres with the diameter of 20 nm in aqueous solution with SPR band around 520 nm have ruby red color.

The surface plasmon resonance can be tuned by varying the size or shape of the nanoparticles, leading to particles with tailored optical properties for different applications. Gold nanorods (GNRs) with their anisotropic shape exhibit two SPR bands (Fig. 1.1): one is the transverse SPR, due to the electrons oscillating along the short axis; and the other is the longitudinal SPR that can be tuned from the visible to the near-infrared region by controlling the aspect ratio of the rods, due to the electrons oscillating along the long axis. These nanoparticle SPR positions can be calculated using methods based on the dipole approximation. While Mie theory was developed to calculate the optical cross-section of spherical nanoparticles, Gans theory was developed to explain that of ellipsoid particles.[11] The optical properties of gold nanorods with the shape between cylinders and ellipsoids can be approximately calculated with Gans theory.[10] The equations 1.1 to 1.5 describe the calculation of optical cross sections of gold nanorods:

$$\sigma_{abs} = \frac{2\pi V}{3\lambda} \varepsilon_m{}^{3/2} \sum_{j=a,b,c} \frac{(1/P_j{}^2)\varepsilon_2}{(\varepsilon_1 + (1-P_j)\varepsilon_m / P_j)^2 + \varepsilon_2{}^2} \tag{1.1}$$

$$\sigma_{sca} = \frac{8\pi^3}{9\lambda^4} \varepsilon_m^2 V^2 \sum_{j=a,b,c} \frac{(\varepsilon_1 - \varepsilon_m)^2 + \varepsilon_2^2 / (1/P_j^2)}{(\varepsilon_1 + (1-P_j)\varepsilon_m / P_j)^2 + \varepsilon_2^2} \tag{1.2}$$

$$\sigma_{ext} = \sigma_{abs} + \sigma_{sca} \tag{1.3}$$

where σ_{abs} is the absorption cross section, σ_{sca} is the scattering cross section, σ_{ext} is the extinction cross section, V is the volume of the particle, λ is the wavelength of light, ε_m is the media dielectric constant, ε_1 and ε_2 are the real and imaginary parts of gold dielectric constant, respectively. The depolarization factors P_j are defined by:

$$P_a = \left(\frac{1-e^2}{e^2}\right)\left\{\frac{1}{2e}\ln\left(\frac{1+e}{1-e}\right)-1\right\} \tag{1.4}$$

$$P_b = P_c = \frac{1-P_a}{2} \tag{1.5}$$

where a, b, and c are the three axes of the nanoparticle, a>b=c, $e=(1-(1/AR)^2)^{1/2}$, and AR is the aspect ratio of the GNRs. Thus, the absorption spectra change of GNRs can be affected by both the dielectric constants of gold and the surrounding media. The detailed calculation of absorption and scattering properties of gold nanoparticles of different size, shape, and composition can be found in the works of Link[12] and Jain[13].

After the absorption of photons by gold nanorods, most of the light energy is converted to heat energy through a series of photophysical processes at different time scales. This conversion of light into heat is what is meant by the phrase “the photothermal properties” of gold nanorods. The processes are demonstrated in Fig. 1.2. Initially, (1) when a gold nanorod is exposed to a femtosecond laser pulse, the laser light excites the plasmon resonance of electrons for the absorption of photons. The dephasing of oscillations in the conduction band happens at the time scale of 10 - 100 fs to form a non-thermal electron distribution. (2) Energy distributes through

electron-electron scattering to form a thermal electron distribution at the time scale of 100 fs - 1ps. (3) Electrons start to transfer energy to the gold lattice through electron-phonon coupling at the time scale of 1 - 10 ps. (4) Finally the gold lattice phonons dissipate the heat energy into the surroundings to raise the temperature around the particles at the time scale of 10 ps to 1 ns.[14,15] Heat energy generated by gold nanorods in the above processes is widely used in the current research of photothermal cancer therapy and drug delivery for biological and biomedical applications.[16–18] The mode of laser source also plays an important role for the temperature gradient around the laser-excited gold nanoparticles. When using a continuous-wave laser source, heat is generated in the gold lattice and dissipated into the environment continuously, thus there is no obvious temperature difference between the gold surface and the surroundings and the sample solution can be heated globally in the laser beam spots. When using a pulsed laser source, heat is generated and dissipated on short time scales in a periodic manner, thus the temperature gradient is localized around the nanoparticle and the transient temperature of the gold nanoparticle is significantly higher than its surroundings.[19]

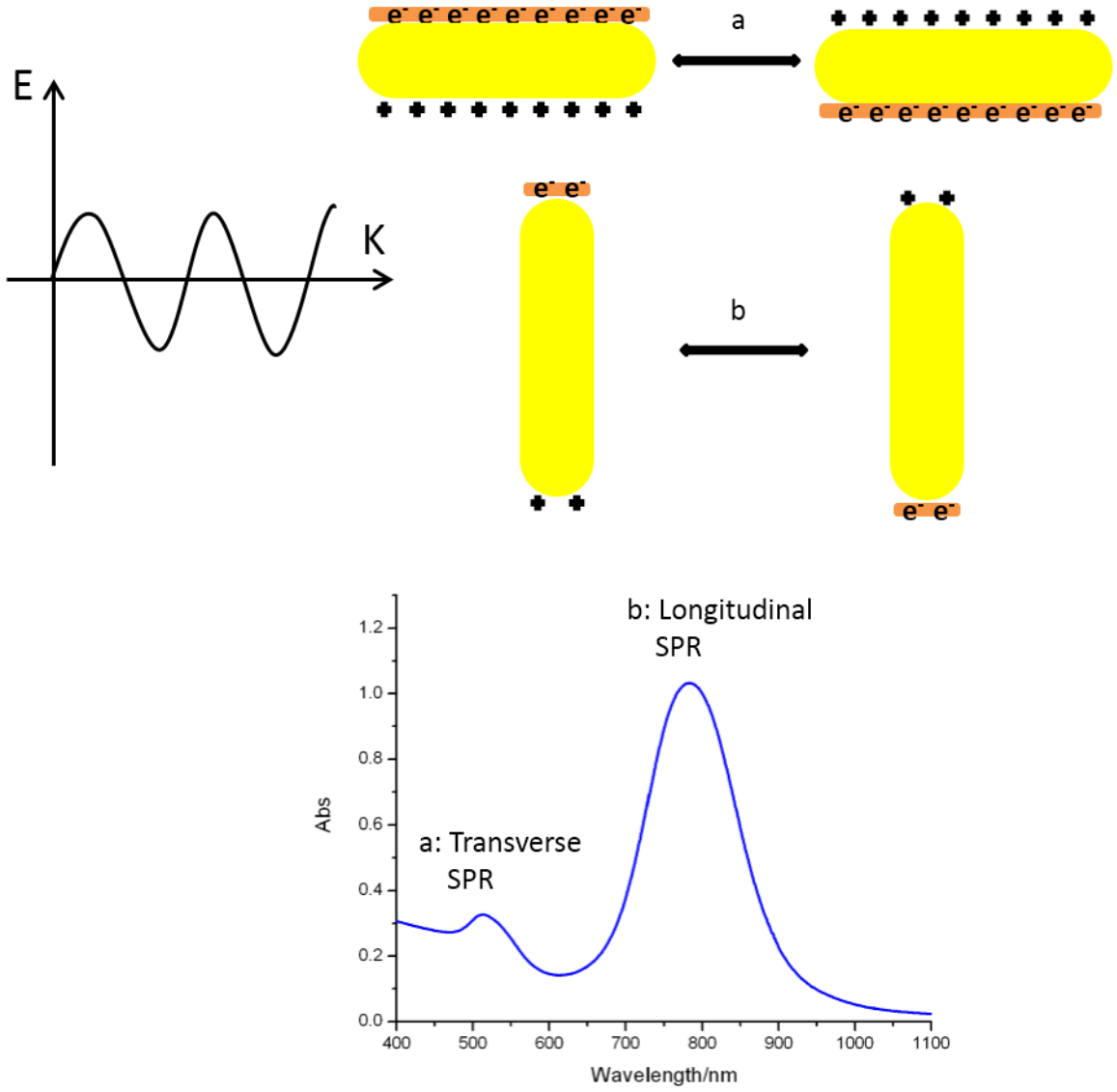

Figure 1.1 Surface plasmon resonance (SPR) of gold nanorod at the transverse and longitudinal bands. E is the electric field of the incident light; K is the propagation direction of the incident light. The conduction band electrons in GNR oscillate with the external electric field along (a) the short axis or (b) the long axis to generate (a) the transverse surface plasmon resonance around 520 nm or (b) the longitudinal surface plasmon resonance tunable from visible region to near-infrared region.[10]

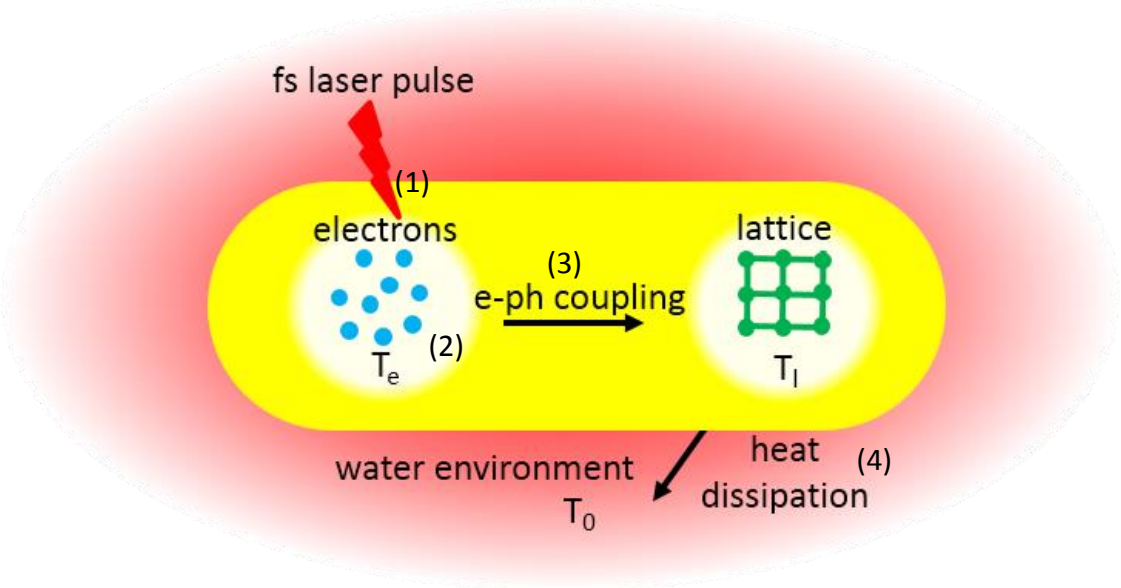

Figure 1.2 Photophysical processes of gold nanorod excited by a femtosecond (fs) laser pulse. (1) excitation of SPR in GNR by fs laser pulse and absorption of photos; (2) electron-electron scattering and heat distribution among electrons; (3) electron-phonon coupling and heat transfer from electrons to gold lattice; (4) heat dissipation from GNR to its surroundings.[14]

1.2 COLLOIDAL SYNTHESIS OF GOLD NANORODS

Gold nanorods synthesis in colloidal solution with the seed-mediated method is the expertise of the Murphy research group.[1,20] Seed-mediated growth protocol included the addition of small gold nanospherical seeds with diameter from 2-4 nm to growth solution consisting of gold salt, surfactant molecules and silver additives. In the growth solution, ascorbic acid first reduced $HAuCl_4$ to $HAuCl_2$ and further reduced $HAuCl_2$ to Au atoms with the addition of gold seeds which catalyzed the reduction reactions. Long GNRs (aspect ratio ~20)[6] and short GNRs (aspect ratio 1~4.5)[21] can be synthesized at high yield and monodispersity, and the method is easy to scale up for batch production at room temperature and aqueous solution conditions. For the short GNRs, the surfactant cetyltrimethylammonium bromide (CTAB, refer to Fig. 1.4c for the molecular structure) acts as a directing agent for GNRs growth, while the amount of silver nitrate as an additive can be used to tune the aspect ratio of the rods.[20] Gold nanorods exhibit two SPR bands: the transverse SPR at ~ 520 nm, and the longitudinal SPR is tunable from 520 nm to over 850 nm. The longitudinal SPR position can be red-shifted with the increasing aspect ratio of GNRs and the color of GNR colloids changes from pink to orange. However, it should be noticed that with the increasing length of GNR, the width actually decreases from over 20 nm to around 10 nm. (Fig. 1.3) There are quite a few different factors that can affect the final composition and dispersion of GNRs: the amount of gold salt, surfactants, ascorbic acid, silver nitrate; the tail lengths and the counter ions of the surfactant; the quality of gold seed, which can be affected further by the amount of sodium borohydride and aging time; even the water purity and temperature.[1,20,22] A slight change of any of the conditions can result in impurities and undesired polydispersity in the final products. All these factors should be carefully controlled in order to obtain the GNRs of desired sizes and dispersity with high reproducibility.

The growth dynamics of short GNRs have been studied by using UV-Vis absorption spectroscopy and transmission electron microscopy and the composition of the final GNRs have also been studied by ICP, EDX, and FTIR as well as many other techniques.[1,15,20] It was found that the GNRs grow fatter before becoming longer and the silver atoms also exist in GNRs with a thickness of about four atomic layers. The silver additive plays a critical role in the mechanism since, without the silver additive, gold nanoparticles with various shapes are obtained with low purity and large degrees of polydispersity. (Fig. 1.4) A recent study in which the Br^- in CTAB was replaced with potassium bromide for GNR growth also indicated the important role of Br^-.[22] Based upon all these findings, there are various hypotheses about the mechanism of rod-shaped single crystalline nanoparticle formation: from the early surfactant soft template mechanism to that of preferable binding of CTAB to a certain facet of gold seed, which can direct the growth direction of GNRs. Other mechanisms include: silver bromide complex formation on the surface, underpotential deposition of silver, electric-field-driving direction, and alloy formation.[1,10,20] More studies should be performed to unveil the contributions of each mechanism with developing spectroscopic and microscopic techniques to probe GNR growth *in situ*.[23–26]

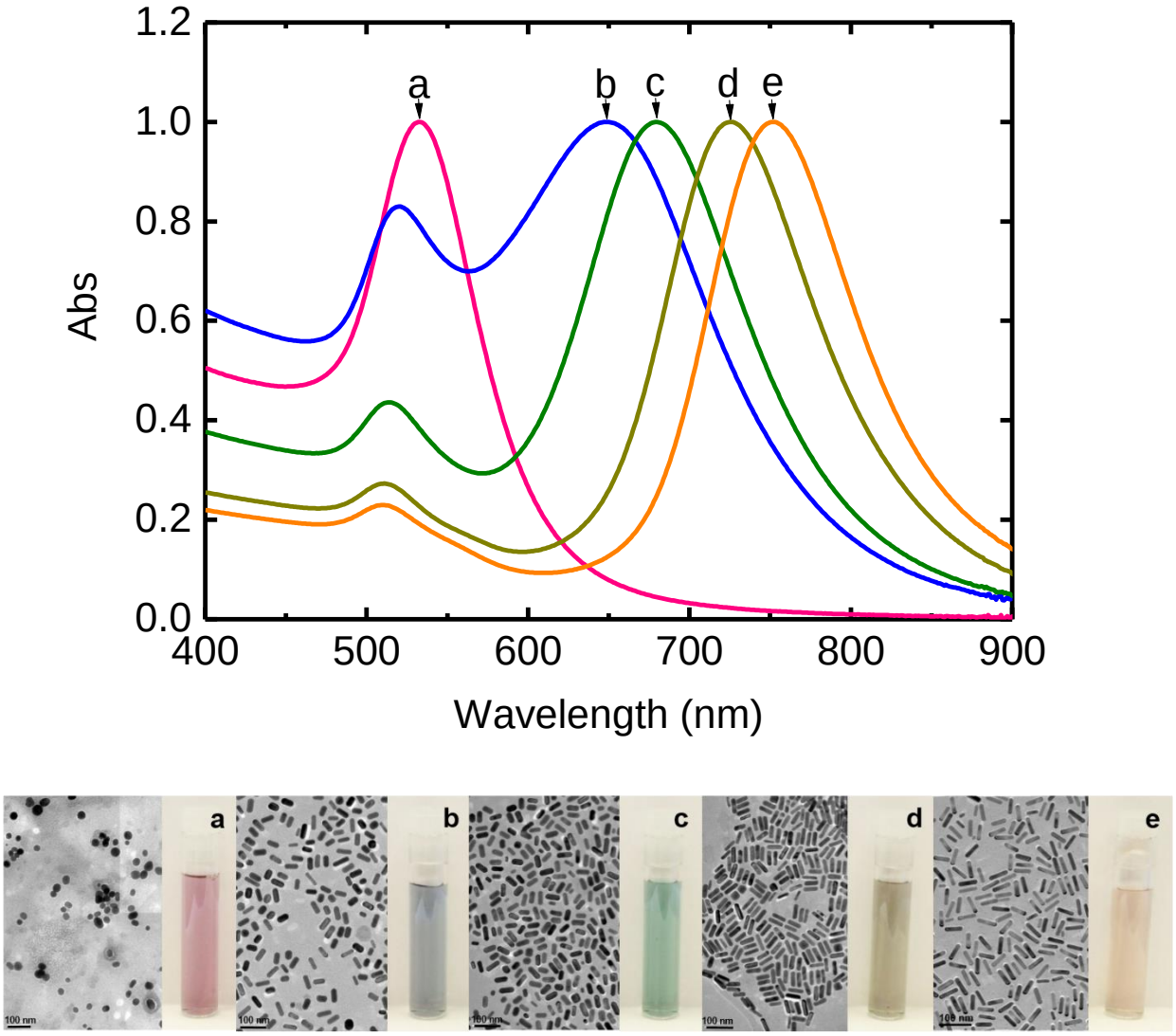

Figure 1.3 Properties of gold nanorods with different aspect ratios (AR) and surface plasmon resonance (SPR) positions. (a) AR=1.1, SPR=530 nm; (b) AR=2.3, SPR=648 nm; (c) AR=2.9, SPR=680 nm; (d) AR=3.4, SPR=721 nm; (e) AR=3.7, SPR=762 nm. (Top): normalized optical absorption spectra and (bottom) transmission electron micrographs with photographs of aqueous solutions of the nanoparticles. Scale bar=100 nm.

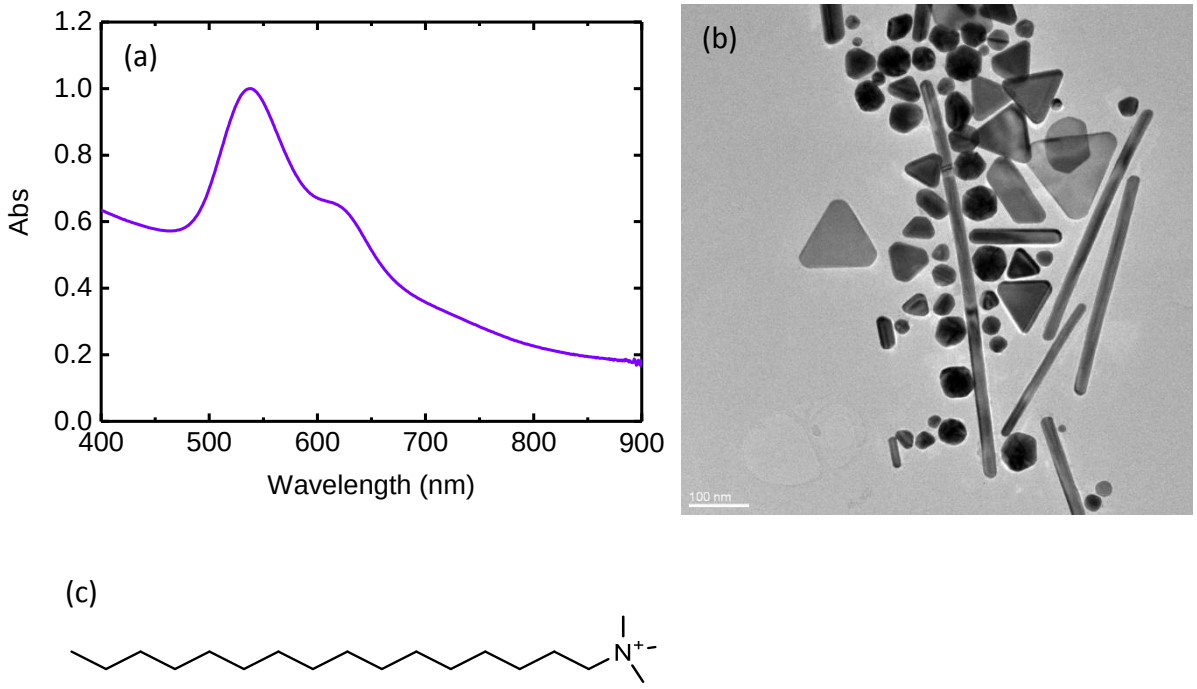

Figure 1.4 Gold nanocrystals synthesized with the seed-mediated method without the $AgNO_3$ additive. (a) optical absorption spectrum; (b) transmission electron micrograph. Scale bar = 100 nm. (c) molecular structure of surfactant cetyltrimethylammonium bromide (CTAB).

1.3 SURFACE MODIFICATION OF GOLD NANORODS

Gold nanorods synthesized with the above seed-mediated method have a bilayer of CTAB on their surface to ensure the separation and dispersion of GNRs in solutions.[27] The electrostatic interaction of CTAB with GNRs and the hydrophobic interaction between the tails in the CTAB bilayer can be easily destroyed by dilution to induce GNRs aggregation, which broadens and red-shifts the longitudinal SPR position.[28] Versatile surface chemistry of ligand exchange and polymer wrapping can be performed to enhance the stability of GNRs and to minimize aggregation. Moreover, the tertiary amine terminal group of CTAB is nearly inert to chemical reaction. Surface modification of GNRs is essential for their extensive use in chemical, biological and engineering application, so that the GNR surface can be loaded with drug molecules, functionalized by bio-recognition molecules and dispersed in different solvents.[29–32]

The surface of GNRs with the average dimension of 46 nm × 12 nm (aspect ratio ~4) can be modified by (a) CTAB concentration; (b) polyelectrolyte coating; (c) thiol-caboxylic acids; (d) thiol-poly(ethylene glycol). Techniques of UV-Vis optical absorption spectroscopy, ζ-potential measurement and dynamic light scattering (DLS) were used for the characterization of GNRs surface modification. (Fig 1.5 and Table 1.1) Optical absorption is used to study the refractive index change around GNRs; ζ-potential is used to characterize the surface charge of GNRs; DLS is used to detect the hydrodynamic diameters of GNRs. It is shown from the data that:

(a) Increasing the external CTAB concentration in the solution changes the structure or thickness of the CTAB bilayer on GNR surface. CTAB-GNRs start to aggregate after more than 2X purification by centrifugation. CTAB-GNRs can be stable for months in 1 mM external CTAB solution but only 2 weeks in <0.01 mM external CTAB solution.

(b) The positively charged CTAB-GNRs can be wrapped with polyelectrolytes (PELs) through layer-by-layer methods by mixing the GNRs with 10 mg/mL polyelectrolytes for 2 hours. Each coating cycle flips the surface charge and increases the thickness of the surface layers. The PEL-GNRs has higher stability in diluted solutions and at high temperatures compared to CTAB-GNRs.

(c) CTAB ligands that interact with the GNR through electrostatics can be exchanged by thiol-terminated ligands that can interact with GNR through Au-S covalent bonds. 3-mercaptopropionic acid (MPA) and 11-mercaptoundecanoic acid (MUA) are sample ligands that can replace CTAB in the aqueous solution environment. In this specific example, solution conditions of tri-borate-EDTA (TBE) buffer was chosen due to the high solubility of MPA and MUA in the solution. Replacement reactions are typically done according to protocols such as this one: if a GNR pellet of 100 μL with the external CTAB concentration ~1 mM is added into 3 mL TBE buffer with pH~8.4, severe aggregation of GNRs leads the solution to turn to a blue color, which indicates CTAB-GNRs in basic condition is not stable against aggregation. However, if the GNR pellet is added into 10 mM MPA or MUA in TBE buffer, ligand exchange takes place and no severe aggregation happens. The MUA-GNRs can be stable for over six months and can sustain for more than 3 purification cycles.

(d) On the other hand, ligand exchange can also happen in neutral aqueous solution by using ligands that contain polyethylene glycol (PEG) fractions to increase the ligand solubility in neutral water. $HS\text{-}CH_2CH_2\text{-}(OCH_2CH_2)_n\text{-}OCH_3$ (m-PEG-thiol M.W. 5000 g/mol) and $SH\text{-}C_{11}\text{-}(EG)_6\text{-}COOH$ are used to replace the CTAB by adding 100 μL GNR pellet into 2 mL 20 mg/mL ligands solution, followed by 15 min sonication and 48 hours of dialysis. The ligand

exchange is directly reflected by the surface charge of the GNRs from positive to neutral or negative. The m-PEG-GNRs is stable for over six months in neutral water, and COOH-$(EG)_6$-C_{11}-GNR can be kept stable in basic conditions.

Table 1.1 ζ-potential and Effective Translational Hydrodynamic Diameter of GNRs with Different Surface Coatings.

Sample	**ζ-potential (mV)**	**d_H (nm)**
GNR+CTAB	41.5 ±3.5	33.2 ±0.35
GNR+PAA	-38.6 ±2.9	33.4 ±0.15
GNR+PAA+PAH	35.1 ±3.1	44.0 ±0.29
GNR+MUA	-175 ±7.6	35.2 ±0.25
GNR+SH-PEG-m	-2.1 ±0.6	52.6 ±0.45
GNP+SH-C_{11}-$(EG)_6$+COOH	-78.2 ±5.0	34.6 ±0.31

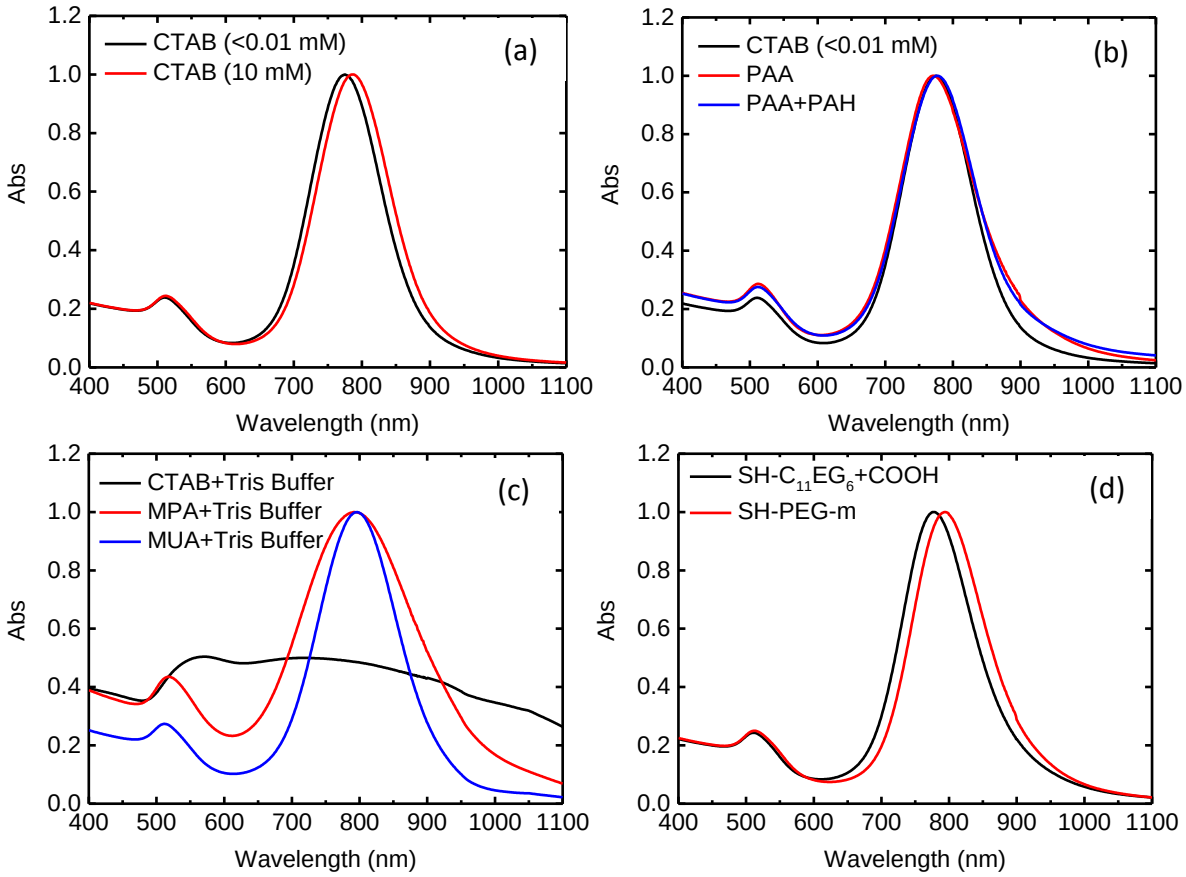

Figure 1.5 Optical absorption spectra of gold nanorods with various surface coatings. (a) GNRs with surfactant CTAB layers; (b) GNRs with polyelectrolyte layers; (c) GNRs with thiol-terminated carboxylic acids; (d) GNRs with thiol-terminated ethylene glycol molecules.

1.4 IMMOBILIZATION OF GOLD NANORODS

Gold nanoparticle synthesized with colloidal methods should be immobilized on substrates for the design of nanophotonic and nanoplasmonic devices. Self-assembly or directed-assembly of anisotropic gold nanorods in bulk or thin film materials through anisotropic surface modification on the sides or tips of the rods or through external mechanical or magnetic forces is a hot area in current research.[33–36] On the other side, in order to design the optical and electronic properties of gold nanorods, it is also essential to control the particle aggregation, which can result in a severe shift of SPR and can also generate "hot spots" for Raman scattering. These topics about particle assembly will not be discussed in this thesis. However, experiments of immobilizing gold nanorods on substrate with minimal aggregation and moderate surface coverage were done to study the thermal and plasmonic properties of an individual nanorod.

The CTAB-capped gold nanorods bear a positive charge on the surface, and it is hard to do chemical modification on the tertiary amine group at the end of CTAB. Thus, electrostatics is the simplest way to immobilize GNRs on substrates with regard to avoiding the step of ligand exchange. Piranha-treated quartz has -Si-O^- groups,[37] and a self-assembled monolayer of 4-mercaptobenzonic acid on a 100 nm Au film has –COO- groups,[38] both of which are negatively charged on the substrate surface that can interact with the $–NH_3^+$ on the GNR surface. The procedure generally includes the immersion of the substrate in 2 nM GNR solutions for 2 hours, then the substrate is washed with water and ethanol alternatively to get rid of the excess of GNRs, and finally the coated substrate is dried gently in nitrogen flows. To control the surface coverage of GNRs on the substrate, the factors of GNRs solution concentration, immersion time and the quality of the SAM should be carefully dealt with. The other critical factor is the external concentration of CTAB molecules in the GNRs solution. If the CTAB concentration is too high,

the extra CTAB molecules can block the negative charge spots on the substrate to reduce the possibility of GNRs immobilization; if the CTAB concentration is too low, GNR aggregation can happen in solution and the surface charge of GNR should also be reduced. In the scanning electron micrographs, an external CTAB concentration of 0.1 nm and GNR concentration of 2 nM were chosen for the sample preparation.

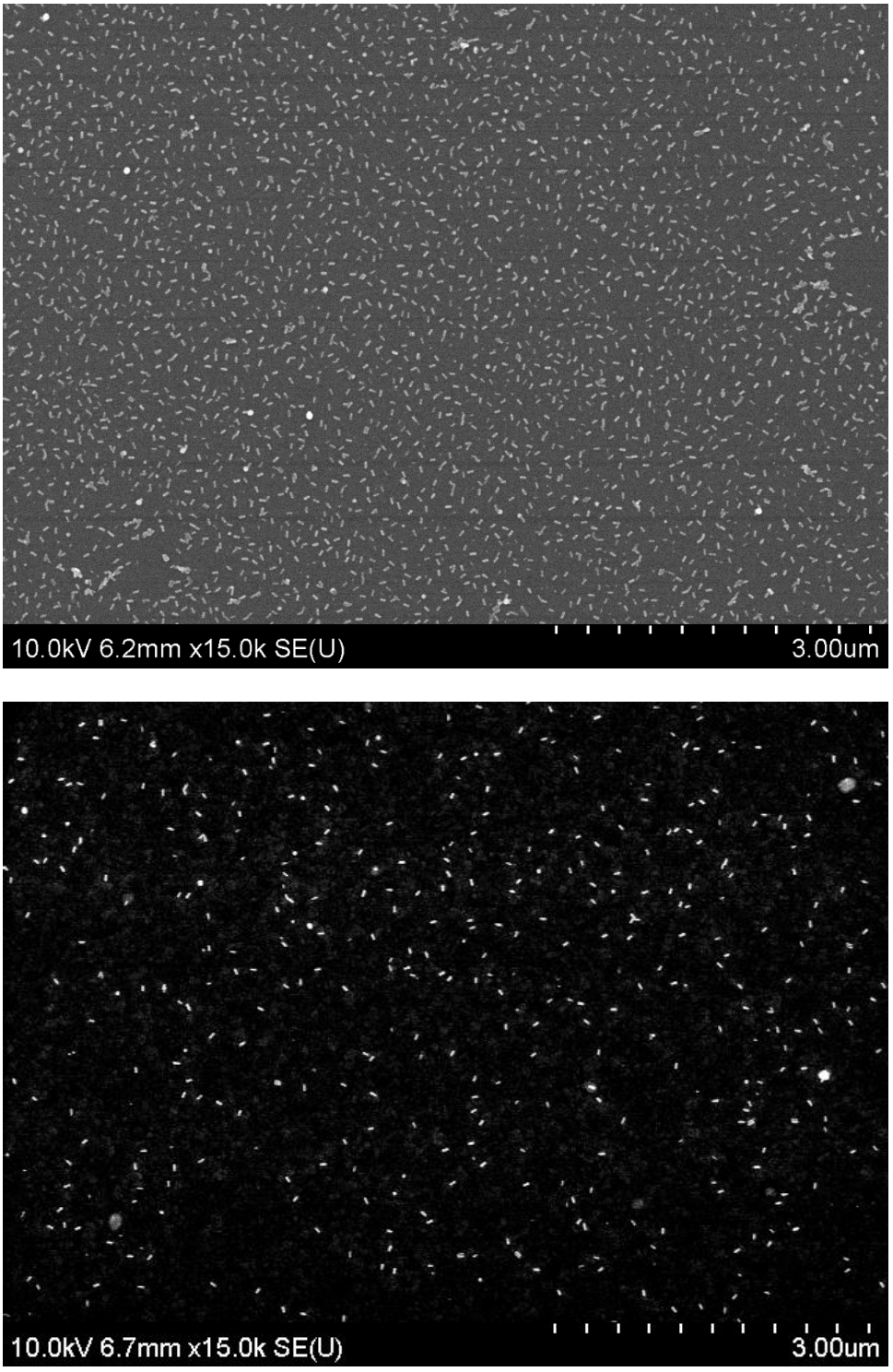

Figure 1.6 Scanning electron micrographs of gold nanorods immobilized on (a) single crystalline quartz (b) a 4-mercaptobenzonic acid monolayer on a 100 nm Au thin film.

1.5 TIME-RESOLVED ABSORPTION AND ANTI-STOKES RAMAN SCATTERING SPECTROSCOPY FOR THERMAL TRANSPORT STUDY

For this thesis, time-resolved spectroscopy apparatuses were built based upon mode-locked pump-probe laser systems. (Fig. 1.7) The transient absorption technique detects the absorption signal change of samples upon laser excitation, and it has been used in various studies to measure properties of electron dynamics, energy transfer and chemical reactions.[14,39–41] In the case of thermal properties, the sample temperature change is directly reflected in the absorption signal change. Time-resolved anti-Stokes Raman (see section 1.6) spectroscopy[42–45] has also been developed for the study of vibrational states, which is based on the fact that the population of anti-Stokes vibrational states follows the Bose-Einstein distribution[46] that is related to the local temperature of the sample molecules.

The instrumental setup of the time-resolved spectroscopy consists of a pump and a probe beam with delay time intervals controlled by a translation stage.[44] Events at a certain delay time after the pump beam excitations can thus be detected using the probe beam, since absorption and Raman scattering are both instantaneous upon light interaction.

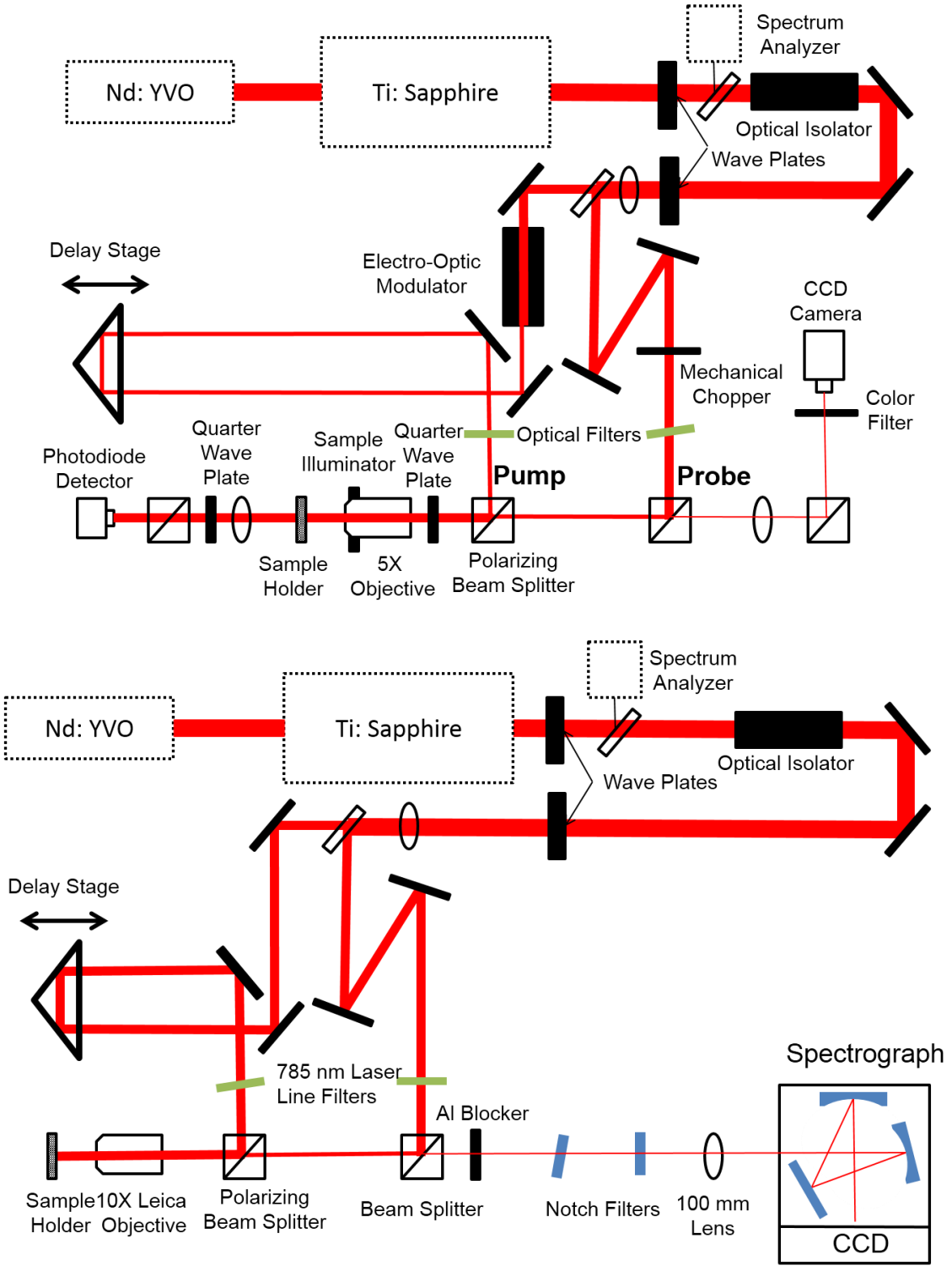

Figure 1.7 Top: transient absorption setup; Bottom: time-resolved Raman spectroscopy setup.

1.6 SURFACE-ENHANCED RAMAN SCATTERING

Raman scattering is a phenomenon of inelastic scattering of a photon. When a photon interacts with a molecule, it produces an oscillating polarization in the molecule and excites it to a virtual energy state. The oscillating polarization can or cannot couple with other vibrational excitations in the molecule. (Fig. 1.8) If there is no coupling, the scattered photon has the same energy as the original photon and the molecule stays in same vibrational state; this type of elastic scattering is called Rayleigh scattering. If there is coupling, the scattered photon has a different energy as the original photon and the molecule changes to higher (Stokes Raman scattering) or lower (anti-Stokes Raman scattering) vibrational state.[47]

Raman scattering of molecules adsorbed on rough metal surface or plasmonic nanostructures can be enhanced significantly, which is called surface-enhanced Raman scattering (SERS). The enhancement factor can be as much as 10^7 to 10^8 in solution and 10^{10} to 10^{11} on substrates. There are mainly two theories being proposed for the enhancement mechanisms: the electromagnetic theory related to localized SPR and the chemical theory related to charge transfer. In the case of molecules adsorbed on a gold nanorod surface through non-covalent bonds, the electric field of plasmonic gold nanoparticles can be greatly enhanced by localized surface plasmon resonance oscillation by orders of magnitude, while the chemical theory cannot be applied.[48,49] Raman scattering from molecules on the gold nanorod surface can be dramatically increased because the intensity is proportional to the square of the electromagnetic field magnitude. The signal intensity of SERS can be described in the following equation[50]:

$$S_{SERS} \propto nI_{inc} g_{inc}^2 g_{sca}^2 \sigma_{Raman} \quad (1.6)$$

where S_{SERS} is intensity of the surface-enhanced Raman scattering of the adsorbed molecule, n is the population distribution of the vibrational modes at a certain energy, I_{inc} is the intensity of incident light, g_{inc} is the enhancement factor from electromagnetic field of the incident light, g_{sca} is the enhancement factor from electromagnetic field of the scattered light, σ_{Raman} is the Raman cross-section of the adsorbed molecules.

The strong scattering from these molecules enhanced by nanoparticles greatly increases functionality of Raman scattering in optical spectroscopy detection and microscopy imaging applications, which can even extend to the probing of single molecules.[51,52]

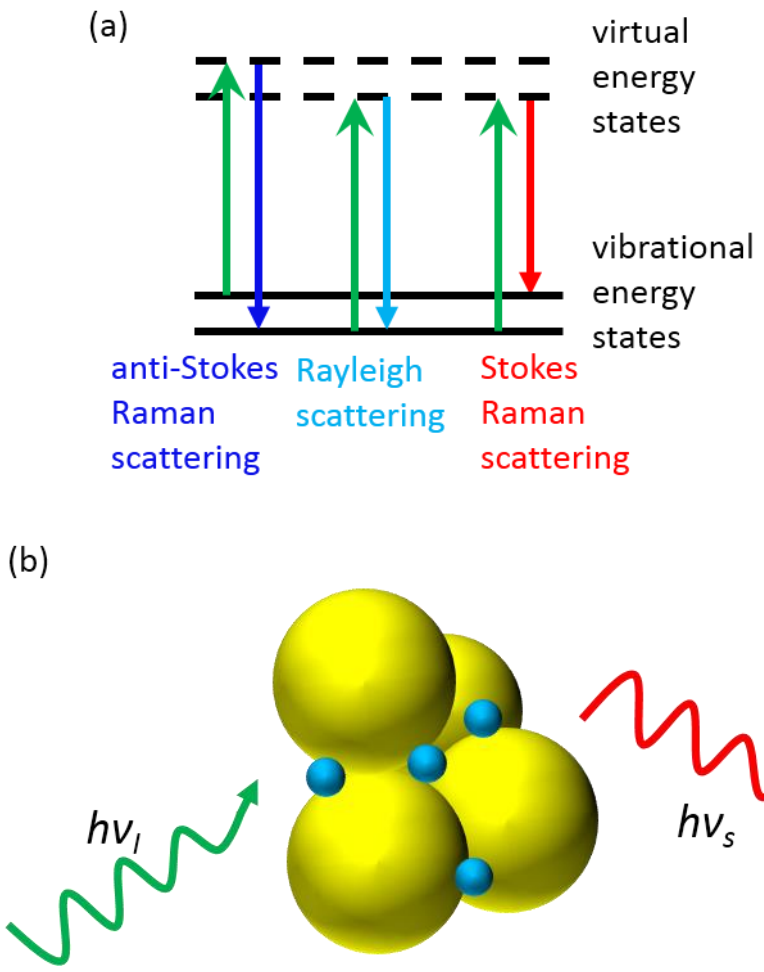

Figure 1.8 (a) Diagram of Stokes, anti-Stokes Raman scattering and Rayleigh scattering mechanisms. (b) Scheme of surface-enhanced Raman scattering: yellow spheres represent gold nanoparticles; blue spheres represent Raman reporter molecules; green arrow represents incident light and red arrow represents scattered light.

1.7 REFERENCES

1. Murphy, C. J.; Sau, T. K.; Gole, A. M.; Orendorff, C. J.; Gao, J.; Gou, L.; Hunyadi, S. E.; Li, T. Anisotropic Metal Nanoparticles: Synthesis, Assembly, and Optical Applications. *J. Phys. Chem. B* **2005**, *109*, 13857–13870.
2. Cai, W.; Gao, T.; Hong, H.; Sun, J. Applications of Gold Nanoparticles in Cancer Nanotechnology. *Nanotechnol. Sci. Appl.* **2008**, *2008*.
3. Sperling, R. A.; Gil, P. R.; Zhang, F.; Zanella, M.; Parak, W. J. Biological Applications of Gold Nanoparticles. *Chem. Soc. Rev.* **2008**, *37*, 1896–1908.
4. Saha, K.; Agasti, S. S.; Kim, C.; Li, X.; Rotello, V. M. Gold Nanoparticles in Chemical and Biological Sensing. *Chem. Rev.* **2012**, *112*, 2739–2779.
5. Dykman, L.; Khlebtsov, N. Gold Nanoparticles in Biomedical Applications: Recent Advances and Perspectives. *Chem. Soc. Rev.* **2012**, *41*, 2256–2282.
6. Jana, N. R.; Gearheart, L.; Murphy, C. J. Wet Chemical Synthesis of High Aspect Ratio Cylindrical Gold Nanorods. *J. Phys. Chem. B* **2001**, *105*, 4065–4067.
7. Hirsch, L. R.; Stafford, R. J.; Bankson, J. A.; Sershen, S. R.; Rivera, B.; Price, R. E.; Hazle, J. D.; Halas, N. J.; West, J. L. Nanoshell-Mediated near-Infrared Thermal Therapy of Tumors under Magnetic Resonance Guidance. *Proc. Natl. Acad. Sci. U. S. A.* **2003**, *100*, 13549–13554.
8. Yavuz, M. S.; Cheng, Y.; Chen, J.; Cobley, C. M.; Zhang, Q.; Rycenga, M.; Xie, J.; Kim, C.; Song, K. H.; Schwartz, A. G.; *et al.* Gold Nanocages Covered by Smart Polymers for Controlled Release with near-Infrared Light. *Nat. Mater.* **2009**, *8*, 935–939.

9. Shao, Y.; Jin, Y. D.; Dong, S. J. Synthesis of Gold Nanoplates by Aspartate Reduction of Gold Chloride. *Chem. Commun.* **2004**, 1104–1105.

10. Huang, X.; Neretina, S.; El-Sayed, M. A. Gold Nanorods: From Synthesis and Properties to Biological and Biomedical Applications. *Adv. Mater.* **2009**, *21*, 4880–4910.

11. Link, S.; El-Sayed, M. A. Shape and Size Dependence of Radiative, Non-Radiative and Photothermal Properties of Gold Nanocrystals. *Int. Rev. Phys. Chem.* **2000**, *19*, 409–453.

12. Link, S.; Mohamed, M. B.; El-Sayed, M. A. Simulation of the Optical Absorption Spectra of Gold Nanorods as a Function of Their Aspect Ratio and the Effect of the Medium Dielectric Constant. *J. Phys. Chem. B* **1999**, *103*, 3073–3077.

13. Jain, P. K.; Lee, K. S.; El-Sayed, I. H.; El-Sayed, M. A. Calculated Absorption and Scattering Properties of Gold Nanoparticles of Different Size, Shape, and Composition: Applications in Biological Imaging and Biomedicine. *J. Phys. Chem. B* **2006**, *110*, 7238–7248.

14. Hartland, G. V. Optical Studies of Dynamics in Noble Metal Nanostructures. *Chem. Rev.* **2011**, *111*, 3858–3887.

15. Huang, X.; Neretina, S.; El-Sayed, M. A. Gold Nanorods: From Synthesis and Properties to Biological and Biomedical Applications. *Adv. Mater.* **2009**, *21*, 4880–4910.

16. Dreaden, E. C.; Alkilany, A. M.; Huang, X.; Murphy, C. J.; El-Sayed, M. A. The Golden Age: Gold Nanoparticles for Biomedicine. *Chem. Soc. Rev.* **2012**, *41*, 2740–2779.

17. Pérez-Juste, J.; Pastoriza-Santos, I.; Liz-Marzán, L. M.; Mulvaney, P. Gold Nanorods: Synthesis, Characterization and Applications. *Coord. Chem. Rev.* **2005**, *249*, 1870–1901.

18. Alkilany, A. M.; Thompson, L. B.; Boulos, S. P.; Sisco, P. N.; Murphy, C. J. Gold Nanorods: Their Potential for Photothermal Therapeutics and Drug Delivery, Tempered by the Complexity of Their Biological Interactions. *Adv. Drug Deliv. Rev.* **2012**, *64*, 190–199.

19. Keblinski, P.; Cahill, D. G.; Bodapati, A.; Sullivan, C. R.; Taton, T. A. Limits of Localized Heating by Electromagnetically Excited Nanoparticles. *J. Appl. Phys.* **2006**, *100*, 054305.

20. Murphy, C. J.; Thompson, L. B.; Chernak, D. J.; Yang, J. A.; Sivapalan, S. T.; Boulos, S. P.; Huang, J.; Alkilany, A. M.; Sisco, P. N. Gold Nanorod Crystal Growth: From Seed-Mediated Synthesis to Nanoscale Sculpting. *Curr. Opin. Colloid Interface Sci.* **2011**, *16*, 128–134.

21. Sau, T. K.; Murphy, C. J. Seeded High Yield Synthesis of Short Au Nanorods in Aqueous Solution. *Langmuir* **2004**, *20*, 6414–6420.

22. Lohse, S. E.; Burrows, N. D.; Scarabelli, L.; Liz-Marzán, L. M.; Murphy, C. J. Anisotropic Noble Metal Nanocrystal Growth: The Role of Halides. *Chem. Mater.* **2014**, *26*, 34–43.

23. Polte, J.; Erler, R.; Thünemann, A. F.; Sokolov, S.; Ahner, T. T.; Rademann, K.; Emmerling, F.; Kraehnert, R. Nucleation and Growth of Gold Nanoparticles Studied via in Situ Small Angle X-Ray Scattering at Millisecond Time Resolution. *ACS Nano* **2010**, *4*, 1076–1082.

24. Becker, J.; Schubert, O.; Sönnichsen, C. Gold Nanoparticle Growth Monitored in Situ Using a Novel Fast Optical Single-Particle Spectroscopy Method. *Nano Lett.* **2007**, *7*, 1664–1669.

25. Koerner, H.; MacCuspie, R. I.; Park, K.; Vaia, R. A. In Situ UV/Vis, SAXS, and TEM Study of Single-Phase Gold Nanoparticle Growth. *Chem. Mater.* **2012**, *24*, 981–995.

26. Sardar, R.; Shumaker-Parry, J. S. Spectroscopic and Microscopic Investigation of Gold Nanoparticle Formation: Ligand and Temperature Effects on Rate and Particle Size. *J. Am. Chem. Soc.* **2011**, *133*, 8179–8190.

27. Murphy, C. J.; Thompson, L. B.; Alkilany, A. M.; Sisco, P. N.; Boulos, S. P.; Sivapalan, S. T.; Yang, J. A.; Chernak, D. J.; Huang, J. The Many Faces of Gold Nanorods. *J. Phys. Chem. Lett.* **2010**, *1*, 2867–2875.

28. Huang, J.; Park, J.; Wang, W.; Murphy, C. J.; Cahill, D. G. Ultrafast Thermal Analysis of Surface Functionalized Gold Nanorods in Aqueous Solution. *ACS Nano* **2013**, *7*, 589–597.

29. Zhou, J.; Ralston, J.; Sedev, R.; Beattie, D. A. Functionalized Gold Nanoparticles: Synthesis, Structure and Colloid Stability. *J. Colloid Interface Sci.* **2009**, *331*, 251–262.

30. Sperling, R. A.; Parak, W. J. Surface Modification, Functionalization and Bioconjugation of Colloidal Inorganic Nanoparticles. *Philos. Trans. R. Soc. Math. Phys. Eng. Sci.* **2010**, *368*, 1333–1383.

31. Nativo, P.; Prior, I. A.; Brust, M. Uptake and Intracellular Fate of Surface-Modified Gold Nanoparticles. *ACS Nano* **2008**, *2*, 1639–1644.

32. Perrault, S. D.; Chan, W. C. W. Synthesis and Surface Modification of Highly Monodispersed, Spherical Gold Nanoparticles of 50−200 Nm. *J. Am. Chem. Soc.* **2009**, *131*, 17042–17043.

33. Lee, C. H.; Tian, L.; Abbas, A.; Kattumenu, R.; Singamaneni, S. Directed Assembly of Gold Nanorods Using Aligned Electrospun Polymer Nanofibers for Highly Efficient SERS Substrates. *Nanotechnology* **2011**, *22*, 275311.

34. Pan, D.; Pramanik, M.; Senpan, A.; Wickline, S. A.; Wang, L. V.; Lanza, G. M. A Facile Synthesis of Novel Self-Assembled Gold Nanorods Designed for Near-Infrared Imaging. *J. Nanosci. Nanotechnol.* **2010**, *10*, 8118–8123.

35. Vigderman, L.; Khanal, B. P.; Zubarev, E. R. Functional Gold Nanorods: Synthesis, Self-Assembly, and Sensing Applications. *Adv. Mater.* **2012**, *24*, 4811–4841.

36. Peng, B.; Li, G.; Li, D.; Dodson, S.; Zhang, Q.; Zhang, J.; Lee, Y. H.; Demir, H. V.; Yi Ling, X.; Xiong, Q. Vertically Aligned Gold Nanorod Monolayer on Arbitrary Substrates: Self-Assembly and Femtomolar Detection of Food Contaminants. *ACS Nano* **2013**, *7*, 5993–6000.

37. Park, J.; Huang, J.; Wang, W.; Murphy, C. J.; Cahill, D. G. Heat Transport between Au Nanorods, Surrounding Liquids, and Solid Supports. *J. Phys. Chem. C* **2012**, *116*, 26335–26341.

38. Sisco, P. N.; Murphy, C. J. Surface-Coverage Dependence of Surface-Enhanced Raman Scattering from Gold Nanocubes on Self-Assembled Monolayers of Analyte†. *J. Phys. Chem. A* **2009**, *113*, 3973–3978.

39. Inouye, H.; Tanaka, K.; Tanahashi, I.; Hirao, K. Ultrafast Dynamics of Nonequilibrium Electrons in a Gold Nanoparticle System. *Phys. Rev. B* **1998**, *57*, 11334–11340.

40. Link, S.; Burda, C.; Wang, Z. L.; El-Sayed, M. A. Electron Dynamics in Gold and Gold–silver Alloy Nanoparticles: The Influence of a Nonequilibrium Electron Distribution and the Size Dependence of the Electron–phonon Relaxation. *J. Chem. Phys.* **1999**, *111*, 1255–1264.

41. Jain, P. K.; Qian, W.; El-Sayed, M. A. Ultrafast Electron Relaxation Dynamics in Coupled Metal Nanoparticles in Aggregates. *J. Phys. Chem. B* **2006**, *110*, 136–142.

42. Letcher, J. J.; Kang, K.; Cahill, D. G.; Dlott, D. D. Effects of High Carrier Densities on Phonon and Carrier Lifetimes in Si by Time-Resolved Anti-Stokes Raman Scattering. *Appl. Phys. Lett.* **2007**, *90*, 252104.

43. Kang, K.; Ozel, T.; Cahill, D. G.; Shim, M. Optical Phonon Lifetimes in Single-Walled Carbon Nanotubes by Time-Resolved Raman Scattering. *Nano Lett.* **2008**, *8*, 4642–4647.

44. Kang, K.; Koh, Y. K.; Chiritescu, C.; Zheng, X.; Cahill, D. G. Two-Tint Pump-Probe Measurements Using a Femtosecond Laser Oscillator and Sharp-Edged Optical Filters. *Rev. Sci. Instrum.* **2008**, *79*, 114901.

45. Kang, K.; Abdula, D.; Cahill, D. G.; Shim, M. Lifetimes of Optical Phonons in Graphene and Graphite by Time-Resolved Incoherent Anti-Stokes Raman Scattering. *Phys. Rev. B* **2010**, *81*, 165405.

46. Klein, M. V. Electronic Raman Scattering. In *Theory of Light Scattering in Condensed Matter*; Bendow, B.; Birman, J. L.; Agranovich, V. M., Eds.; Springer US, 1976; pp. 461–473.

47. Ferraro, J. R.; Nakamoto, K.; Brown, C. W. Chapter 1 - Basic Theory. In *Introductory Raman Spectroscopy (Second Edition)*; Ferraro, J. R.; Nakamoto, K.; Brown, C. W., Eds.; Academic Press: San Diego, 2003; pp. 1–94.

48. Campion, A.; Kambhampati, P. Surface-Enhanced Raman Scattering. *Chem. Soc. Rev.* **1998**, *27*, 241–250.

49. Vo-Dinh, T. Surface-Enhanced Raman Spectroscopy Using Metallic Nanostructures. *Trac-Trends Anal. Chem.* **1998**, *17*, 557–582.

50. Kneipp, J.; Kneipp, H.; Kneipp, K. SERS - a Single-Molecule and Nanoscale Tool for Bioanalytics. *Chem. Soc. Rev.* **2008**, *37*, 1052–1060.

51. Kneipp, K.; Wang, Y.; Kneipp, H.; Perelman, L. T.; Itzkan, I.; Dasari, R.; Feld, M. S. Single Molecule Detection Using Surface-Enhanced Raman Scattering (SERS). *Phys. Rev. Lett.* **1997**, *78*, 1667–1670.

52. Nie, S. M.; Emery, S. R. Probing Single Molecules and Single Nanoparticles by Surface-Enhanced Raman Scattering. *Science* **1997**, *275*, 1102–1106.

CHAPTER 2

POLYELECTROLYTE WRAPPING LAYERS CONTROL RATES OF PHOTOTHERMAL MOLECULAR RELEASE FROM GOLD NANORODS

2.1 INTRODUCTION

The unique optical properties and tunable sizes of gold nanorods have made them attractive materials for research over the last decade. Due to their anisotropic shape, gold nanorods display two plasmon resonance bands that arise from the collective oscillation of conduction-band electrons, one along the transverse axis of the rods and another along the longitudinal axis. This oscillation results in strong absorption of light at tunable wavelengths, in the visible and near-infrared regions, that depend on nanorod shape.[1] The absorbed light undergo nonradiative decay processes and thereby be converted to heat, and the resulting temperature rise affects not only the gold nanorods but also their surrounding environment.[2]

Gold nanorods with "confined" thermal effects show great potential for a wide variety of biological applications, including photothermal therapy via cell ablation[3–9] and photothermally activated drug and gene delivery.[10–16] The small size of the gold nanorods compared to typical cells (10-100 nm for the rods, compared to many microns for cells), coupled with the relative ease of nanorod surface functionalization, suggests that there is much promise for using gold nanorods as drug carriers for controlled release systems.[17,18] Near-infrared (NIR) laser

Part of this chapter is reprinted with permission from Jingyu Huang, Kaliah S. Jackson and Catherine J. Murphy, *Nano Lett.*, **2012**, *12* (6), pp 2982–2987. (DOI: 10.1021/nl3007402)

irradiation-triggered drug release is especially attractive, because this is the "water window" of tissue (~800-1200 nm), and gold nanorods can easily be made to absorb in this window.[19]

Gold nanoparticles of various shapes including nanorods,[10–16] nanospheres,[20–27] nanoshells[15,28,29] and nanocages[30–32] have been used for photothermal drug release using either pulsed lasers or continuous wave lasers. Pulsed laser heating can generate a large transient temperature increase in the picosecond time scale, and high release rates of the drugs from the gold particles. When the laser power is high enough, the particles can even melt.[2,17] However, high temperatures can also denature the drug molecules bound to the surface of the particles, and so careful adjustment of various parameters are necessary to ensure that the proper and desired molecular release truly occurs. Continuous wave lasers more typically raise the temperature of the particles and surrounding bath slowly, without causing molecular damage, although the release rate may thus be slowed.

In this work, rhodamine 6G was used as a model "drug" and was incorporated into polyelectrolyte multilayers around gold nanorods, as a function of the number of outer capping layers. A NIR continuous wave laser was used to gently heat the samples and trigger the release of the dye molecules through the trapping layers. The molecular release rate by laser heating was quantitatively examined as a function of multilayer number and type. We find that release can be shut off if only several polymer layers overcoat dye-modified nanorods.

2.2 RESULTS AND DISCUSSION

Gold nanorods (GNRs) with aspect ratio 3.6 were synthesized using a seed-mediated silver-assisted approach with cetyltrimethylammonium bromide (CTAB) surfactant in aqueous solution.[33] Nanorods were then purified by centrifugation and characterized with electronic absorption spectroscopy, zeta potential measurements and transmission electron microscopy (TEM). The nanorods, 57 nm × 16 nm, exhibited a maximum plasmon peak at 770 nm and bore a positive surface charge due to the CTAB bilayer on the surface. The GNR surface was further modified with layer-by-layer polyelectrolyte coating.[34] In neutral aqueous solutions, negatively charged poly(acrylic acid, sodium salt) (PAA) and positively charged poly(allylamine hydrochloride) (PAH) were used to alter the surface charge of the rods and also to electrostatically trap the dye molecules.

In order to absorb the positively-charged R6G on the surface of the as-made GNRs, an anionic PAA polymer layer was first coated onto the rods by mixing 1 mL of a 1 nM GNR solution with 0.1 mL of 10 mM NaCl and 0.2 mL of 10 mg/mL PAA (MW 150,000 g/mol) in a centrifuge tube for 2 hours. Excess polyelectrolyte was removed by centrifugation and the pellets were re-dispersed in 1 mL water. A 20 μL aliquot of a 1 mM R6G solution was added into the GNR+PAA solution, and allowed to stand overnight to form PAA-R6G complexes. Excess dye was removed by centrifugation and the GNR-polyelectrolyte-dye pellets were dispersed in 1 mL water. Additional polyelectrolyte layer-by-layer coatings were added as “trapping” layers by mixing 1 mL sample solution with 0.1 mL of 10 mM NaCl and 0.2 mL of 10 mg/mL PAA or

PAH (MW 15,000 g/mol). The final sample solution was spun down to remove the extra unbound polyelectrolytes and dispersed in DI water. The samples with different trapping layers were shown in Scheme 2.1:

(GNR+PAA+R6G+PAA)

(GNR+PAA+R6G+PAA+PAH)

(GNR+PAA+R6G+PAA+PAH+PAA)

(GNR+PAA+R6G+PAH)

(GNR+PAA+R6G+PAH+PAA).

Isothermal titration calorimetry of R6G with PAA (Figure 2.1) showed that electrostatic complex formation is highly exothermic; therefore, raising the temperature should promote dissociation of the molecule from the polymer at equilibrium. Comparable ITC data for R6G with PAH showed zero complex formation within the limit of measurement.

Each layer-by-layer coating step was characterized with electronic absorption spectroscopy and with zeta potential measurements. A representative data set is shown for GNR+PAA+R6G+PAA+PAH+PAA (Figure 2.2). Slight changes in the plasmon band maxima were observed, as there is some loss of signal due to sample loss upon purification by centrifugation. The slight tailing at long wavelengths suggests a small amount of nanorod aggregation. Zeta potential measurements showed evidence for bulk average successful polymer layer coating, as the nanorod surface charge changed in accord with the net charge of each polymer layer.

Samples of wrapped nanorods were purified after each coating step by centrifugation. To quantify the amount of bound dye, supernatants were separated at each step from the nanorod pellets, and fluorescence spectra were acquired from the supernatants to measure free dye by comparison to a fluorescence calibration curve. The numbers of bound molecules were calculated per nanorod based on: total dye – free dye = bound dye. On average, all the nanorods bore ~1200-1700 R6G molecules per rod (Table 2.1). For release studies, all samples were concentrated to achieve a constant GNR concentration of 2 nM.

For the laser irradiation release, 200 μL of wrapped GNR sample solutions were each added to two vials. One vial was then exposed to 785 nm continuous wave laser light (DeltaNu Advantage 785 Raman Laser System) with a power of ~48 mW and the spot size of ~1.5 mm^2 at the sample, for a set amount of time (5 minute intervals from 0-60 minutes); the other vial served as a control without laser exposure. Two new vials of sample were prepared separately for each different time point of laser exposure. After irradiation, samples and their controls were spun down by centrifugation, and the supernatants were separated from the pellets. The amount of R6G in the supernatants was quantified by fluorescence spectroscopy against a standard calibration curve. The amount of light-triggered released dye was obtained by subtracting the fluorescent signal of the control sample from the fluorescent signal of the irradiated sample for each time-point pair.

After 60 minutes of laser irradiation, a representative sample (GNR+PAA+R6G+PAA) was analyzed to assess any changes in the GNRs compared to its control solution as well as the

original unmodified GNR solution (Figure 2.3). Samples with or without laser exposure showed no obvious difference either in the absorption spectra or TEM images, suggesting that any heat generated by the laser was not large enough to cause any significant morphology changes to the gold nanorods in the sample solution during laser irradiation process.

Dye release rates were obtained by equilibrium measurements of the fluorescence intensity of sample supernatants corrected for their controls (thus canceling the effect of passive diffusion) as a function of laser irradiation time, and as a function of trapping polyelectrolyte layers. Dye release was linear with time of irradiation. An increase in the number of wrapping layers from one to two to three decreased release, to the point of no measurable release, with three outer layers (Figure 2.4a), for PAA as the polyelectrolyte on both sides of the R6G layer. For GNR samples with a PAA-R6G-PAH array, dye release under the same conditions could be observed with only one trapping layer, but no release was observed with two trapping layers (Figure 2.4b). It is possible that the released dye might be associated with polyelectrolyte; control experiments confirmed that PAA does not alter R6G fluorescence, and no signal from supernatants was observed by dynamic light scattering or zeta potential analysis (therefore, nothing larger than 3 nm was released within the detection limits of the instrument).

The general trend of that an increase in the number of trapping layers would decrease molecular release makes intuitive sense, as the molecules would have to "fight" their way out through more layers. One surprising finding is that only 2-3 polyelectrolyte layers, with an estimated thickness of 3-5 nm,[34] are sufficient to stop molecular release under these conditions.

We estimated the R6G diffusion coefficient for the case of maximum release (one PAA trapping layer) using the same flux calculations as Mohwald et al. did for their dye (fluorescein) being released from a 5 micron core particle through 8-18 polyelectrolyte layers at different ionic strengths.[35] In our case, we calculate a diffusion coefficient of ~10^{-18} m^2/s. This is far less than Mohwald's findings under different solution conditions (~10^{16} m^2/s)[35] but similar to what has been found for dye diffusion through planar polyelectrolyte multilayers (10^{-18} – 10^{-20} m^2/s).[36] Ionic strength play a role in these processes; increasing the NaCl concentration in our solutions does lead to more release, and laser irradiation increases it yet more (Supporting Information).

Another finding is that the thermodynamics of the polyelectrolytes may play a larger role in the ability to be released than previously thought. The ITC data suggested that R6G and PAA have strong interactions that would favor decomplexation upon heating, while R6G and PAH do not associate with each other at neutral aqueous conditions. However, since the R6G layer does not completely switch the zeta potential of the nanorods to cationic, a capping cationic PAH layer might in fact bind more tightly and compactly to underlying PAA/R6G layers than a capping PAA layer. In that case, the R6G molecules would be sandwiched between oppositely-charged polyelectrolytes and thus be more hindered from release. The relatively low number for the dye's diffusion coefficient is consistent with this notion.

In order to confirm that irradiation into the plasmon band is the source of heat, the release of R6G from the surface of gold nanospheres (GNPs) with a maximum absorption peak at 520 nm by the 785 nm laser was also investigated. The sample GNP+PAA+R6G+PAA solution with a

GNP concentration of 6 nM was used, in order to quantitatively match the total amount of bound dye as the GNRs. While dye release was observed (Table 2.1), it was very low compared to GNR samples; only a couple of molecules, out of ~1600, were released to the supernatant after 60 minutes of irradiation at 785 nm, compared to ~100 for the equivalent wrapping of gold nanorods that do absorb light strongly at 785 nm.

We replotted the release rates in terms of percent molecules released (Figure 2.5) and compared the quantity of molecules released upon irradiation to those for simple heating in a water bath. The data suggests that irradiation at 785 nm at room temperature (~ 25 ˚C) is equivalent to heating the entire sample to 35 ℃ - 37 ℃. In order to directly measure the degree of heating by the laser, a thermocouple was placed into the sample solution after 60 min laser irradiation and an ~8 ℃ temperature rise was recorded. This measurement, although crude, is in general agreement with the molecular release "effective temperature" data.

A continuous-wave laser with a low optical intensity of ~3 W/cm^2 can only increase the temperature of the gold nanorods' surface by ~ 10^{-4} K.[15] Therefore, unlike experiments with femtosecond pulsed lasers, dye release should not be interpreted as arising from a significant temperature rise on the particle surface, and non-equilibrium thermal mechanisms that involve hot electrons or bond breaking do not need to be applied to the release mechanism in this case. Others have made measurements of the heat increase from illuminated nanoparticles in single-molecule imaging mode for 25-35 mW laser powers (by measuring decreased dye emission due to increased temperature), and have concluded that the temperature rise is on the

order of 3K, and extends out ~10 microns from the nanoparticle at a given short time.[37] In our case, on the 5-60 minute time scales, we consider that first, the gold nanorods absorb the continuous-wave laser photons and convert the light to thermal energy, and thus increased the temperature of the whole solution by 8-10 degrees at maximum times. The bulk temperature rise of the sample solution shifted the exothermic reaction equilibrium PAA + R6G ⟷ PAA·R6G to the left, in accord with the ITC data. Additionally, the increased temperature could cause the thermal expansion of the polyelectrolyte layers, which also favors dye release.[10] The addition of further polyelectrolyte trapping layers slows down the release by a factor of 50-100 depending on layer conditions. This degree of control is far larger than has been reported in related systems, in which NIR irradiation of gold nanorods in a polymer gel showed a 4-fold level of difference in release compared to no illumination.[38]

There are many examples in the literature of molecular release from polyelectrolyte multilayers on surfaces (mostly flat, but some colloidal) in the absence of any sort of plasmonic heating.[35-41] It is illuminating to compare the time profile of our release (up to 60 minutes, and still increasing, upon plasmon irradiation) to analogous systems of dyes immobilized on polyelectrolyte layers on flat surfaces; in those systems, changes in pH or ionic strength can lead to very fast release (~30 s) that reaches molecular depletion from the layers within 10 minutes.[39] For thick multilayers, passive release can be on the scale of days.[40] Electrically driven release of molecules from polyelectrolyte layers (on an electrode surface) is another option for rapid release chip-based technologies.[41] Overall, our findings suggest that judicious choice of the

surface chemistry and plasmon illumination time can greatly tune the release rate of electrostatically adsorbed molecules from metal nanoparticles, with significant control from light.

2.3 FUTURE WORK

This photothermal molecular release system has demonstrated a promising route for future drug delivery applications based on gold nanorods. However, only 6% of the molecules loaded on the GNR surface were released after 60 min of continuous-wave laser irradiation. The slow release rate and relative small release percentage should be further increased in real drug delivery systems. In order to improve the release rate and percentage, larger laser power can be used to generate a higher temperature excursion in the drug delivery system to accelerate the de-complexation and diffusion rate of molecules as well as to increase the thermal expansion of the polymer layers. Though higher temperature can favor faster release, it may also induce thermal degradation of the loaded drug molecules, and a proper laser power should be chosen to ensure both the rate and quality of drug release. With cw laser irradiation, temperature in the whole region in the laser spot tends to increase. In order to get the localized heating only around gold nanorods, ultrafast laser pulse irradiation should be applied. Laser pulses can also generate large transient temperature rise to get a faster release rate. However, the problem of thermal degradation of drug molecules might also be severe. Testing the drug delivery system in biological environment is essential for its future application in clinical use. More experiments should be done other than in the simple aqueous solution environment. For example, this

molecular release system should be first tested at human body temperature of 37 ℃ instead of room temperature, pH and salt concentration can also affect drug release somehow. Despite the preferential accumulation of gold nanoparticles at tumor sites by the enhanced permeability and retention effect, the surface of GNRs should be further modified with molecules that have biocompatibility to the environment and biorecognition to the specific tissues or cells in order to get a higher efficiency of photothermal therapy and drug delivery to the targets. Thus the next test of this molecular release system should be performed in malignant tumor cell cultures or even in mice. Near infrared laser penetration efficiency in human organs still need to be tested to ensure effective laser-triggered release, but large laser power can also definitely harm human body. Various parameters and more tests in biological systems should be first done to get the potential drug delivery system into future biomedical applications.

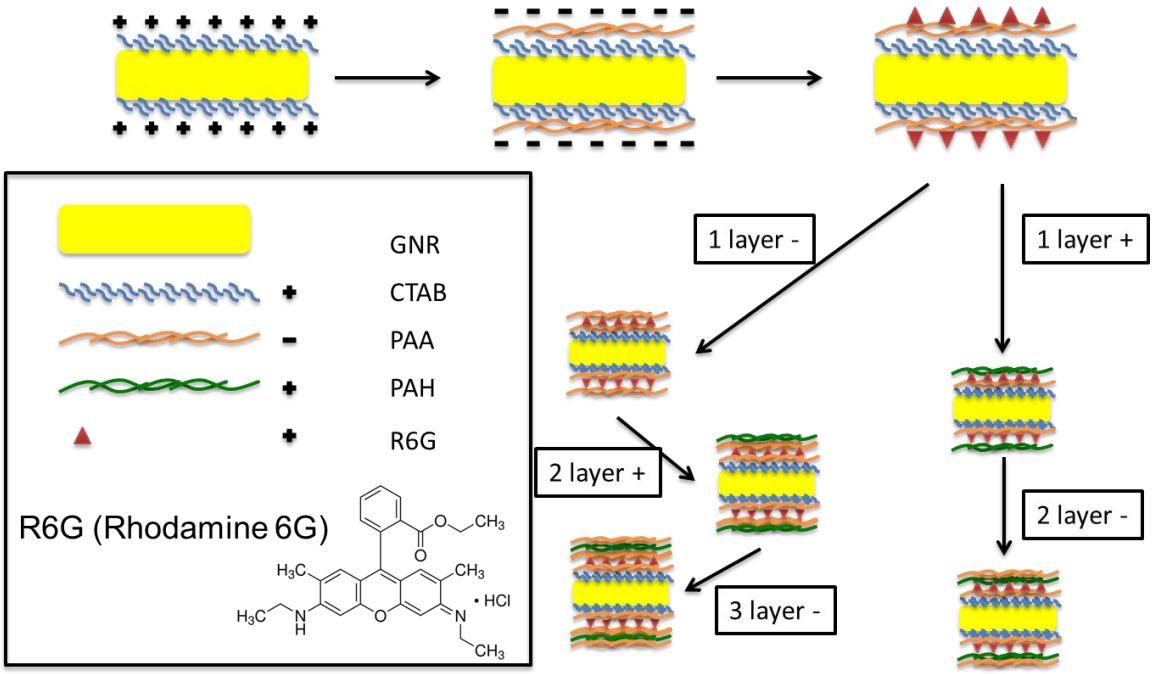

Scheme 2.1 GNR coating and R6G wrapping in different types of polymer layers:

(GNR+PAA+R6G+PAA)

(GNR+PAA+R6G+PAA+PAH)

(GNR+PAA+R6G+PAA+PAH+PAA)

(GNR+PAA+R6G+PAH)

(GNR+PAA+R6G+PAH+PAA).

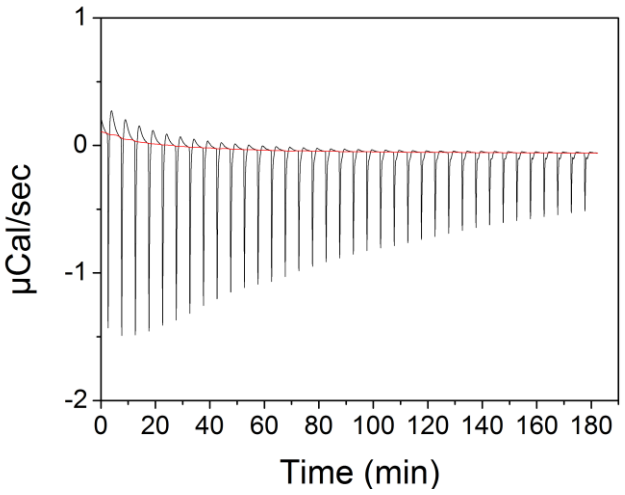

Figure 2.1 Isothermal titration calorimetry of R6G with PAA alone. $\Delta H = -1.6 \times 10^3$ kcal/mol; $\Delta S = -5.5$ kcal/mol/K; equilibrium binding constant = 4700 M^{-1}.

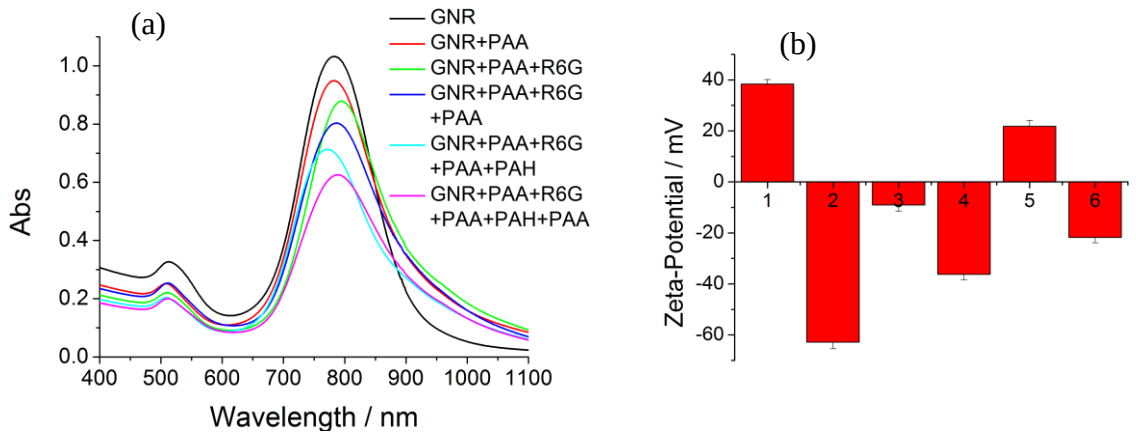

Figure 2.2 Layer-by-layer polyelectrolyte characterization at each step for GNR+PAA+R6G+PAA+PAH+PAA. (a) Electronic absorption spectra. (b) Zeta potential measurements; 1: original GNR; 2: GNR+PAA; 3: GNR+PAA+R6G (showing a decrease in zeta potential to more positive values, but not total coverage); 4: GNR+PAA+R6G+PAA; 5: GNR+PAA+R6G+PAA+PAH; 6: GNR+PAA+R6G+PAA+PAH+PAA.

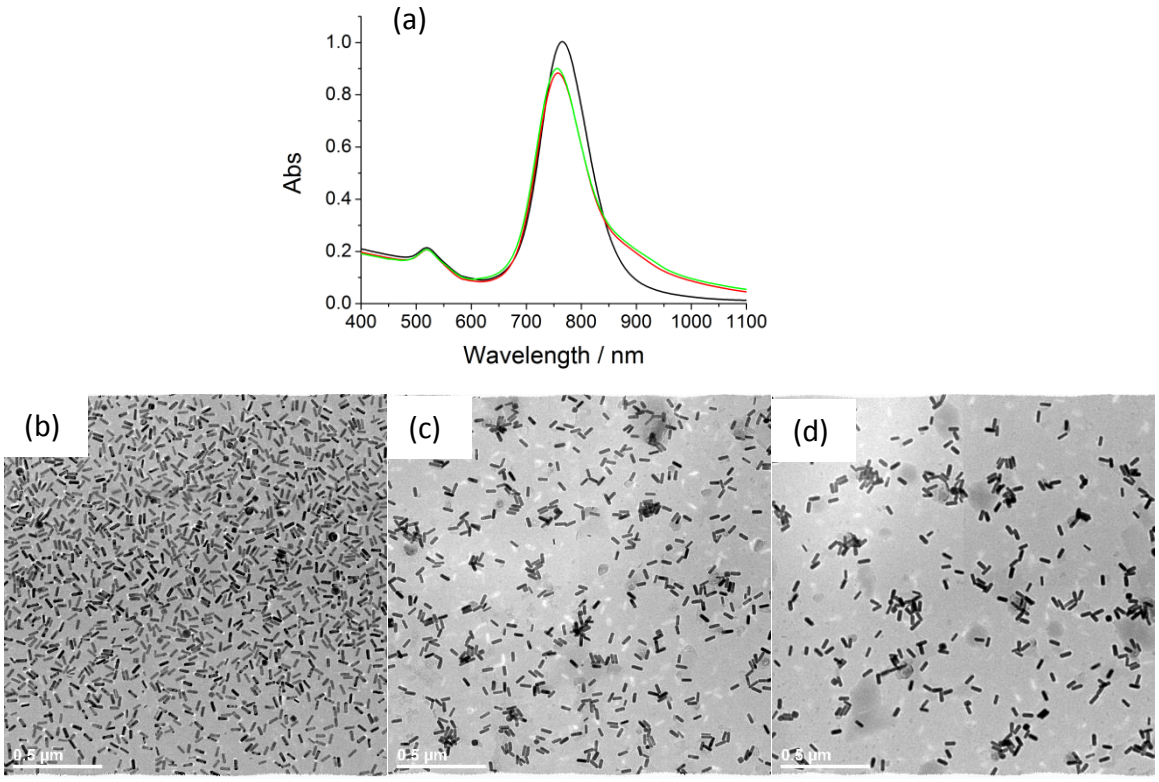

Figure 2.3 (a) Electronic absorption spectra of dye-loaded gold nanorods before and after laser irradiation, compared to controls. Black: original GNR; red: GNR+PAA+R6G+PAA without laser irradiation; green: GNR+PAA+R6G+PAA with laser irradiation for 60 min. (b) Transmission electron micrograph (TEM) of the original GNRs. (c) TEM of GNR+PAA+R6G+PAA without laser irradiation. (d) TEM of GNR+PAA+R6G+PAA with laser irradiation for 60 min. All scale bars = 500 nm.

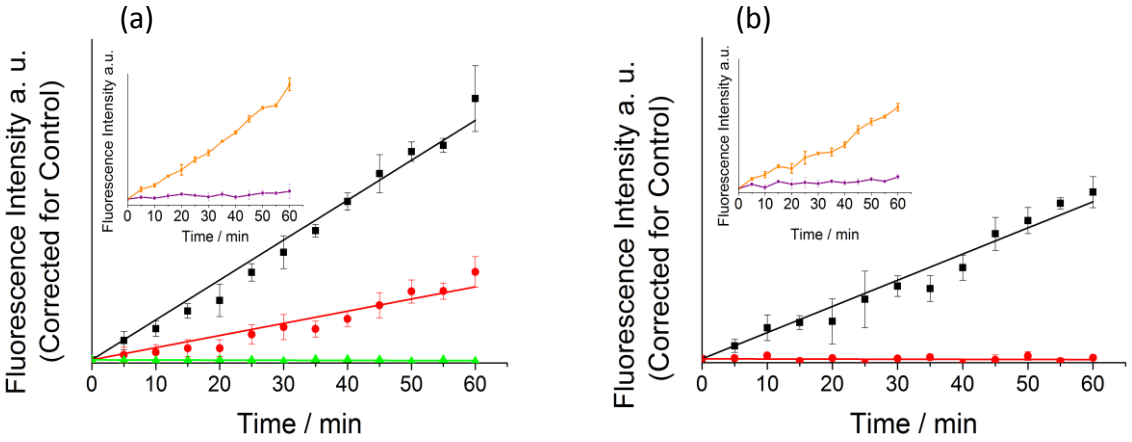

Figure 2.4 (a) Dye release rates plotted as supernatant fluorescence intensity vs. laser irradiation time of the samples with PAA as the first trapping layer. Black: GNR+PAA+R6G+PAA; red: GNR+PAA+R6G+PAA+PAH; green: GNR+PAA+R6G+PAA+PAH+PAA. Inset showed the raw fluorescence data of GNR+PAA+R6G+PAA laser irradiated sample (orange) and control sample (purple). (b) Dye release rates plotted as supernatant fluorescence intensity vs. laser irradiation time of the samples with PAH as the first trapping layer. Black: GNR+PAA+R6G+PAH; red: GNR+PAA+R6G+PAH+PAA. Inset showed the raw fluorescence data of GNR+PAA+R6G+PAH laser irradiated sample (orange) and control sample (purple). All data are the average of three runs, one standard deviation from the mean is represented by the error bars, and all are on the same vertical scale.

Table 2.1 Quantification of the Number of R6G Molecules Bound to Each Gold Nanoparticle (from 5000 R6G/GNR in the original incubation solutions) and the Number of R6G Molecules Released from Each Gold Nanoparticle after 60 min Laser Irradiation.

Sample	**Initial bound R6G#/GNR**	**Released R6G/GNR at 60 min**
GNR+PAA+R6G+PAA	1690 ±97	101 ± 6
GNR+PAA+R6G+PAA+PAH	1482 ±190	36 ± 5
GNR+PAA+R6G+PAA+PAH+PAA	1220 ±155	0 ± 0.1
GNR+PAA+R6G+PAH	1718 ±140	36 ± 3
GNR+PAA+R6G+PAH+PAA	1555 ±151	0 ± 0.1
GNP+PAA+R6G+PAA	1455 ±248	2.0 ± 0.4

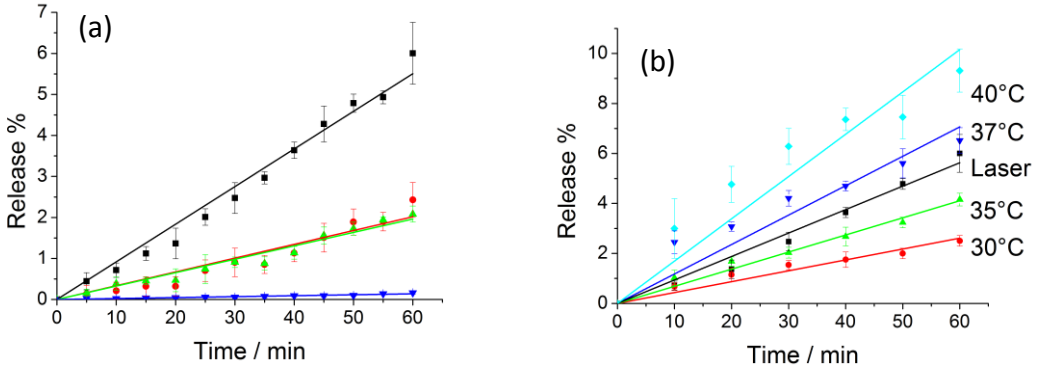

Figure 2.5 (a) Dye release rate plotted as the release percentage vs. time for different samples by laser irradiation. Black: GNR+PAA+R6G+PAA; red: GNR+PAA+R6G+PAA+PAH; green: GNR+PAA+R6G+PAH; blue: GNP+PAA+R6G+PAA. (b) Dye release rate plotted as the release percentage vs. time by thermal heating in a water bath for GNR+PAA+R6G+PAA (black curve in part (a)) compared to laser irradiation.

2.4 REFERENCES

1. Murphy, C. J.; Sau, T. K.; Gole, A. M.; Orendorff, C. J.; Gao, J.; Gou, L.; Hunyadi, S. E.; Li, T. Anisotropic Metal Nanoparticles: Synthesis, Assembly, and Optical Applications. *J. Phys. Chem. B* **2005**, *109*, 13857-13870.

2. Huang, X.; Neretina, S.; El ‐ Sayed, M. A. Gold Nanorods: From Synthesis and Properties to Biological and Biomedical Applications. *Adv. Mater.* **2009**, *21*, 4880-4910.

3. Norman, R. S.; Stone, J. W.; Gole, A.; Murphy, C. J.; Sabo-Attwood, T. L. Targeted Photothermal Lysis of the Pathogenic Bacteria, *Pseudomonas aeruginosa*, with Gold Nanorods. *Nano Lett.* **2008**, *8*, 302-306.

4. Choi, R.; Yang, J.; Choi, J.; Lim, E.-K.; Kim, E.; Suh, J.-S.; Huh, Y.-M.; Haam, S. Thiolated Dextran-Coated Gold Nanorods for Photothermal Ablation of Inflammatory Macrophages. *Langmuir* **2010**, *26*, 17520-17527.

5. Pissuwan, D.; Valenzuela, S. M.; Killingsworth, M. C.; Xu, X.; Cortie, M. B. Targeted destruction of murine macrophage cells with bioconjugated gold nanorods. *J. Nanopart. Res.* **2007**, *9*, 1109-1124.

6. Huang, Y.-F.; Sefah, K.; Bamrungsap, S.; Chang, H.-T.; Tan, W. Selective Photothermal Therapy for Mixed Cancer Cells Using Aptamer-Conjugated Nanorods. *Langmuir* **2008**, *24*, 11860-11865.

7. Bartczak, D.; Muskens, O. L.; Millar, T. M.; Sanchez-Elsner, T.; Kanaras, A. G. Laser-Induced Damage and Recovery of Plasmonically Targeted Human Endothelial Cells. *Nano Lett.* **2011**, *11*, 1358-1363.

8. Huang, X.; El-Sayed, I. H.; Qian, W.; El-Sayed, M. A. Cancer Cell Imaging and Photothermal Therapy in the Near-Infrared Region by Using Gold Nanorods *J. Am. Chem. Soc.* **2006**, *128*, 2115-2120.

9. Dickerson, E. B.; Dreaden, E. C.; Huang, X.; El-Sayed, I. H.; Chu, H.; Pushpanketh, S.; McDonald, J. F.; El-Sayed, M. A. Gold Nanorod assisted near-infrared plasmonic photothermal theraphy (PPTT) of squamous cell carcinoma in mice. *Cancer Lett.* **2008**, *269*, 57-66.

10. Kuo, T.-R.; Hovhannisyan, V. A.; Chao, Y.-C.; Chao, S.-L.; Chiang, S.-J.; Lin, S.-J.; Dong, C.-Y.; Chen, C.-C. Photothermal cancer therapy via femtosecond-laser-excited FePt nanoparticles. *J. Am. Chem. Soc.* **2010**, *132*, 14163-14171.

11. Yamashita, S.; Fukushima, H.; Akiyama, Y.; Niidome, Y.; Mori, T.; Katayama, Y.; Niidome, T. Controlled-release system of single-stranded DNA triggered by the photothermal effect of gold nanorods and its in vivo application. *Bioorg. Med. Chem.* **2011**, *19*, 2130-2135.

12. Wijaya, A.; Schaffer, S. B.; Pallares, I. G.; Hamad-Schifferli, K. Selective Relese of Multiple DNA Oligonucleotides from Gold Nanorods. *ACS Nano* **2008**, *3*, 80-86.

13. Chu, C.-H.; Wang, Y.-C.; Tai, L.-A.; Wu, L.-C.; Yang, C.-S. Surface deformation of gold nanorod-loaded poly(DL-lactide-*co*-glycolide) nanoparticles after near infrared irradiation: an active and controllable drug release system. *J. Mater. Chem.* **2010**, *20*, 3260-3264.

14. Wei, Q.; Ji, J.; Shen, J. Synthesis of Near-infrared Responsive Gold Nanorod/PNIPAAm Core/Shell Nanohybrids via Surface Initiated ATRP for Smart Drug Delivery. *Macromol. Rapid Commun.* **2008**, *29*, 645-650.

15. Huschka, R.; Zuloaga, J.; Knight, M. W.; Brown, L. V.; Nordlander, P.; Halas, N. J. Light-Induced Release of DNA from Gold Nanoparticles: Nanoshells and Nanorods. *J. Am. Chem. Soc.* **2011**, *133*, 12247-12255.

16. Shiotani, A.; Akiyama, Y.; Kawano, T.; Niidome, Y.; Mori, T.; Katayama, Y.; Niidome, T. Active Accumulatio of Gold Nanorods in Tumor In Response to Near-Infrared Laser Irradiation. *Bioconjugate Chem.* **2010**, *21*, 2049-2054.

17. Qin, Z.; Bischof, J. C. Thermophysical and biological responses of gold nanoparticle laser heating. *Chem. Soc. Rev.* **2012**, *41*, 1191-1217.

18. Alkilany, A. M.; Thompson, L. B.; Boulos, S. P.; Sisco, P. N; Murphy, C. J. Gold Nanorods: Their Potential for Photothermal Therapeutics, Tempered by the Complexity of their Biological Interactions. *Adv. Drug Deliv. Rev*. **2012**, 64, 190-199.

19. Alper, J.; Crespo, M.; Hamad-Schifferli, K. Release Mechanism of Octadecyl Rhodamine B Chloride from Au Nanorods by Ultrafast Laser Pulses. *J. Phys. Chem. C* **2009**, *113*, 5967-5973.

20. Kyrsting, A.; Bendix, P. M.; Stamou, D. G.; Oddershede, L. B. Heat Profilling of Three-Dimensionally Optically Trapped Gold Nanoparticles using Vesicle Cargo Release. *Nano Lett.* **2010**, *11*, 888-892.

21. Huschka, R.; Neumann, O.; Barhoumi, A.; Halas, N. J. Visualizing Light-Triggered Release of Molecules Inside Living Cells. *Nano Lett.* **2010**, *10*, 4117-4122.

22. Nakanishi, J.; Nakayama, H.; Shimizu, T.; Ishida, H.; Kikuchi, Y.; Yamaguchi, K.; Horiike, Y. Light-Regulated Activeation of Cellular Signaling by Gold Nanoparticles That Capture and Release Amines. *J. Am. Chem. Soc.* **2009**, *131*, 3822-3823.

23. You, J.; Shao, R.; Wei, X.; Gupta, S.; Li, C. Near-Infrared Light Triggers Release of Paclitaxel from Biodegradable Microspheres: Photothermal Effect and Enhanced Antitumor Activity. *Small* **2010**, *6*, 1022-1031.

24. Volodkin, D. V.; Skirtach, A. G.; Möhwald, H. Near-IR Remote Release from Assemblies of Liposomes and Nanoparticles. *Angew. Chem. Intl. Ed.* **2009**, *48*, 1807-1809.

25. An, X.; Zhang, F.; Zhu, Y.; Shen, W. Photoinduced drug release from thermosensitive AuNPs-liposome using a AuNPs-switch. *Chem. Commun.* **2010**, *46*, 7202-7204.

26. Bretschneider, J. C.; Reismann, M.; von Plessen, G.; Simon, U. Photothermal Control of the Activity of HRP-Functionalized Gold Nanoparticles. *Small* **2009**, *5*, 2549-2553.

27. Poon, L.; Zandberg, W.; Hsiao, D.; Erno, Z.; Sen, D.; Gates, B. D.; Branda, N. R. Photothermal Release of Single-Stranded DNA from the Surface of Gold Nanoparticles Through Controlled Denaturating and Au-S Bond Breaking. *ACS Nano* **2010**, *4*, 6395-6403.

28. Wu, G.; Mikhailovsky, A.; Khant, H. A.; Fu, C.; Chiu, W.; Zasadzinski, J. A. Remotely Triggered Lipsome Release by Near-Infrared Light Absorption via Hollow Gold Nanoshells. *J. Am. Chem. Soc.* **2008**, *130*, 8175-8177.

29. Park, H.; Yang, J.; Seo, S.; Kim, K.; Suh, J.; Kim, D.; Haam, S.; Yoo, K. Multifunctional Nanoparticles for Photothermally Controlled Drug Delivery and Magnetic Resonance Imaging Enhancement. *Small* **2008**, *4*, 192-196.

30. Moon, G. D.; Choi, S.-W.; Cai, X.; Li, W.; Cho, E. C.; Jeong, U.; Wang, L. V.; Xia, Y. A New Theranostic System Based on Gold Nanocages and Phase-Change Materials with Unique Features for Photoacoustic Imaging and Controlled Release. *J. Am. Chem. Soc.* **2011**, *133*, 4762-4765.

31. Chen, J.; Yang, M.; Zhang, Q.; Cho, E. C.; Cobley, C. M.; Kim, C.; Glaus, C.; Wang, L. V.; Welch, M. J.; Xia, Y. Gold Nanocages: A Novel Class of Multifunctional Nanomaterials for Theranostic Applications. *Adv. Funct. Mater.* **2010**, *20*, 3684-3694.

32. Yavuz, M. S.; Cheng, Y.; Chen, J.; Cobley, C. M.; Zhang, Q.; Rycenga, M.; Xie, J.; Kim, C.; Song, K. H.; Schwartz, A. G.; Wang, L. V.; Xia, Y. Gold nanocages covered by smart polymers for controlled release with near-infrared light. *Nature Mater.* **2009**, *8*, 935-939.

33. Sau, T. K.; Murphy, C. J. Seeded High Yield Synthesis of Short Au Nanorods in Aqueous Solution. *Langmuir* **2004**, *20*, 6414-6420.

34. Gole, A.; Murphy, C. J. Polyelectrolyte-Coated Gold Nanorods: Synthesis, Characteriztion and Immobilization. *Chem. Mater.* **2005**, *17*, 1325-1330.

35. Antipov, A. A.; Sukhorukov, G. B.; Donath, E.; Mohwald, H. Sustained release properties of polyelectrolyte multilayers capsules. *J. Phys. Chem. B* **2001**, *105*, 2281-2284.

36. Peyratout, C. S.; Dahne, L. Tailor-Made Polyelectrolyte Microcapsules: From Multilayers to Smart Containers. *Angew. Chem. Int. Ed*. **2004**, *43*, 3762-3783.

37. Skirtach, A. G.; Dejugnat, C.; Braun, D.; Susha, A. S.; Rogach, A. L.; Parak, W. J.; Mohwald, H.; Sukhorukov, G. B. The Role of Metal Nanoparticles in Remote Release of Encapsulated Materials. *Nano Lett.* **2005**, *5*, 1371-1377.

38. Hribar, K. C.; Lee, M. H.; Lee, D.; Burdick, J. A. Enhanced Release of Small Molecules from Near-Infrared Light Responsive Polymer-Nanorod Composites. *ACS Nano* **2011**, 5, 2948-2956.

39. Chung, A. J.; Rubner, M. F. Methods of Loading and Releasing Low Molecular Weight Cationic Molecules in Weak Polyelectrolyte Multilayer Films. *Langmuir* **2002**, *18*, 1176-1183.

40. Berg, M. C.; Zhai, L.; Cohen, R. E.; Rubner, M. F. Controlled Drug Release from Porous Polyelectrolyte Multilayers. *Biomacromolecules* **2006**, *7*, 357-364.

41. Schmidt, D. J.; Moskowitz, J. S.; Hammond, P. T. Electrically Triggered Release of a Small Molecule Drug from a Polyelectrolyte Multilayer Coating. *Chem. Mater*. **2010**, *22*, 6416-6425.

CHAPTER 3

ULTRAFAST THERMAL ANALYSIS OF SURFACE FUNCTIONALIZED GOLD NANORODS IN AQUEOUS SOLUTION

3.1 INTRODUCTION

Gold nanorods (GNRs) exhibit both transverse and longitudinal surface plasmon resonances, tunable from the visible to the near-infrared (NIR) as a function of nanorod shape,[1,2] and can absorb photons and convert light into heat through a series of non-radiative photophysical processes.[3] When a gold nanorod interacts with a femtosecond laser pulse, the photothermal events include: (1) an increase in the electron temperature, through electron-electron scattering, within several hundred fs; (2) an increase in the lattice temperature, through electron-phonon coupling, within 1-10 ps; (3) dissipation of heat from the hot particle to the surrounding media to reach thermal equilibrium within 100 ps to several ns, depending on the particle size, thermal properties of the surroundings, and laser intensity.[3–5]

The combination of photothermal effects with the ability to functionalize the GNR surface has led to potential biological applications of GNRs such as targeted cell ablation[6–8] and targeted drug delivery.[9–12] Engineering applications of GNRs and other plasmonic nanomaterials require improved scientific understanding of thermal transport at the nanocale.[13,14] The study of heat transfer rate or spatio-temporal temperature distribution around the heated nanostructures is

This chapter is reprinted with permission from Jingyu Huang, Jonglo Park, Wei Wang, Catherine J. Murphy and David G. Cahill, *ACS Nano*, **2013**, *7* (1), pp 589–597. (DOI: 10.1021/nn304738u)

important for both photothermal therapies, and the effect of local heating on catalysis[15] and surface reactions.[16–18] Moreover, the study of thermal transport can provide information about vibrational energy transfer through molecular adsorbates, and thereby probe the properties of the adsorbed molecular layer.[19,20]

Pump-probe transient absorption has been widely applied to study heat transfer from noble metal nanoparticles to their surroundings.[21–27] The particle/water interface thermal conductance (G) of GNRs with different ligands on their surface has been studied by Hamad-Schifferli *et al*. by probing changes in the longitudinal surface plasmon band; these transient absorption changes were modeled numerically to extract values for the effective interface thermal conductance G.[24,25] However, in their work[24,25] the model fitting could only be applied to absorption changes at time scales longer than 300 ps, and their calculated thermal conductivity (the product of G and thickness of the ligand layer) of the surface layers were ~1 W m^{-1} K^{-1}, much larger than the typical values of 0.1-0.5 W m^{-1} K^{-1} for organic materials.[28] Hamad-Schifferli *et al*. used a frequency-doubled pump laser at 400 nm to heat the GNRs (which had a longitudinal plasmon peak at 770 nm) and a probe laser at 800 nm to perform the transient absorption experiments. Transient absorption data taken at the red side of the plasmon band will include contributions from both gold nanorod cooling and the heating of the surrounding media[26,29]; the sum of these two processes can be misinterpreted as large G values.

This artifact can be avoided by tuning the pump and the probe to the wavelength of peak absorption.[26,29] By combining transient absorption measurements at the wavelength of peak absorption and measurements of the coating thickness by dynamic light scattering (DLS), we

find that we can determine both the thermal conductivity and heat capacity per unit volume of the nanorod coatings. Our approach for thermal analysis using temperature excursions on picosecond to nanosecond time-scales is analogous to the use of the plasmon resonance to probe the index of refraction of the immediate surroundings of the nanorods. The plasmon resonance involves electric fields that are localized to the close proximity of the nanorod. Following rapid heating of the nanoparticle by the pump optical pulse, temperature excursions are similarly confined on small length scales. Thermal diffusion constants in water or organic layers are on the order of 10^{-3} cm^2 s^{-1}. Therefore, thermal diffusion distances on time-scales of 10 ps to 1 ns are 2 to 20 nm.

3.2 RESULTS AND DISCUSSION

Gold nanorods were prepared by the aqueous seed-mediated and silver-assisted method[30]. The aspect ratio was controlled so that the longitudinal surface plasmon wavelength maximum was at ~776 nm. Transmission electron microscopy (TEM) showed that the GNRs had average dimensions 46 ± 5 nm $\times$ 12 ± 1.1 nm, for an aspect ratio of 3.8 (Figure 3.1). ζ-potential measurements confirmed that the GNR colloids were positively charged at pH 7, due to the cationic surfactant cetyltrimethylammonium bromide (CTAB) bilayer on the surface of the synthesized GNRs.[1,31] GNR concentrations in aqueous solution were kept at ≈0.15 nM for absorption spectra measurements and ≈1 nM for transient absorption and dynamic light scattering measurements. The optical path length of the sample solutions was 1 cm for absorption spectra measurements and 0.1 mm for transient absorption measurements.

Transient absorption was used to probe thermal transport from the GNR, through the organic coatings, and into the surrounding water. A laser power of 1.5 mW was chosen for both pump and probe beams compromise between a high level of signal-to-noise and low temperature rise of the GNRs. The average transient heating for the entire ensemble GNRs was estimated to be 7 K by dividing the total energy absorbed by the GNRs per pump laser pulse with the volumetric heat capacity of gold and the total volume of gold in the laser beam spot. The temperature excursions of individual GNRs vary widely because of the dependence of the optical cross-section on orientation and aspect ratio. We estimate a maximum heating of 45 K for GNRs with the maximum optical cross-section. For such temperature rises, there should be no nanorod melting shape change,[3,32] the stable signals of repeated transient absorption experiments at the same sample spot also proved the thermal stability of GNRs under this laser power. The absorbance change created by pump heating of ~10^{-3} is small compared to the total absorbance of the sample solution of ~0.1. For such small absorbance excursions, the GNR absorbance can be considered to change linearly with the GNR temperature.

To gain insight on how the transient absorption signal changes with the choice of pump and probe wavelengths, we first studied the transient absorption of the GNR aqueous solution using the same wavelength for the pump and probe and varied the wavelength from 740 nm to 820 nm, i.e., from the blue side to the red side of the peak of the longitudinal plasmon absorption. The decay of the transient signal is faster at the blue side of the plasmon peak and slower at the red side (Figure 3.2a).

We also performed experiments using sharp edged optical filters[33] to fix the pump beam wavelength at 790 nm while changing the probe beam wavelength from 790 nm to 770 nm. (The homogeneous line-width of a single GNR of aspect ratio 3.8 is expected to be 30-40 nm[34] and therefore the absorption of our samples, see Figure 3.1a, has significant inhomogeneous broadening.) Using this approach, we observe an even more pronounced dependence of the decay of transient absorption on probe wavelength (Figure 3.2b) than when both the pump and probe wavelengths are changed simultaneously (Figure 3.2a).

The dependence of the transient absorption signal on the laser wavelength can be attributed to the effects of heating and resulting changes in the index of refraction of the surrounding media, when the heat flows out of GNR to the surroudings. The absorption spectra for ellipsoidal particles is described by Gans theory[3,5]:

$$\sigma_{abs} = \frac{2\pi V}{3\lambda}\varepsilon_m^{3/2}\sum_{j=a,b,c}\frac{(1/P_j^2)\varepsilon_2}{(\varepsilon_1+(1-P_j)\varepsilon_m/P_j)^2+\varepsilon_2^2} \tag{3.1}$$

where σ_{abs} is the absorption cross section, V is the volume of the particle, λ is the wavelength of light, ε_m is the media dielectric constant, ε_1 and ε_2 are the real and imaginary parts of gold dielectric constant, respectively. The depolarization factors P_j are defined by:

$$P_a = \left(\frac{1-e^2}{e^2}\right)\left\{\frac{1}{2e}\ln\left(\frac{1+e}{1-e}\right)-1\right\} \tag{3.2}$$

$$P_b = P_c = \frac{1-P_a}{2} \tag{3.3}$$

where a, b, and c are the three axes of the nanoparticle, a>b=c, $e=(1-(1/AR)^2)^{1/2}$, and AR is the aspect ratio of the GNRs. Thus, the absorption spectra change of GNRs can be affected by both the dielectric constants of gold and the surrounding media. The total absorption cross section change can be considered to be the addition of both factors[26]:

$$\Delta\sigma_{abs}(\lambda)=\left(\frac{\partial\sigma_{abs}}{\partial\varepsilon_1}\frac{d\varepsilon_1}{dT_p}+\frac{\partial\sigma_{abs}}{\partial\varepsilon_2}\frac{d\varepsilon_2}{dT_p}\right)_\lambda \Delta T_p+\left(\frac{\partial\sigma_{abs}}{\partial\varepsilon_m}\frac{d\varepsilon_m}{dT_m}\right)_\lambda \Delta T_m \tag{3.4}$$

where T_p is the temperature of the gold nanorod, T_m is the temperature of the media surrounding the GNRs. Using Gans theory and the temperature-dependent optical properties of Au[35], we estimate that the values of the six coefficients at the GNR plasmon absorption peak are: $\partial\sigma_{abs}/\partial\varepsilon_1\approx-2\times10^3$ nm^2; $\partial\sigma_{abs}/\partial\varepsilon_2\approx-5\times10^3$ nm^2; $\partial\sigma_{abs}/\partial\varepsilon_m\approx-4\times10^2$ nm^2; $d\varepsilon_1/dT_p\approx2\times10^{-3}$ K^{-1}; $d\varepsilon_2/dT_p\approx2\times10^{-3}$ K^{-1}; $d\varepsilon_m/dT_m\approx-2\times10^{-4}$ K^{-1}.

Increasing the temperature of gold nanorods induces a red shift of the plasmon peak and a decrease in the peak height,[36–38] while the heating of water causes the water dielectric constant to decrease,[39] which blue-shifts the plasmon peak.[38,40] At short time scales, when the heat generated within the GNR has not yet been transferred to the surrounding media, ε_m is constant and the transient absorption signal is only due to the temperature increase of the GNRs; at long time scales when the heat has been transferred to the surrounding media, ε_m decreases and shifts the GNR absorption peak to blue. At the wavelength of peak absorption, the coefficient of the ΔT_p term in Eq. 3.4 is ≈-14 nm^2 K^{-1}, while the coefficient of the ΔT_m term in Eq. 3.4 is close to zero,

≈ 0.08 nm^2 K^{-1}. Thus, all subsequent measurements were performed by setting the wavelength of the pump and probe at the wavelength of peak absorption.

As-synthesized GNRs bear a bilayer of CTAB on their surfaces,[1,31] which is in equilibrium with free CTAB in solution. (The fact that other quaternary ammonium surfactants can exchange with CTAB upon prolonged exposure[41] provides evidence that the kinetics are sufficient to establish equilibrium between the nanorod coating and the solution.) To vary the properties of the CTAB surface layer, GNR pellets were dispersed in CTAB solutions with the concentration varying from 0 mM to 100 mM. The final CTAB concentration in the sample solution were estimated with the assumptions that: (1) the GNRs originally had a 3.9 nm CTAB layer before dispersion, and after dispersion, part of the CTAB molecules originally on the GNR surface desorb and reduce the CTAB layer thickness to what has been estimated from DLS data, per the discussion below; and (2) the CTAB layer has a density of 1 g mL^{-1}. The final CTAB concentration in the sample solution is the sum of the starting CTAB concentration in the solution and the contribution from CTAB removed from the GNR surface (Figure 3.3b-c), which also depends on the GNR concentration in the sample solution.

The plasmon peak of the sample shifted to the red, from 776 nm to 788 nm (Figure 3.3a-b) as the CTAB solution concentration increased from 0.001 mM to the critical micelle concentration (cmc), 0.92-1.00 mM.[42,43] As expected, the wavelength of peak absorption stayed constant at concentrations exceeding the cmc since the presence of CTAB micelles in solution approximately fixes the chemical potential.

Dynamic light scattering measurements showed a small increase of the effective hydrodynamic diameter (d_H) of the GNRs in water upon increasing the CTAB solution concentration up to 1 mM CTAB in solution (Figure 3.3c). From 1-100 mM, the apparent size of all objects in solution increases much more dramatically, an effect that we attribute to presence of CTAB micelles in the solution. The experimental thickness (h) of the CTAB bilayer can be extracted from the hydrodynamic diameters using the following relationships:[44,45]

$$d_H = \frac{k_B T}{3\pi\eta D_t} \tag{3.5}$$

$$D_t = \frac{k_B T(\ln(L/d_{cs}) + C_t)}{3\pi\eta L} \tag{3.6}$$

$$C_t = 0.312 + 0.565\left(\frac{d_{cs}}{L}\right) - 0.100\left(\frac{d_{cs}}{L}\right)^2 \tag{3.7}$$

$$L = L_{GNR} + 2h \tag{3.8}$$

$$d_{cs} = d_{GNR} + 2h \tag{3.9}$$

where d_H is the hydrodynamic diameter due to the translational diffusion of the GNRs, k_B is the Boltzmann constant, T is the temperature of sample solution, η is the solution viscosity, D_t is the translational diffusion constant, L is the total length of the coated GNR, d_{cs} is the total diameter of the coated GNR, L_{GNR} and d_{GNR} are the bare average length and diameter of the GNRs measured from TEM micrographs.

We found that the transient absorption signals measured at the peak of the plasmon absorption (Figure 3.4a) can be used to extract both the thermal conductivity and heat capacity of the CTAB layers surrounding the GNRs. The rapid decay during the first 10 ps is due to electron-phonon coupling, and is followed by acoustic vibrations which decay by ≈500 ps.[5] Data were analyzed using a heat conduction model developed by A. Schmidt and co-workers[24]. This model neglects the interfacial thermal conductances of particle/surface and surface layer/solvent interfaces, instead, the factors from the interfacial thermal conductances are included into the thermal properties of the surface layers, otherwise, fitting would be impossible with more than two free parameters in this case. The calculated thicknesses (h) of the CTAB bilayer in different samples, using Eqs. 3.5-3.9, are displayed in Table 1. For GNRs in CTAB solutions above the critical micelle concentration, we used a thickness of 3.9 nm. Since the absorption spectra and transient absorption of the 10 mM CTAB and 100 mM CTAB solutions are similar to that of GNRs in 1 mM CTAB solution, it implies that the CTAB bilayer structure for GNRs in >1 mM CTAB solution is constant.

Table 3.1. Thickness of CTAB Layers on GNRs in CTAB Solutions with Different Estimated Final CTAB Concentrations.

[CTAB] (mM)	**0.006**	**0.007**	**0.014**	**0.10**	**1.0**	**10**	**100**
h (nm)	2.9	2.9	3.2	3.6	3.9	3.9	3.9

A typical fit of the transient absorption data to the model is shown in Figure 3.4b; the fit is constrained to delay times between 30 ps and 2 ns. We treated the thermal conductivity (Λ) and volumetric heat capacity (C) of the CTAB bilayer as free parameters in the fit. The deviation (D) between the fit and the data was calculated using Eq. 3.10.

$$D = \frac{\sum_{i=1}^{n}\left(\frac{|abs_{Fit}|_i - |abs_{Data}|_i}{|abs_{Data}|_i}\right)^2}{n} \tag{3.10}$$

where $|abs_{Fit}|$ and $|abs_{Data}|$ are the absolute absorbance of the fit and data at a certain delay time, respectively; n is the number of points. A contour of constant deviation between the fit and the data for this two-dimensional parameter space are plotted in Figure 3.5. This contour is drawn at the points where the deviations are twice the minimum deviation ($D \approx 10^{-3}$) between the data and the fit.

The thermal conductivity (Λ) of the CTAB bilayer is centered at ≈0.24 W m^{-1} K^{-1} for samples at CTAB concentrations < 1 mM, which decreases to ≈0.18 W m^{-1} K^{-1} for samples at CTAB concentration > 1 mM. The data further suggest that a full CTAB bilayer has a thermal conductivity more dominated by the organic alkyl chain than water, as thermal conductivities for alkanes at 20˚C are 0.11-0.14 W m^{-1} K^{-1} while that of water is 0.61 W m^{-1} K^{-1}. [23,46] The volumetric heat capacity of the CTAB bilayer is constant and centered at 2.0 J cm^{-3} K^{-1}, which is similar to the values reported for many polymers.[28]

The surface charge of CTAB-coated GNRs is positive in water[45]. Polyelectrolyte layer-by-layer coating is an effective way to increase the thickness of the surface layers on GNRs and also to convert positively-charged nanorods into negatively-charged ones and vice-versa.[47] For GNRs with polyelectrolyte coatings, the longitudinal plasmon peak shifts after each coating step due to the change in the refractive index of the surrounding media (Figure 3.6a); here, poly(acrylic acid) (PAA) is the anionic polyelectrolyte, and poly(allylamine hydrochloride (PAH)) is the cationic polyelectrolyte, which are added in succession to the surface of GNRs. The first PAA layer coating blue-shifts the plasmon peak ~8 nm. This phenomenon can be explained by considering that the surrounding environment change from organic-like to water-like, as hydrophilic PAA molecules replace part of the CTAB bilayer and bring associated water molecules near the GNR surface. As additional polyelectrolyte layers are deposited, the plasmon peak maximum shifts slightly, in an alternating fashion, for each layer (Figure 3.6b). ζ-potential measurements confirm the alternating surface charge upon successive rounds of PAA or PAH coating (Figure 3.6c).

Dynamic light scattering measurements show an increasing hydrodynamic diameter of the particles after the polyelectrolyte coatings, as expected, although the PAA/PAH alternating behavior in the shift of the plasmon band is recapitulated in an alternating trend in overall effective size (Figure 3.6d). Whether this means that polyelectrolyte layers are being released for the odd-number layers, or multilayers are added for the even-number layers, is not clear from

this data alone. Nonetheless, the same approaches for transient absorption measurements and data analysis can be applied to these samples as they were to the CTAB-coated samples.

The calculated thickness for the polyelectrolyte layers is shown in Table 2. The increasing thickness of PAA-terminated (layers 1, 3, 5) coating layers measured by DLS is not reflected in the degree of red-shifting of the plasmon absorption peak that would be expected if the index of refraction of the coating is constant. In other words, as the coating layer increases, the coating layers are apparently becoming less dense. The PAH-terminated (layers 2, 4, 6) coating layers with the increasing layer thickness have the same plasmon absorption peak position. This also implies that the as the number of coating layers increases, the density decreases.

Table 3.2 Thickness of Polyelectrolyte Layers (PEL) on Wrapped GNRs

No. of PEL	**0**	**1**	**2**	**3**	**4**	**5**	**6**
h (nm)	2.9	3.8	7.2	5.6	9.4	7.7	12.6

Transient absorption data were acquired at the wavelength of peak absorption of the polyelectrolyte-wrapped GNRs. The transient absorption changes of samples with PAH as the outer layer (layers 2, 4, 6) are significantly slower than samples with PAA as the outer layer (layers 1, 3, 5; Figure 3.7a). To fit the transient absorption data, all the polyelectrolyte layers and the original CTAB layer are considered as one surface layer with uniform thermal properties. A typical fit of the transient absorption data to the model is shown in Figure 3.7b. Both the thermal

conductivity (Λ) and volumetric heat capacity (C) are varied to fit the transient absorption curves. Contours of constant deviation between the fit and the data for this two-dimensional parameter space are plotted in Figure 3.8. This contour is drawn at the points where the deviations are twice the minimum deviation between the raw data and the fitted data.

For PAA-terminated samples (layers 1, 3, 5), the Λ values increase from 0.32 W m^{-1} K^{-1} to 0.45 W m^{-1} K^{-1} as the number of coating layers increases; C values range between 2.2 and 2.8 J cm^{-3} K^{-1}. The increased Λ and C values compared to the CTAB-only coated GNRs can be explained by possible water penetration when the polyelectrolytes are present. For PAH-terminated samples (layers 2, 4, 6), Λ values decrease slightly from 0.58 W m^{-1} K^{-1} to 0.53 W m^{-1} K^{-1}, while C values increase from ~3.2 J cm^{-3} K^{-1} to ~4.8 J cm^{-3} K^{-1} as the number of coating layers increases. The larger numbers compared to CTAB-only and PAA-terminated GNRs suggest that even more water is present near the GNR surface for PAH-terminated GNRs.

Periodic changes in water content with alternative anionic and cationic polyelectrolyte multilayer coatings has been widely observed.[48–52] Neutron reflectivity studies of multilayers of polystyrene sulfonate (PSS) and PAH on silicon surfaces suggest that these polyelectrolyte multilayer films are heavily hydrated; water occupies > 40% of the volume within the films.[48] In the PSS/PAH study, the data suggested that the water content varied periodically with the nature of the layers (PSS was more hydrated than PAH).[48] The swelling behavior of layer-by-layer assemblies of PSS/PAH was investigated.[49] A pronounced “odd-even effect” in the thickness and refractive index of the swollen layers depending on the outmost layer type was observed. They

concluded that water was pressed out of the multilayers when PAH is adsorbed onto the PSS layer and more water penetrates into the multilayer after the next adsorption of PSS layer.[49] Similar "odd-even effect" in the thickness[53] and Young's modulus[54] for PAA/PAH multilayers have been reported, in which the PAA-terminated multilayers have relatively smaller thickness[53] and higher Young's modulus[54] than the PAH-terminated multilayers. Our data suggest that a similar situation is present in the PAA/PAH multilayers on GNRs, in that the apparent water content varies periodically with nature of the wrapping layers and therefore affects thermal conductivity and heat capacity of the layers.

Transient absorption spectra of gold nanorods with rationally tuned surface coatings have been examined for different surface treatments, in order to analyze the thermal conductivity and heat capacity of the coatings. The quaternary ammonium surfactant CTAB forms a bilayer on the gold nanorods, with CTAB above the critical micelle concentration fixing the structure of the bilayer and the thermal properties. Dynamic light scattering can be used to measure the thickness of the surface layer with high precision. Polyelectrolyte multilayer coatings on top of the CTAB alter the apparent hydrophobic organic environment around the GNRs; polyelectrolyte and water penetration results in the increased thermal conductivity and heat capacity for the surface layers. The thermal conductivity and heat capacities measured in a transient absorption experiment can be used to infer the physical and chemical nature of species within ~10 nm of the surface of gold nanorods.

3.3 FUTURE WORK

This work used transient absorption technique to characterize the thermal properties of the surface coatings on the surface of gold nanorods. It also enables the calculation of spatiotemporal temperature evolution around a laser pulse-heated GNR with the heat conduction model and the thermal conductivity and volumetric heat capacity values of the coatings. This kind of knowledge is important for designing photothermal therapy and drug delivery with laser pulses and estimation of tumor ablation and drug release efficiencies. However, there are still several points need to be further improved in order to get more precise results. (1) Dynamic light scattering was used to measure and calculate the thickness of surface coatings. The hydrodynamic diameter may still have slight difference with the real thickness of the coatings due to the hydration effect, though it is more precise than normal TEM measurements in which the samples are dried on grids to give a totally different status as that in solutions. Though we assume the coating around a GNR has the same thickness, we still do not know if the coating is thicker on the sides than the tips or vice versa in the actual samples. Thus TEM graphs of samples frozen directly from the solution could be applied to study the actual coating thicknesses. (2) In the transient absorption measurements, GNRs in the solutions have orientations in all directions out of the circular laser plane, the laser pulses have a higher power intensity in the middle than at the edges, and GNRs in the samples also have certain polydispersity. All of these factors can result in different degrees of temperature increase in each GNR. Thus the transient absorption is detecting the average cooling rate of the GNRs in the whole sample. The elimination of these factors may be limited by the instrument techniques, but

single nanoparticle spectroscopy can be a promising way to solve at least some of these problems. (3) We calculated the average thermal properties of the layer-by-layer surface coatings, but these parameters should be different for each individual polyelectrolyte layer. Thus if we need to know the temperature among each layer, more detailed characterization and more complicated models should be applied. Of course the interfacial thermal conductance between each elements should also be considered. (4) Spatiotemporal temperature distribution around a GNR can be calculated with the above method theoretically, but there can also be more problems in a complicated drug delivery or photothermal therapy system than in such simple samples. Thus developing nanoscale molecular thermometers can be an alternative way to directly measure the temperature around a gold nanoparticle with either cw or pulsed laser irradiation to avoid the difficulties of building complicated models.

3.4 MATERIALS AND METHODS

Materials. Hydrogen tetrachloroaurate (III) hydrate ($HAuCl_4 \cdot 3H_2O$, 99.999%), sodium borohydride ($NaBH_4$, 99.99%), silver nitrate ($AgNO_3$, >99.0%), (poly(acrylic acid) sodium salt), M.W. ~15,000 (35 wt% solution in H_2O) (PAA), and polyallyamine hydrochloride, M.W. ~15,000 (PAH) were obtained from Aldrich. Cetyltrimethylammonium bromide (CTAB, >99%) and ascorbic acid ($C_6H_8O_6$, >99.0%) were purchased from Sigma Chemical. Sodium chloride (>99.0%) was obtained from Fischer Chemicals. All of these reagents were used without any further purification. All solutions were prepared using Barnstead E-Pure 18 MΩ water.

Synthesis of Gold Nanorods. Gold nanorods with aspect ratios ~3.8 were synthesized using a seed-mediated silver-assisted method.[30] At first, gold seeds with diameter ~2-4 nm were synthesized by adding 0.6 mL 0.01 M ice-cold $NaBH_4$ solution into a mixture of 0.25 mL 0.01 M $HAuCl_4$ aqueous solution and 9.75 mL 0.1 M cetyltrimethylammonium bromide (CTAB) aqueous solution, followed by vigorous stirring for 10 min. The prepared brownish gold seed solution stood for 30 min before use. GNR growth solutions were prepared by mixing 0.5 mL 0.01 M $HAuCl_4$ solution, 9.5 mL 0.1 M CTAB solution, and 0.1 mL 0.01 M $AgNO_3$ solution. Then 0.055 mL 0.1 M ascorbic acid solution as reducing agent was added into the growth solution, and 0.012 mL gold seed solution was added and the solution was allowed to stand overnight. The as-made GNR solution was purified twice by centrifugation at 11000 rpm for 20 min to remove excess surfactants and other reactants. The synthesis could be scaled up to 200 mL.

Preparation of Gold Nanorods in CTAB Solutions. GNRs in different concentrations of CTAB solutions were prepared by dispersing 0.05 mL of the twice-purified GNR pellet into 1.5 mL deionized water or into 0.001, 0.01, 0.1, 1, 10, 100 mM CTAB solutions.

Preparation of Gold Nanorods Coated with Polyelectrolyte Layers. GNRs coated with different layers of polyelectrolytes were prepared by the layer-by-layer absorption approach.[47] Solutions of 1 mL 0.01 M NaCl solution and 2 mL of 10 mg mL^{-1} poly(acrylic acid sodium salt) (PAA) or polyallylamine hydrochloride (PAH) (M.W. ~15,000) were added into 10 mL of 0.5 nM GNR solutions and shaken for 2 hours to coat the GNR surface with polyelectrolyte multilayers. After each coating step, samples was diluted to 20 mL with deionized water, purified by centrifugation at 8000 rpm for 20 min (Thermo Scientific Sorvall Legend X1centrifuge in a "swinging bucket" orientation) and re-dispersed in deionized water.

Characterization of Gold Nanorod Aqueous Solutions. The final GNR samples were characterized with UV-Vis absorption spectrometer, transmission electron microscopy, ζ-potential and dynamic light scattering measurements. Absorption spectra of the diluted samples with GNR concentration ~0.15 nM were taken on a Cary 500 scan UV−vis-NIR spectrophotometer. ζ-potential and dynamic light scattering measurements of samples with GNR concentrations of ~1 nM were taken on a Brookhaven ZetaPALS instrument. Transmission electron microscope images were taken on a JEOL 2100 Cryo TEM microscope at 200 kV accelerating voltage. TEM grids were prepared by drop-casting 15 μL of ~1 nM purified GNRs on a holey carbon TEM grid (Pacific Grid-Tech).

Transient Absorption Measurement. A mode-locked Ti:Sapphire laser that produces a series of <0.5 ps pulses at a repetition rate of 80 MHz was used for transmission measurement. The relative optical path lengths of pump beam and probe beam are adjusted via a mechanical delay stage. A 5X microscope objective lens was used to focus the pump and probe beams on the sample with the laser spot radius of 10.3 μm. Flat-sided capillary tubes with the inner dimension of 0.1×2 mm^2 were used as fluid cell for GNR suspensions. The pump and probe beam powers were set ~1.5 mW, and the wavelengths could be adjusted from 730 nm to 830 nm. Sharp edged optical filters (790 LP, 785 ± 1.5 BP, 780 SP, 770 SP from Omega Filters) were used to separate the pump and probe wavelengths as needed. The differences in transmitted probe intensity caused by the pump pulse appear at the f=9.8 MHz modulation frequency of the pump beam and were extracted with lock-in detection.[21–23] Two quarter-wave plates were fixed before the objective lens and photo-detector individually to change the linear polarized beam to circular polarized beam and back. Transient absorption measurements to determine the thermal decay of multilayer-coated GNRs was taken with both the pump and probe wavelengths tuned to the absorption peaks of the GNR samples.

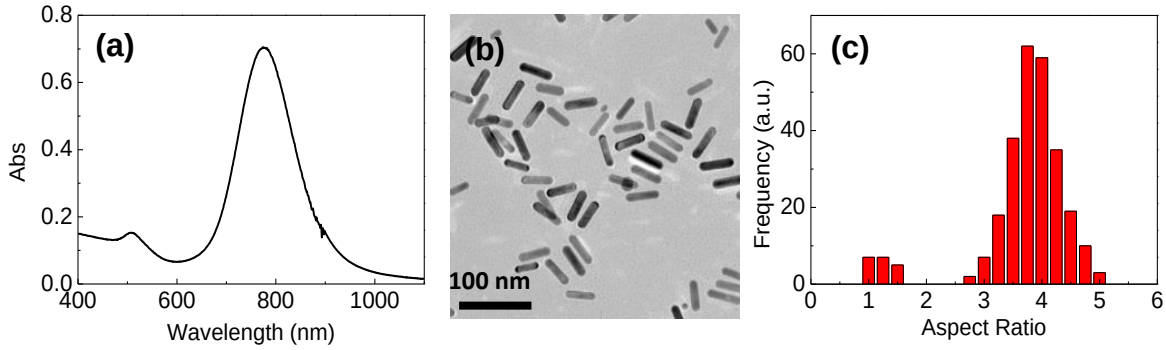

Figure 3.1 (a) UV-vis absorption spectrum of GNRs in aqueous solution. (b) Transmission electron micrograph (TEM) of the GNRs; the scale bar is 100 nm. (c) Distribution of the aspect ratios of GNRs as measured from TEM micrographs.

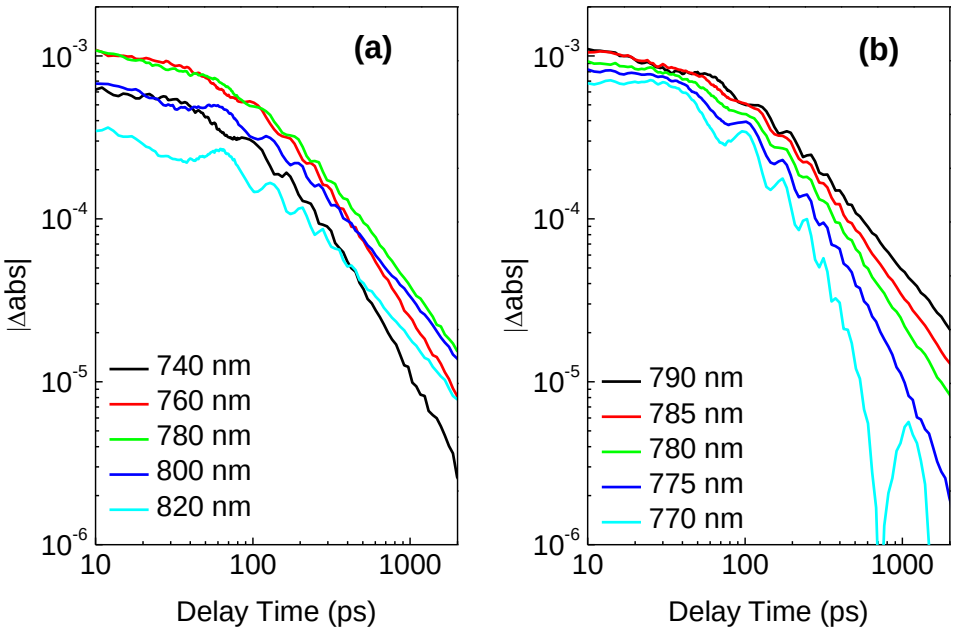

Figure 3.2 (a) Transient absorption of CTAB-coated GNRs in aqueous solution as a function of pump and probe wavelength, changed simultaneously. (b) Transient absorption of CTAB-coated GNRs in aqueous solution by fixing the pump wavelength at 790 nm and changing the probe wavelength from 790 nm to 770 nm. For the data at 770 nm, the transient absorption signal changes sign at a delay time of ≈700 ps.

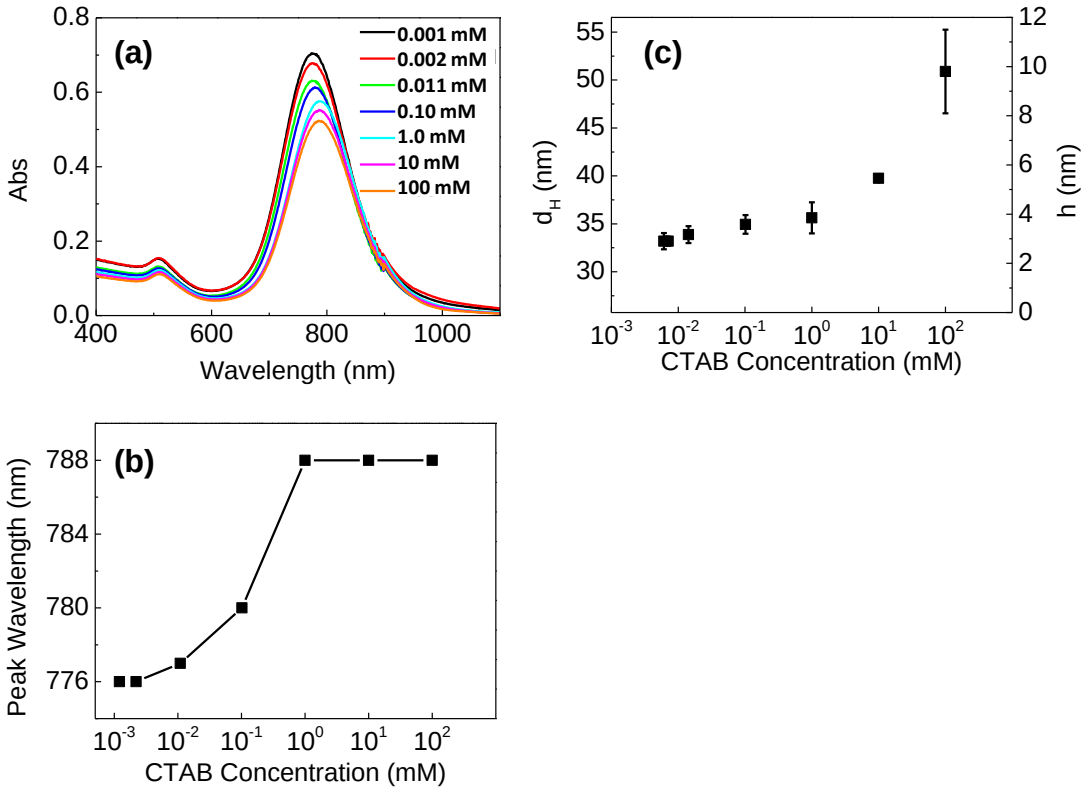

Figure 3.3 (a) UV-vis absorption spectra of ~0.15 nM GNRs in CTAB solutions with different estimated final CTAB concentrations. (b) Longitudinal plasmon peak maxima for ~ 0.15nM GNRs in CTAB solutions as a function of the estimated final CTAB concentrations in the solutions. (c) Effective hydrodynamic diameters (d_H) of ~1 nM GNRs in CTAB solutions measured by dynamic light scattering and equivalent thicknesses of CTAB bilayers (h) calculated from Eqs. 3.5-3.9 as a function of the estimated final CTAB concentrations in the solutions.

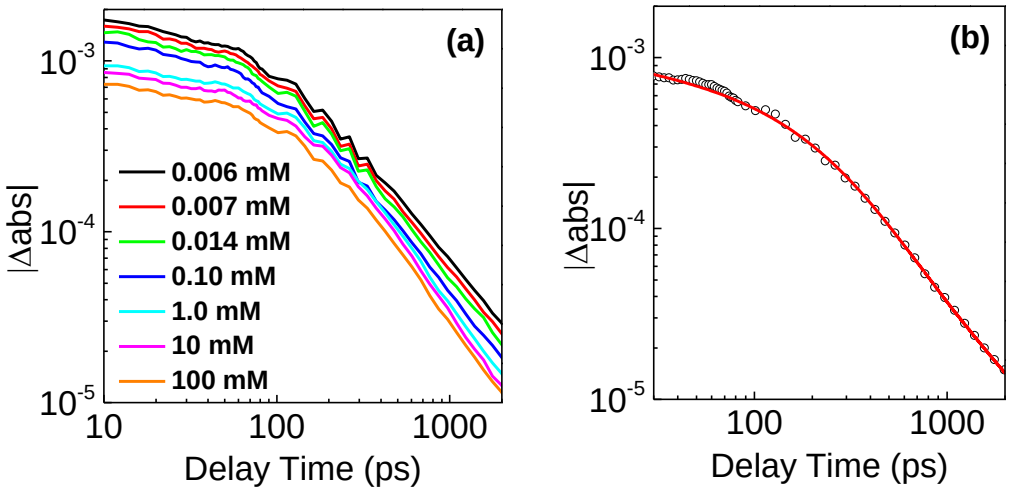

Figure 3.4 (a) Transient absorption of GNRs in CTAB solutions with different estimated final CTAB concentrations. (b) Circles: raw data of GNRs in 1 mM CTAB solution from pump-probe measurement; line: fitting for thermal conductivity of 0.18 W m^{-1} K^{-1} and volumetric heat capacity of 2.0 J cm^{-3} K^{-1} for the CTAB bilayer.

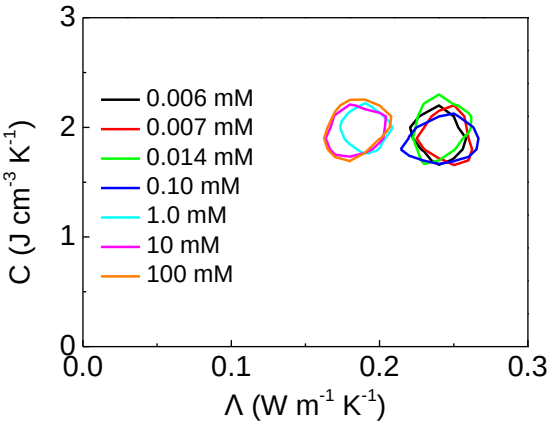

Figure 3.5 Data fitting for thermal conductivity and volumetric heat capacity of CTAB-coated GNRs in CTAB solutions. The contour edge indicates the Λ-C combinations that have a deviation between the fit and the data that is twice the minimum deviation.

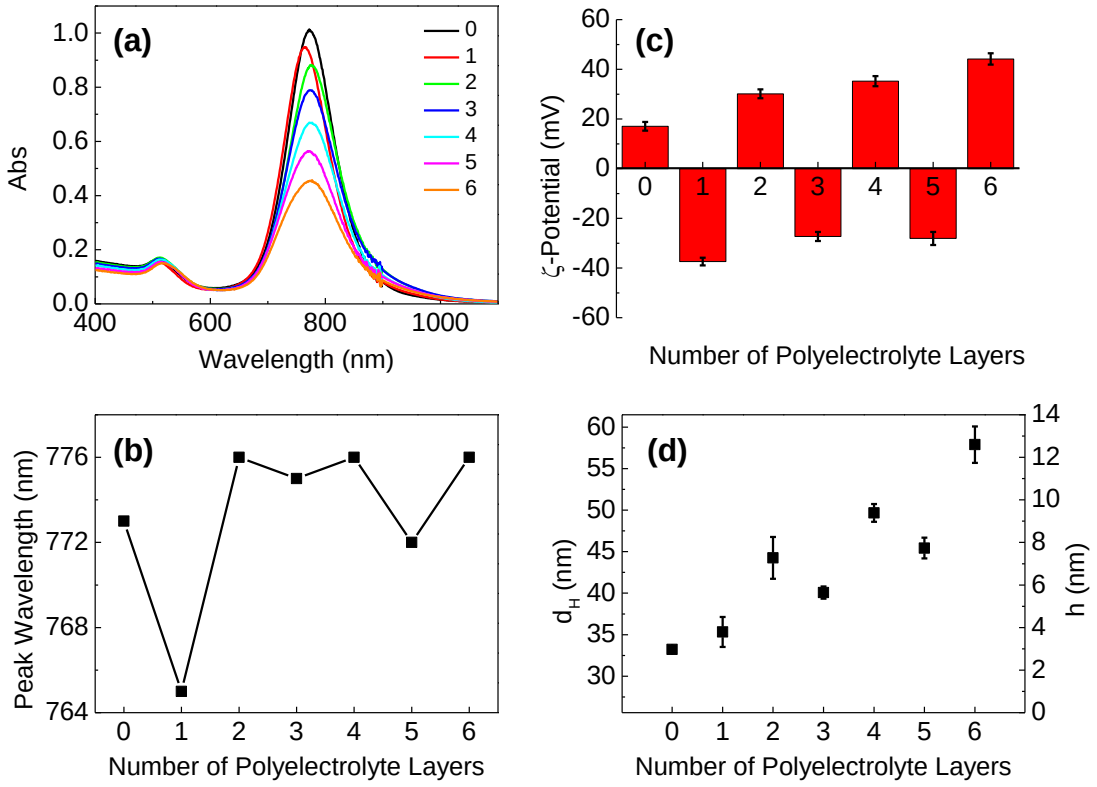

Figure 3.6 (a) UV-vis absorption spectra of GNRs with different numbers of PAA and PAH alternating polyelectrolyte coating layers (1, 3, 5=PAA; 2, 4, 6=PAH). The number of polyelectrolyte layer 0 refers to the as-prepared GNR pellets dispersed directly in water. (b) Longitudinal plasmon peak maxima for GNRs as a function of polyelectrolyte layers. (c) ζ-potential of GNRs as a function of polyelectrolye layers. (d) Effective hydrodynamic diameters (d_H) of GNRs with polyelectrolyte layers measured by dynamic light scattering and equivalent thicknesses (h) of polyelectrolyte layers calculated from Eqs. 3.5-3.9.

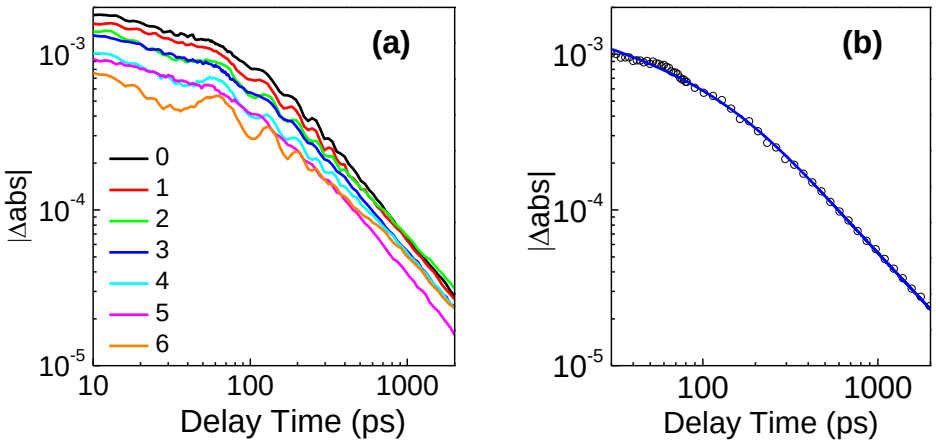

Figure 3.7 (a) Transient absorption of GNRs with different numbers of polyelectrolyte coating layers. (b) Circle: raw data of GNRs with 3 layers of polyelectrolyte coatings from pump-probe measurement; line: fitting for thermal conductivity of 0.38 W m^{-1} K^{-1} and volumetric heat capacity of 2.5 J cm^{-3} K^{-1} for polyelectrolyte layers.

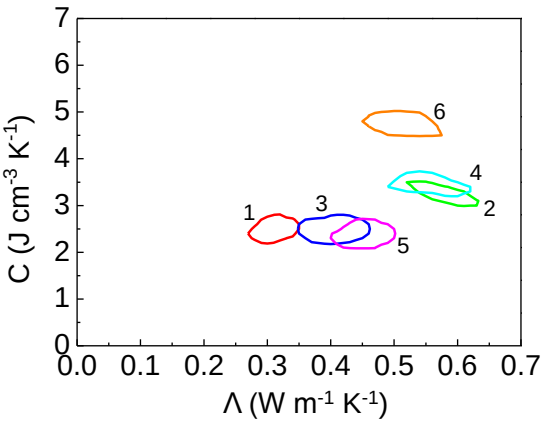

Figure 3.8 Data fitting for thermal conductivity and volumetric heat capacity of multilayer polyelectrolyte-coated GNRs in aqueous solutions. Layers 1, 3, 5 are PAA, and layers 2, 4, 6 are PAH. The contour indicates the Λ-C combinations that have twice as much as the minimum deviation between the raw data and fitted data.

3.5 REFERENCES

1. Murphy, C. J.; Sau, T. K.; Gole, A. M.; Orendorff, C. J.; Gao, J.; Gou, L.; Hunyadi, S. E.; Li, T. Anisotropic Metal Nanoparticles: Synthesis, Assembly, and Optical Applications. *J. Phys. Chem. B* **2005**, *109*, 13857–13870.
2. Murphy, C. J.; Thompson, L. B.; Chernak, D. J.; Yang, J. A.; Sivapalan, S. T.; Boulos, S. P.; Huang, J.; Alkilany, A. M.; Sisco, P. N. Gold Nanorod Crystal Growth: From Seed-mediated Synthesis to Nanoscale Sculpting. *Curr. Opin. in Colloid & Interface Sci.* **2011**, *16*, 128–134.
3. Huang, X.; Neretina, S.; El‐Sayed, M. A.; Huang, X.; Neretina, S.; El‐Sayed, M. A. Gold Nanorods: From Synthesis and Properties to Biological and Biomedical Applications. *Adv. Mater.* **2009**, *21*, 4880–4910.
4. Ekici, O.; Harrison, R. K.; Durr, N. J.; Eversole, D. S.; Lee, M.; Ben-Yakar, A. Thermal Analysis of Gold Nanorods Heated with Femtosecond Laser Pulses. *J. Phys. D: Appl. Phys.* **2008**, *41*, 185501.
5. Hartland, G. V. Optical Studies of Dynamics in Noble Metal Nanostructures. *Chem. Rev.* **2011**, *111*, 3858–3887.
6. Norman, R. S.; Stone, J. W.; Gole, A.; Murphy, C. J.; Sabo-Attwood, T. L. Targeted Photothermal Lysis of the Pathogenic Bacteria, Pseudomonas Aeruginosa, with Gold Nanorods. *Nano Lett.* **2008**, *8*, 302–306.
7. Bartczak, D.; Muskens, O. L.; Millar, T. M.; Sanchez-Elsner, T.; Kanaras, A. G. Laser-Induced Damage and Recovery of Plasmonically Targeted Human Endothelial Cells. *Nano Lett.* **2011**, *11*, 1358–1363.

8. Huang, Y.-F.; Sefah, K.; Bamrungsap, S.; Chang, H.-T.; Tan, W. Selective Photothermal Therapy for Mixed Cancer Cells Using Aptamer-conjugated Nanorods. *Langmuir* **2008**, *24*, 11860–11865.

9. Huang, J.; Jackson, K. S.; Murphy, C. J. Polyelectrolyte Wrapping Layers Control Rates of Photothermal Molecular Release from Gold Nanorods. *Nano Lett.* **2012**, *12*, 2982–2987.

10. Kuo, T.-R.; Hovhannisyan, V. A.; Chao, Y.-C.; Chao, S.-L.; Chiang, S.-J.; Lin, S.-J.; Dong, C.-Y.; Chen, C.-C. Multiple Release Kinetics of Targeted Drug from Gold Nanorod Embedded Polyelectrolyte Conjugates Induced by Near-infrared Laser Irradiation. *J. Am. Chem. Soc.* **2010**, *132*, 14163–14171.

11. Wijaya, A.; Schaffer, S. B.; Pallares, I. G.; Hamad-Schifferli, K. Selective Release of Multiple DNA Oligonucleotides from Gold Nanorods. *ACS Nano* **2008**, *3*, 80–86.

12. Huschka, R.; Zuloaga, J.; Knight, M. W.; Brown, L. V.; Nordlander, P.; Halas, N. J. Light-induced Release of DNA from Gold Nanoparticles: Nanoshells and Nanorods. *J. Am. Chem. Soc.* **2011**, *133*, 12247–12255.

13. Cahill, D. G.; Ford, W. K.; Goodson, K. E.; Mahan, G. D.; Majumdar, A.; Maris, H. J.; Merlin, R.; Phillpot, S. R. Nanoscale Thermal Transport. *Journal of Applied Physics* **2003**, *93*, 793–818.

14. Shakouri, A. Nanoscale Thermal Transport and Microrefrigerators on a Chip. *Proceedings of the IEEE* **2006**, *94*, 1613 –1638.

15. Adleman, J. R.; Boyd, D. A.; Goodwin, D. G.; Psaltis, D. Heterogenous Catalysis Mediated by Plasmon Heating. *Nano Lett.* **2009**, *9*, 4417–4423.

16. Christopher, P.; Xin, H.; Linic, S. Visible-light-enhanced Catalytic Oxidation Reactions on Plasmonic Silver Nanostructures. *Nature Chemistry* **2011**, *3*, 467–472.

17. Fasciani, C.; Alejo, C. J. B.; Grenier, M.; Netto-Ferreira, J. C.; Scaiano, J. C. High-Temperature Organic Reactions at Room Temperature Using Plasmon Excitation: Decomposition of Dicumyl Peroxide. *Org. Lett.* **2011**, *13*, 204–207.

18. Maity, S.; Downen, L. N.; Bochinski, J. R.; Clarke, L. I. Embedded Metal Nanoparticles as Localized Heat Sources: An Alternative Processing Approach for Complex Polymeric Materials. *Polymer* **2011**, *52*, 1674–1685.

19. Wang, Z.; Cahill, D. G.; Carter, J. A.; Koh, Y. K.; Lagutchev, A.; Seong, N.-H.; Dlott, D. D. Ultrafast Dynamics of Heat Flow Across Molecules. *Chem. Phys.* **2008**, *350*, 31–44.

20. Chen, S.; Lee, I. Y. S.; Tolbert, W. A.; Wen, X.; Dlott, D. D. Applications of Ultrafast Temperature Jump Spectroscopy to Condensed Phase Molecular Dynamics. *J. Phys. Chem.* **1992**, *96*, 7178–7186.

21. Wilson, O.; Hu, X.; Cahill, D.; Braun, P. Colloidal Metal Particles as Probes of Nanoscale Thermal Transport in Fluids. *Phys. Rev. B* **2002**, *66*, 224310.

22. Ge, Z.; Cahill, D. G.; Braun, P. V. AuPd metal nanoparticles as probes of nanoscale thermal transport in aqueous solution. *J. Phys. Chem. B* **2004**, *108*, 18870–18875.

23. Ge, Z.; Kang, Y.; Taton, T. A.; Braun, P. V.; Cahill, D. G. Thermal Transport in Au-Core Polymer-Shell Nanoparticles. *Nano Lett.* **2005**, *5*, 531–535.

24. Schmidt, A. J.; Alper, J. D.; Chiesa, M.; Chen, G.; Das, S. K.; Hamad-Schifferli, K. Probing the Gold Nanorod−Ligand−Solvent Interface by Plasmonic Absorption and Thermal Decay. *J.*

Phys. Chem. C **2008**, *112*, 13320–13323.

25. Alper, J.; Hamad-Schifferli, K. Effect of Ligands on Thermal Dissipation from Gold Nanorods. *Langmuir* **2010**, *26*, 3786–3789.

26. Juvé, V.; Scardamaglia, M.; Maioli, P.; Crut, A.; Merabia, S.; Joly, L.; Fatti, N. Del; Vallée, F. Cooling Dynamics and Thermal Interface Resistance of Glass-embedded Metal Nanoparticles. *Phys. Rev. B* **2009**, *80*, 195406.

27. Hu, M.; Wang, X.; Hartland, G. V.; Salgueiriño-Maceira, V.; Liz-Marzán, L. M. Heat Dissipation in Gold–silica Core-shell Nanoparticles. *Chem. Phys. Lett.* **2003**, *372*, 767–772.

28. Mark, J. E. *Physical Properties of Polymers Handbook*; Springer, **2006**, 145-163.

29. Pelton, M.; Liu, M.; Park, S.; Scherer, N. F.; Guyot-Sionnest, P. Ultrafast Resonant Optical Scattering from Single Gold Nanorods: Large Nonlinearities and Plasmon Saturation. *Phys. Rev. B* **2006**, *73*, 155419.

30. Sau, T. K.; Murphy, C. J. Seeded High Yield Synthesis of Short Au Nanorods in Aqueous Solution. *Langmuir* **2004**, *20*, 6414–6420.

31. Murphy, C. J.; Thompson, L. B.; Alkilany, A. M.; Sisco, P. N.; Boulos, S. P.; Sivapalan, S. T.; Yang, J. A.; Chernak, D. J.; Huang, J. The Many Faces of Gold Nanorods. *J. Phys. Chem. Lett.* **2010**, *1*, 2867–2875.

32. Petrova, H.; Perez Juste, J.; Pastoriza-Santos, I.; Hartland, G. V.; Liz-Marzán, L. M.; Mulvaney, P. On the Temperature Stability of Gold Nanorods: Comparison Between Thermal and Ultrafast Laser-induced Heating. *Phys. Chem. Chem. Phys.* **2006**, *8*, 814-821.

33. Kang, K.; Koh, Y. K.; Chiritescu, C.; Zheng, X.; Cahill, D. G. Two-tint Pump-probe

Measurements Using a Femtosecond Laser Oscillator and Sharp-edged Optical Filters. *Rev. Sci. Instrum.* **2008**, *79*, 114901-114904.

34. Sönnichsen, C.; Franzl, T.; Wilk, T.; Plessen, G. von; Feldmann, J.; Wilson, O.; Mulvaney, P. Drastic Reduction of Plasmon Damping in Gold Nanorods. *Phys. Rev. Lett.* **2002**, *88*, 077402.

35. Johnson, P. B.; Christy, R. W. Optical Constants of the Noble Metals. *Phys. Rev. B* **1972**, *6*, 4370–4379.

36. Cardinal, M. F.; Mongin, D.; Crut, A.; Maioli, P.; Rodríguez-González, B.; Pérez-Juste, J.; Liz-Marzán, L. M.; Fatti, N. Del; Vallée, F. Acoustic Vibrations in Bimetallic Au@Pd Core–Shell Nanorods. *J. Phys. Chem. Lett.* **2012**, *3*, 613–619.

37. Baida, H.; Mongin, D.; Christofilos, D.; Bachelier, G.; Crut, A.; Maioli, P.; Fatti, N. Del; Vallée, F. Ultrafast Nonlinear Optical Response of a Single Gold Nanorod Near Its Surface Plasmon Resonance. *Phys. Rev. Lett.* **2011**, *107*, 057402.

38. Link, S.; El-Sayed, M. A. Spectral Properties and Relaxation Dynamics of Surface Plasmon Electronic Oscillations in Gold and Silver Nanodots and Nanorods. *J. Phys. Chem. B* **1999**, *103*, 8410–8426.

39. Uematsu, M.; Frank, E. U. Static Dielectric Constant of Water and Steam. *J. Phys. Chem. Ref. Data* **1980**, *9*, 1291–1306.

40. Link, S.; Mohamed, M. B.; El-Sayed, M. A. Simulation of the Optical Absorption Spectra of Gold Nanorods as a Function of Their Aspect Ratio and the Effect of the Medium Dielectric Constant. *J. Phys. Chem. B* **1999**, *103*, 3073–3077.

41. Alkilany, A. M.; Nagaria, P. K.; Wyatt, M. D.; Murphy, C. J. Cation Exchange on the Surface

of Gold Nanorods with a Polymerizable Surfactant: Polymerization, Stability, and Toxicity Evaluation. *Langmuir* **2010**, *26*, 9328–9333.

42. Ming, T.; Kou, X.; Chen, H.; Wang, T.; Tam, H.-L.; Cheah, K.-W.; Chen, J.-Y.; Wang, J. Ordered Gold Nanostructure Assemblies Formed By Droplet Evaporation. *Angew. Chem. Int. Ed.* **2008**, *47*, 9685–9690.

43. Hamon, C.; Postic, M.; Mazari, E.; Bizien, T.; Dupuis, C.; Even-Hernandez, P.; Jimenez, A.; Courbin, L.; Gosse, C.; Artzner, F. *et al.* Three-Dimensional Self-Assembling of Gold Nanorods with Controlled Macroscopic Shape and Local Smectic B Order. *ACS Nano* **2012**, *6*, 4137–4146.

44. Rodr ́guez-Fernández, J.; Pérez−Juste, J.; Liz−Marzán, L. M.; Lang, P. R. Dynamic Light Scattering of Short Au Rods with Low Aspect Ratios. *J. Phys. Chem. C* **2007**, *111*, 5020–5025.

45. Ortega, A.; García de la Torre, J. Hydrodynamic Properties of Rodlike and Disklike Particles in Dilute Solution. *J. Chem. Phys.* **2003**, *119*, 9914-9919.

46. Dashora, P.; Gupta, G. On the Temperature Dependence of the Thermal Conductivity of Linear Amorphous Polymers. *Polymer* **1996**, *37*, 231–234.

47. Gole, A.; Murphy, C. J. Polyelectrolyte-coated gold nanorods : Synthesis, characterization and immobilization. *Chem. Mater.* **2005**, *17*, 1325–1330.

48. L ösche, M.; Schmitt, J.; Decher, G.; Bouwman, W. G.; Kjaer, K. Detailed Structure of Molecularly Thin Polyelectrolyte Multilayer Films on Solid Substrates as Revealed by Neutron Reflectometry. *Macromolecules* **1998**, *31*, 8893–8906.

49. Wong, J. E.; Rehfeldt, F.; Hänni, P.; Tanaka, M.; Klitzing, R. V. Swelling Behavior of Polyelectrolyte Multilayers in Saturated Water Vapor. *Macromolecules* **2004**, *37*, 7285–7289.

50. McCormick, M.; Smith, R. N.; Graf, R.; Barrett, C. J.; Reven, L.; Spiess, H. W. NMR Studies of the Effect of Adsorbed Water on Polyelectrolyte Multilayer Films in the Solid State. *Macromolecules* **2003**, *36*, 3616–3625.

51. Schlenoff, J. B.; Rmaile, A. H.; Bucur, C. B. Hydration Contributions to Association in Polyelectrolyte Multilayers and Complexes: Visualizing Hydrophobicity. *J. Am. Chem. Soc.* **2008**, *130*, 13589–13597.

52. Schwarz, B.; Schönhoff, M. Surface Potential Driven Swelling of Polyelectrolyte Multilayers. *Langmuir* **2002**, *18*, 2964–2966.

53. Liu, X.; Goli, K. K.; Genzer, J.; Rojas, O. J. Multilayers of Weak Polyelectrolytes of Low and High Molecular Mass Assembled on Polypropylene and Self-Assembled Hydrophobic Surfaces. *Langmuir* **2011**, *27*, 4541–4550.

54. Lehaf, A. M.; Moussallem, M. D.; Schlenoff, J. B. Correlating the Compliance and Permeability of Photo-Cross-Linked Polyelectrolyte Multilayers. *Langmuir* **2011**, *27*, 4756–4763.

CHAPTER 4

RESONANT SECONDARY LIGHT EMISSION FROM PLASMONIC Au NANOSTRUCTURES AT HIGH ELECTRON TEMPERATURES CREATED BY PULSED LASER EXCITATION

4.1 INTRODUCTION

The unique optical properties of Au and Ag nanostructures have enabled a wide variety of innovations in optical detection, sensing, and imaging.[1] Two of the most important and widely studied of these applications involve the emission of light at a different wavelength than the excitation, i.e., secondary light emission: i) sensing of molecular layers by surface-enhanced Raman scattering (SERS)[2,3] ; and ii) imaging of biological microstructures using light emission generated by ultrafast laser pulses, a process often referred to as two-photon luminescence (TPL)[4,5].

A common limitation of SERS for sensing adsorbed species is the background[6] that appears as a broad continuum of light emission underlying the desired signal generated by the vibrational modes of the adsorbed molecules. This background is often attributed to unintentional fluorescence by impurities although processes involving photoluminescence of the substrate[7,8]; electronic Raman scattering by localized surface electronic states associated with the molecule/metal chemical bond[9,10] have also been invoked.

This chapter is reprinted with permission from Jingyu Huang, Wei Wang, Catherine J. Murphy and David G. Cahill, *Proc. Natl. Acad. Sci. U.S.A.* 2014, 111(3): 906-911. (DOI: 10.1073/pnas.1311477111)

The quantum efficiency of TPL from metal nanoparticles is small compared to a molecular bleaching or blinking.[5] The benefit of two-photon excitation is an improvement of the spatial resolution over what can typically be achieved by confocal fluorescence imaging. Proposed mechanisms for luminescence from Au or Ag nanostructures include fluorescence by interband transitions[11-17], intraband transitions[18] and radiative decay of surface plasmons[19-22].

The electromagnetic resonance of Au or Ag nanostructures are thought to play a critical role in both the background in SERS and the emission typically described as TPL. In the language of quantum mechanics, the optical process for the annihilation of an incident photon and the creation of an emitted photon involves a resonance with a plasmon; therefore, light emission by plasmonic nanostructures is a type of resonant secondary emission. The interpretation of resonant secondary light emission in terms of fundamental processes has been controversial for 40 years. Klein, and Solin and Merkelo argued that resonant Raman scattering and hot luminescence are formally equivalent[23-25]. Shen countered[26-27] that emission can be broken down into a Raman scattering component and a luminescence component[28-29] based on the longitudinal and transverse relaxation times. In a 1991 review, Kono and co-workers found a similar division into "Raman-like" and "fluorescence-like" components of the secondary emission[30].

We do not attempt to address this controversy directly but instead point out that resonant electronic Raman scattering and resonant fluorescence may both be useful descriptions of the secondary emission. An important conclusion of our work is, however, that blue-shifted secondary emission generated by pulsed laser excitation at a plasmon resonance in the

near-infrared is not the result of a two-photon absorption followed by radiative decay of a plasmon and is instead better described by electronic Raman scattering from single-particle electron-hole pair excitations[31,32] of the Au or Ag metal that are resonantly enhanced by the plasmon. (In a classic study published nearly 50 years ago, Kawabata and Kubo[33] described the mechanisms by which a plasmon decays by transferring energy to electron-hole pairs.) In particular, the changes in the anti-Stokes spectra with the energy and duration of the ultrafast laser pulse are quantitatively predicted by a two-temperature model; and the time-scale of the non-linearity is consistent with the cooling time of hot-electrons.

4.2 RESULTS AND DISCUSSION

Figure 4.1 compares the optical absorption spectra and the spectra of light emission using 488 nm cw laser excitations for aqueous suspensions of AuNRs with three aspect ratios. To facilitate this comparison, we use a common *x*-axis for both plots; since we will argue that the light emission by the AuNRs can be described by a resonant Raman scattering process, we label the *x*-axis of both plots "Raman shift". The corresponding wavelength for absorption or emission is given on the top axis. Raman scattering by the band of OH stretching vibrations of water is the dominant feature near a shift of 3300 cm^{-1}. The spectra of light emission from all three AuNR suspensions show a broad peak near 525 nm. For aspect ratios of 2.3 and 3.8, the spectra also show a broad peak at longer wavelengths that corresponds to the position of the peak absorption created by the longitudinal plasmon resonance. The ratio of scattering cross-section and

absorption cross-section of the AuNRs of our dimensions is smaller than 0.05,[34] thus the y-axis in Fig. 4.1A can be approximately set as absorbance instead of extinction.

The similarity of the optical absorption and light emission spectra of AuNR has been noted before[13,18,20,21] and is typically attributed to light emission associated with the plasmon resonance of the AuNR.[20,21] The proposed mechanisms of the luminescence involve i) the creation of energetic electron-hole pairs by the 488 nm photon; ii) the relaxation of these electron-hole pairs by excitation of the collective longitudinal plasmon; iii) radiative decay of the longitudinal plasmon by emission of near infrared photons.

Inspired by Klein's assertion of the equivalence of hot luminescence and resonant Raman scattering[23], we assert that the secondary light emission under 488 nm excitation is equally well described by Raman scattering by a broad spectrum of single-particle electron-hole excitations and that the peak observed in the spectra is the result of the enhancements of the electric fields of the scattered radiation by the plasmon resonance of the AuNR. In the usual situation where the spectrum of excitations is sharp and the resonance effects are weakly dependent on wavelength, the wavelength of the Raman scattered light will shift with the excitation wavelength. The system we are studying is the opposite: the spectrum of excitations is broad and the resonance effects have a strong dependence on wavelength. Since the plasmon resonance is fixed by the geometry of the AuNR, a change in the excitation wavelength will not change the peak position. Further support for this description comes from prior studies[13,18,20,21] which employed varying excitation wavelengths and found that the emission peak of AuNRs overlapped with the optical

absorption or dark-field scattering peak.

We next focus our attention on the largest aspect-ratio AuNR that have a resonance that was intentionally tuned to be close to the wavelength of operation of the Ti:sapphire laser oscillator. Fig. 4.2A compares the Raman scattering spectra from AuNRs excited by cw and pulsed laser excitation at 785 nm. The y-axis of these plots has been normalized by the average power of the excitation laser and the data acquisition time, i.e., the y-axis shows the intensity of scattered light normalized by the incident photon flux. The cw mode excitation produces a narrow anti-Stoke spectrum and a broad Stokes spectrum which does not change with the average power of the excitation laser. This indicates that the emission process is linear when the excitation laser is operated in cw mode. The anti-Stokes data is well-described by a thermal population of excitations with a characteristic temperature of 300 K.

With pulsed laser excitation, however, the spectra become significantly more intense, broaden dramatically on the anti-Stokes side of the spectra, and depend on the laser pulse duration and average power. The emission is thus a nonlinear function of the incident photon flux. For spectra obtained with pulses of 0.45 ps duration, and a change in laser power of a factor of 4, the normalized anti-Stokes intensity increases by a factor of ≈3 at small energy shifts (-250 cm^{-1}) and by a factor of ≈4 at large energy shifts (-1000 cm^{-1}).

The non-linear relationship between the spectral intensity *S* and the average power *P* of the pulsed laser excitation on the anti-Stokes side is emphasized further in Fig. 4.2B and 4.2C. We

believe that this non-linearity, which is approximately quadratic, has been often misinterpreted as signature of non-linear optical absorption via two-photon excitation of interband transitions[17] followed by fluorescence. We argue that this non-linear optical response is explained by a high temperature distribution of electron-hole excitations created by the short laser pulses and is not the signature of a direct optical non-linearity. In the language of Raman scattering, the strength of the scattering is high because both the incident and scattered fields are enhanced by the electromagnetic resonance of the AuNR.

Furthermore, the intensity does not scale quadratically with the average laser intensity. At constant energy per pulse, we calculate that changing the pulse duration from 0.45 ps to 1.3 ps, decreases the integral of the square of the intensity by a factor of ≈3.5. An emission process that was initiated by two-photon absorption should therefore decrease in intensity by a factor of 3.5 when the pulse duration is broadened. In our experiments, broadening the pulse duration reduces the emission intensity by a factor of only ≈1.5.

To further test the role of the plasmon resonance, we also collected emission spectra of AuNRs with smaller aspect ratios excited by 785 nm laser pulses with an average power of 1 mW, see Fig. 4.3. Spectra for AuNRs with longitudinal plasmon resonances at 523 nm and 647 nm have much lower intensities because of the low enhancement factors, and the low optical cross-section that results in low electronic temperatures. (We could not measure emission spectra for these non-resonant AuNRs using cw excitation at 785 nm because the signals are too weak for our apparatus to detect reliably.)

We approximately describe the intensity $S(\Delta\omega)$ of anti-Stokes electronic Raman scattering by the electron-hole excitations of the AuNR by the following equation[35,36]:

$$S(\Delta\omega) = f\beta\int P(t)n(\Delta\omega,t)dt\,, \qquad \beta = \sigma_{S,I}{g_S}^2{g_I}^2 \tag{4.1}$$

where $P(t)$ is the laser intensity of an individual laser pulse as a function of time t; f=80 MHz is repetition rate of laser pulse; $n(\Delta\omega,t)$ is the time-dependent electron-hole occupation number; $\sigma_{S,I}$ is the Raman cross section of AuNR at the incident and scattering light frequencies; g_S is the Raman enhancement factor for the scattered light; and g_I is the Raman enhancement factor for the incident light. We define the sign of the Raman frequency shift $\Delta\omega$ as a negative value on the anti-Stokes side of the spectra and positive on the Stokes side.

The time-dependent electron-hole occupation number is:

$$n(\Delta\omega,t) = \frac{1}{\exp\left(-hc\Delta\omega / k_B T_e(t)\right) - 1} \tag{4.2}$$

where $T_e(t)$ is time-dependent electronic temperature of AuNRs; h is Planck constant; and c is the speed of light. In cw mode, $T_e(t)$=T_0=300 K. In pulsed mode, $T_e(t)$ greatly exceeds T_0 during the optical pulse.

We cannot determine $T_e(t)$ experimentally and instead focus our attention on an effective temperature T_{eff} for the scattering process that we can derive from the data. We define T_{eff} [37] by equating the integral of the time dependent scattering intensity to the scattering intensity that

would be created by a constant electronic temperature. T_{eff} can be thought of as a time average of $T_e(t)$ that is weighted by the emission intensity.

$$\frac{Q}{\exp(-hc\Delta\omega / k_B T_{eff}) - 1} = \int \frac{P(t)dt}{\exp(-hc\Delta\omega / k_B T_e(t)) - 1} \tag{4.3}$$

where $Q = \int P(t)dt$ is the total energy in one laser pulse.

Equation 4.3 describes how we derive a prediction for T_{eff} from a model for $T_e(t)$. We extract an experimental value for T_{eff} from the data by dividing the intensity generated by pulsed laser excitation by the intensity generated by cw laser excitation.

$$\frac{\exp(-hc\Delta\omega / k_B T_0) - 1}{\exp(-hc\Delta\omega / k_B T_{eff}) - 1} = \frac{S(\Delta\omega)_{pulsed}}{S(\Delta\omega)_{cw}} \tag{4.4}$$

This approach has the advantage of eliminating the Raman enhancement factors, Raman cross-sections, and the calibration of the spectrometer from the analysis at the same Raman shift; but has the disadvantage of giving a different value of T_{eff} for every value of the Raman shift. Data for the change in the effective temperature $\Delta T_{eff} = T_{eff} - T_0$ as a function of average laser power of the pulsed laser are summarized in Fig. 4.4A and 4.4B.

The effective temperature on the Stokes side is defined in the same way and can also be calculated using Eq. 4.4. For Stokes scattering, n is replaced by n+1 in Eq. 4.1; Eqs. 4.3 and 4.4 are valid for Stokes scattering where $\Delta\omega > 0$. ΔT_{eff} derived from the data deviates from the prediction at average laser power >1 mW with 0.45 ps pulses and at average laser power >2 mW

with 1.3 ps pulses.

To make this analysis more quantitative, we employ a conventional two-temperature model to predict how the electron temperature varies as a function of time during the laser pulse. In the two-temperature model, the electron-hole excitations of the metal are assumed to have a thermal distribution characterized by a temperature $T_e(t)$. Since we are only interested in the electronic temperature, and the heat capacity of the phonons is large compared to the heat capacity of the electronic system, we do not consider time variations of the phonon temperatures and set T_0=300 K, independent of time.

$$C_e \frac{dT_e(t)}{dt} = \frac{P(t)\sigma_{abs}}{\pi r_0^2 V} - g\left(T_e(t) - T_0\right) \quad , \qquad C_e(t) = \gamma T_e(t) \tag{4.5}$$

In Eq. 4.5, C_e is the volumetric heat capacity of electrons; γ=66 J m^{-3} K^{-2} is a constant[38]; σ_{abs} is the AuNR optical absorption cross-section of the AuNR; r_0=4.7 μm is the $1/e^2$ intensity radius of the focused laser spot radius; V is the AuNR volume; and g=3.0×10^{16} W m^{-3} K^{-1} is the electron-phonon coupling parameter for Au[38]. In our experiments, we measured the temporal shape of the laser pulse using a conventional autocorrelator. The autocorrelation has a full-width-at-half-maximum of 0.65 ps and is described well by a Gaussian pulse shape, see Eq. 4.6. $P(t)$ is the time-dependent laser power intensity in one laser pulse that appears in Eqs. 4.5 and 4.8. We were unable to measure the autocorrelation of the pulse after the etalon and therefore used two photon-absorption in a GaP detector to measure the correlation of the pulse after the etalon with a much shorter pulse that does not pass through the etalon. We determine the

pulse shape after the etalon by convoluting the correlation. The resulting pulse shape is fit by a phenomenological equation that combines a broadened onset with an exponential decay, see Eq. 4.7.

$$P(t) = \frac{Q}{\xi\sqrt{2\pi}} \exp\left(-\frac{t^2}{2\xi^2}\right) \tag{4.6}$$

$$P(t) = \frac{Q}{\eta} \frac{\exp(-t/\tau_1)}{\exp(-t/\tau_2)+1} \tag{4.7}$$

In Eq. 4.6, the pulse has a Gaussian shape, Q is the energy in one laser pulse, r_0 is the $1/e^2$ intensity radius of the focused laser spot radius, and ξ=0.19 ps is the temporal standard deviation of the pulse. This choice of ξ is equivalent to a full-width-at-half-maximum of 0.45 ps and an autocorrelation time 0.65 ps. We also calculated the fitting with a sech^2 shape pulse with the same autocorrelation time 0.65 ps, which generates a FWHM of 0.45 ps; the calculation of ΔT_{eff} shows nearly no difference from the calculation using a Gaussian shape pulse. Pulses that travel through the etalon are described by Eq. 4.7 with τ_1=1.2 ps, τ_2=0.1 ps, and η=1.245 ps. The FWHM of these pulses is 1.3 ps. The temporal pulse shapes of these two cases are plotted as Fig. 4.5A and the evolution of electron temperature for the two cases are plotted as Fig. 4.5B.

$T_e(t)$ is calculated numerically by integrating Eq. 4.5. Examples of calculated values of $T_e(t)$ are plotted as Fig. 4.5B. The ratio of scattered light produced by pulsed and cw excitation in each pulse cycle of 12.5 ns is then:

$$\frac{S(\Delta\omega)_{pulsed}}{S(\Delta\omega)_{cw}} = \frac{\int_{-6.25ns}^{6.25ns} P(t)n(\Delta\omega,t)_{pulsed}\,dt}{Qn(\Delta\omega)_{cw}} = \frac{\int_{-6.25ns}^{6.25ns} P(t)/\left[\exp\left(-hc\Delta\omega/k_B T_e(t)\right)-1\right]dt}{Q/\left[\exp\left(-hc\Delta\omega/k_B T_0\right)-1\right]} \quad (4.8)$$

We treat σ_{abs} as an adjustable parameter in Eq. 4.5 and find that σ_{abs}=2700 nm^2 produces the best fit for the pulsed vs. cw ratio between the anti-Stokes data and the model at low average laser power at 0.45 ps pulse excitations. The calculated ratio using the same σ_{abs} value also agrees well with the anti-Stokes data at 1.3 ps pulse excitations. We use the anti-Stokes side of the spectra in this fit because the anti-Stokes data provide greater sensitivity to T_{eff} than the Stokes data. The results of the calculation using σ_{abs}=2700 nm^2 to calculate $T_e(t)$ from Eq. 4.5, and therefore the ratio of pulsed vs. cw spectra intensity as a function of frequency shift and laser power using Eq. 4.8, are shown in Fig. 4.6.

Once σ_{abs} is fixed, and therefore $T_e(t)$ can be calculated from the two-temperature model, we calculate ΔT_{eff} using Eq. 4.4. These predictions for ΔT_{eff} are compared to ΔT_{eff} derived from the experiment in Fig. 4A and 4B. At low laser powers, the predictions agree closely with experiment for both pulse durations and both the anti-Stokes and Stokes side of the spectra. At high laser power, the experimental value for ΔT_{eff} exceeds the predictions. The deviation of the data from the prediction is larger for short pulse duration and larger on the Stokes side of the spectra than the anti-Stokes side of the spectra. We speculate on the origin of these discrepancies at high electron temperature below.

Predicted values of σ_{abs} using the discrete dipole approximation (DDA) method are

σ_{abs}=3800 nm^2 for 44×10.7 nm^2 AuNRs[39] and σ_{abs}=4700 nm^2 for 48×12.2 nm^2 AuNRs[34] for linearly polarized light oriented with the electric field vector along the long-axis of the AuNR. For circularly polarized light, the maximum optical absorption cross section is reduced by a factor of 2. Thus, the expected values of the maximum possible cross-sections and the value of σ_{abs}=2700 nm^2 we used to fit the anti-Stokes data agree to within a factor of 2 and we conclude that both the intensity of the scattering and the changes in the scattering with laser power are adequately described by a two-temperature model.

We do not expect better agreement between the predicted and fitted cross-sections because of the non-linearity of the light emission and the multiple inhomogeneities in the experiment: i) polydispersity of the aspect-ratio of the AuNR; ii) the Gaussian spatial profile of the excitation laser; and iii) the three-dimensional random orientations of the AuNRs. The polydispersity and three-dimensional orientations of AuNRs will tend to decrease the apparent cross-section; the Gaussian profile of the excitation laser will tend to increase the apparent cross-section because of the factor of 2 larger intensity (and therefore higher electronic temperatures) at the center of the beam compared to the average intensity calculated using an effective beam area of πr_0^2.

In Fig. 4.4C and 4.4D, we make a more detailed comparison between measured and calculated ΔT_{eff} at the Raman shifts of -500 and 500 cm^{-1}. We do not yet understand the origin of the discrepancy at high average laser power and speculate that the cross-section for secondary emission increases for some reason at higher electronic temperatures. The strong enhancement of emission on the Stokes side of the spectra relative to the prediction of Raman scattering by single

electron-hole pairs suggests to us that higher-order processes are involved. These higher-order processes may be analogous to multi-phonon resonant Raman scattering that is often observed when the excitation photon energy exceeds the band gap of a semiconductor. [23,40]

We directly determined the time-scale for the non-linearity of the light emission using a pair of ultrafast excitation pulses at 785 nm separated by a variable time delay. In this experiment, the laser pulse is in Gaussian shape with 0.45 ps duration, and the total average power is 1 mW, i.e., the average power carried by each of the excitation pulses is 0.5 mW. The relative values of the intensity integrated over a 200 cm^{-1} range centered at -500 cm cm^{-1} and 900 cm^{-1} are plotted in Fig. 5 as a function of the delay time τ. The y-axis of Fig. 5 is the intensity of the light emission as a function of the delay time, normalized by the intensity when the pulse separation is -10 ps. The ratio of the intensity with overlapping pulses (τ=0) to the intensity with well-separated pulses (τ=-10 ps) is ≈1.6 for intermediate Raman shifts (-400 to -600 cm^{-1}) and ≈1.8 for large Raman shifts (-800 to -1000 cm^{-1}).

The emission spectra in Fig. 4.7B are excited by two 0.45 ps laser pulses at different delay times. The spectrum intensity increase when the two laser pulses become more overlapped in time. Data presented in Fig. 4.7A are calculated based on the integrated intensity ratio at a certain delay time vs. -10 ps delay time either in -400 to -600 cm^{-1} range or -800 to -1000 cm^{-1} range.

We model the scattered intensity by a two pulse excitation using extensions of the models

presented above. The time-dependent electronic temperature calculation of Eq. 4.5 is modified by including two laser pulses separated by delay time of τ. The relative ERS intensity at the Raman shift $\Delta\omega$ and delay time τ is then:

$$S(\Delta\omega,\tau) = f\beta \int_{-6.25\text{ ns}}^{6.25\text{ ns}} \frac{P(t)+P(t+\tau)}{\exp\left(-hc\Delta\omega / k_B T_e(t,\tau)\right)-1}\, dt \tag{4.9}$$

The calculated intensity ratio at various delay times τ vs. τ =-10 ps is plotted in Fig. 5 as solid lines. The model closely resembles the experimental results but there are discrepancies: in particular, while the decay rates of the signal as a function τ are similar for experiment and theory, the experimental data are more sharply peaked than the model.

In this modeling, we are making the standard assumption within the two temperature model that the occupation of the electronic excitations is well-described by an equilibrium distribution of temperature T_e. However, both the generation of electron-hole pairs and the coupling of electronic excitations to the lattice will cause the distribution to deviate from equilibrium. Since the electron-electron scattering time is short compared to the electron thermalization time (10's of femtoseconds vs. picoseconds), this deviation from equilibrium is usually assumed to be small[41] but we point out that the equilibration time of electronic excitations becomes significantly longer than the electron-electron scattering time as the excess energy decreases.[42] It is possible that deviations from a thermal distribution are revealed in this type of two-pulse experiment but a quantitative treatment of these effects is beyond the scope of the present work.

In conclusion, we propose that resonant electronic Raman scattering from the continuum electron-hole pairs provides a useful description of secondary light emission from a model Au nanostructure. The peak of emission that is usually attributed to radiative decay of plasmons is described by the enhancement of the Raman scattered light by the electromagnetic resonance. The non-linear light emission usually attributed to two-photon absorption followed by fluorescence is quantitatively described by a broad spectrum of anti-Stokes electronic Raman scattering created by high electronic temperatures. The time-scale of the non-linearity is consistent with the time-scale for the exchange of thermal energy between the electronic system and the lattice.

4.3 FUTURE WORK

Electronic Raman scattering theory for the explanation of resonant secondary light emission from plasmonic gold nanorods in aqueous solution was supported by experiments quantitatively in this work. (1) There are still problems with unevenly heating of gold nanorods in the solution due to the same reasons that have been discussed in section 3.3. Thus we used a reasonable average absorption cross section of gold nanorod in the calculations. To get a higher resolution, nanorods oriented in the incident laser plane should be used, or single nanoparticle spectroscopy could also eliminate these concerns. The study of other kinds of plasmonic nanoparticles in different environments can be further tested to verify the electronic Raman scattering theory. (2) At the same time, we also get more knowledge about the broad continuum background underlying the sharp Raman peaks in SERS measurements. Increasing laser pulse duration or

decreasing laser power can effectively reduce the intensity of SERS background when using a pulsed laser as excitation source. Thus nanoscale molecular thermometers as indicated in section 3.3 based on SERS signals could be improved to get a larger signal to noise ratio by minimizing the background underlying the Raman peaks if using laser pulse irradiation. (3) One thing we may need to notice is that gold nanorod itself may also be promising to be used as nanothermometer, since we know the emission spectrum of gold nanorod, especially on the anti-Stokes side, changes with its electron temperature. In this way, gold nanorods can be used to indicate its steady state surrounding temperature, because both the electron and lattice temperatures of a gold nanorod should be the same as the surrounding. Low power cw laser rather than pulsed laser should be used to excite the gold nanorods, so that the heating effect from the excitation laser itself can be minimized.

4.4 MATERIALS AND METHODS

We synthesized Au nanorods (AuNRs) with average aspect ratios of 1.2 ± 0.2, 2.3 ± 0.3, and 3.8 ± 0.4 using the methods described previously[43]. The AuNRs are subsequently coated with poly(acrylic acid)[44] to increase their thermal stability in aqueous solution during laser heating[45]. A quartz cuvette with optical path length of 200 μm is used as the sample holder for the optical measurements.

All three aspect ratios of AuNRs were studied using a conventional Raman spectrometer with 488 nm cw excitation. (For all of the data reported below, the AuNR suspensions are at room temperature.) The microscope objective that focuses the incident light and collects the scattered light has a numerical aperture of 0.17. AuNRs with an average aspect-ratio of 3.8, dimension of 47×12.5 nm^2, and longitudinal surface plasmon resonance (SPR) peak at 787 nm were studied more extensively with a second custom-built Raman spectrometer that uses a Ti:sapphire laser as the excitation source[46]. A 10× microscope objective lens with a numerical aperture of 0.25 is used to focus the laser on the sample with a $1/e^2$ intensity radius of ≈ 4.7 μm. The laser can be operated in either cw or pulsed mode with a repetition frequency of 80 MHz. The spectrum of the excitation pulses is limited to 785 ± 1.5 nm by a bandpass optical filter. Due to dispersion of optical elements, the full-width-at-half-maximum (FWHM) duration of the laser pulses is ≈ 0.45 ps. In a second set of experiments, we placed a Fabry–Pérot etalon after the bandpass optical filter to broaden the pulse to produce a FWHM of ≈ 1.3 ps. We include details about the pulse durations and shapes in the section 4 of supplemental information.

We illuminate the sample using circularly polarized light to improve the homogeneity of the energy absorbed by AuNRs with different orientations. Scattered light collected by the microscope objective passes through a quarter-wave plate, polarizing beam-splitter, a beam block for specularly reflected light, and two holographic notch filters before reaching the spectrometer.[46] Data acquisition time is typically 100 s for the cw mode and 10 s for the pulsed mode. A quartz lamp source was used correct the data for variations in the wavelength dependence of the quantum efficiency of the CCD detector, the reflectivity of the spectrometer grating, and the transmission coefficients of the optical elements.

We checked for extrinsic contributions to the light emission by testing all the reagents used in synthesizing the AuNRs at concentrations of ~10^5 times of that in the final AuNRs samples and could not detect any background fluorescence with excitation by pulsed 785 nm excitation. AuNRs with different surface modification were also tested to exclude the possibility of surface-enhanced fluorescence from impurities or ligands on the surfaces of AuNR.

The characteristic time-scale of the non-linear light emission was measured using two-pulse excitation. The time delay between the two pulses is adjusted using a mechanical delay stage[46]. The two pulses have the same spectrum of 785 ± 1.5 nm and orthogonal circular polarization. The two beams are co-linear; a transient absorption measurement is used to optimize the spatial overlap of the two pulses within the sample cell[47]. We set the zero of delay time at the position of the maximum of the signal.

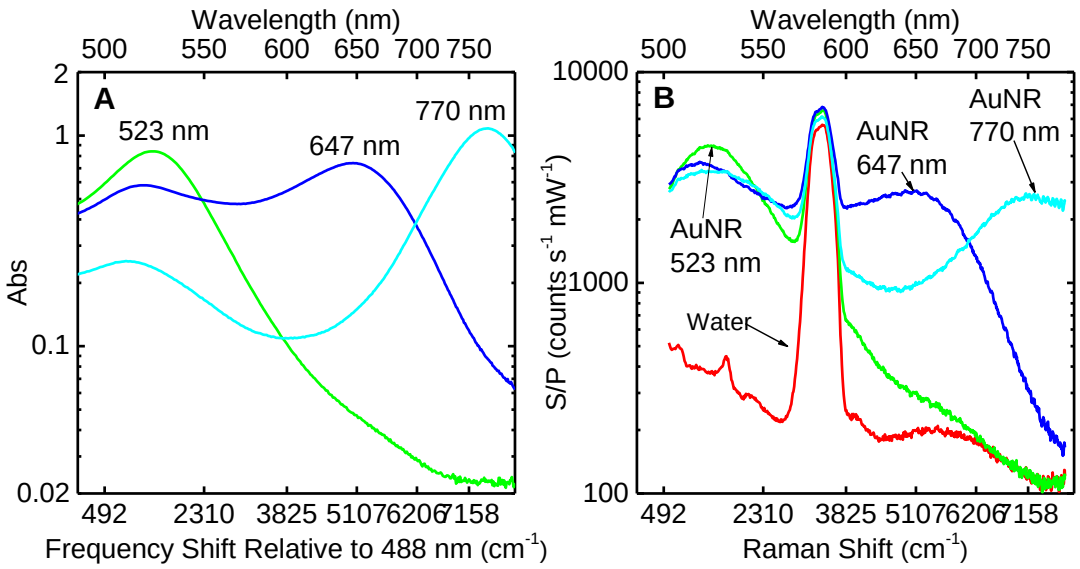

Figure 4.1 (A) Absorption spectra of AuNRs of different abstract ratios (AR): green (AR=1.2), blue (AR=2.3) and cyan (AR=3.8). The unit of the bottom axis is given as a frequency shift relative to the 488 nm laser excitation for the convenience of comparison with panel **(B)**. The top-axis provides the corresponding wavelengths. The y-axis is the absorbance (abs), i.e., the negative of the base-10 logarithm of the optical transmission. **(B)** Spectra of water and AuNRs of different absorption peaks excited by 488 nm cw laser with 1 mW power. *S* is the spectral density of the intensity of scattered light and *P* as the average excitation laser power. Thus, the y-axis is the output of the CCD camera of the spectrometer normalized by the data acquisition time and the power of the excitation laser.

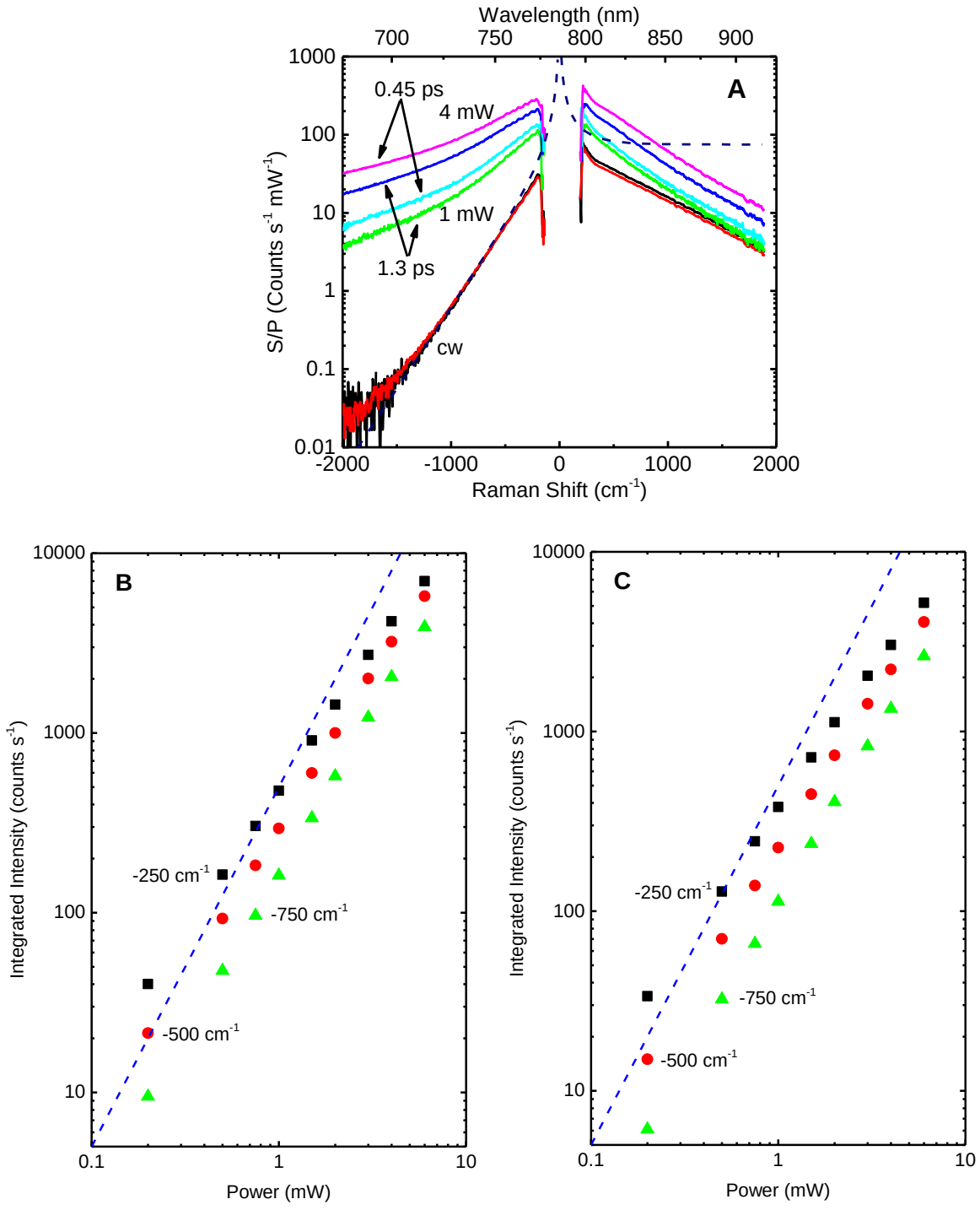

Figure 4.2 (A) Raman scattering spectra for AuNRs with the absorption peak at 787 nm excited by cw laser light at 785 nm at incident powers of 1 mW (black), 4 mW (red); by mode-locked laser pulses of 0.45 ps width with average incident powers of 1 mW (cyan) and 4 mW (magenta);

and by mode-locked laser pulses of 1.3 ps width with average incident powers of 1 mW (green) and 4 mW (blue). The y-axis is the same as in Figure 1B: *S* is the scattered intensity and *P* the average power of the excitation laser. Data for 1 mW and 4 mW using the cw laser overlap. The dashed line is the calculated intensity for a characteristic temperature of 300 K assuming constant Raman cross-section and enhancement factors at all Raman shifts; the vertical scale of the dashed line is adjusted to match the experimental anti-Stokes intensity. **(B)** Raman scattering intensity vs. average incident power for AuNRs with absorption peak at 787 nm excited by pulsed 785 nm laser pulses of 0.45 ps width integrated over a Raman shift range of -240 to -260 cm^{-1} (black squares), -490 to -510 cm^{-1} (red circles), -740 to -760 cm^{-1} (green triangles). The blue dashed line with a slope of 2 indicates a quadratic relation between the spectral intensity and average incident power. **(C)** Raman scattering intensity vs. average incident power for AuNRs with absorption peak at 787 nm excited by pulsed 785 nm laser pulses of 1.3 ps width integrated over a Raman shift range of -240 to -260 cm^{-1} (black squares), -490 to -510 cm^{-1} (red circles), -740 to -760 cm^{-1} (green triangles). The blue dashed line with a slope of 2 indicates a quadratic relation between the spectral intensity and average incident power.

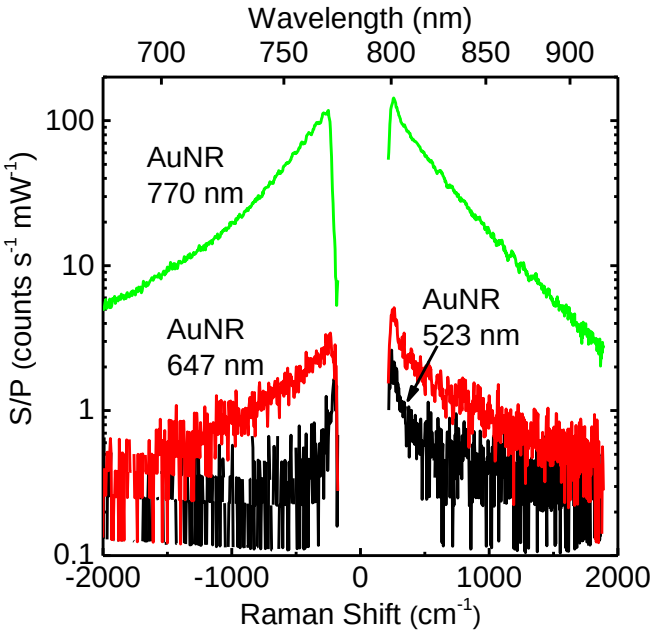

Figure 4.3 Raman scattering spectra for AuNRs with the absorption peaks at 523 nm (black), 647 nm (red) and 770 nm (green) excited by 785 nm laser pulses of 0.45 ps duration with an average incident power of 1 mW.

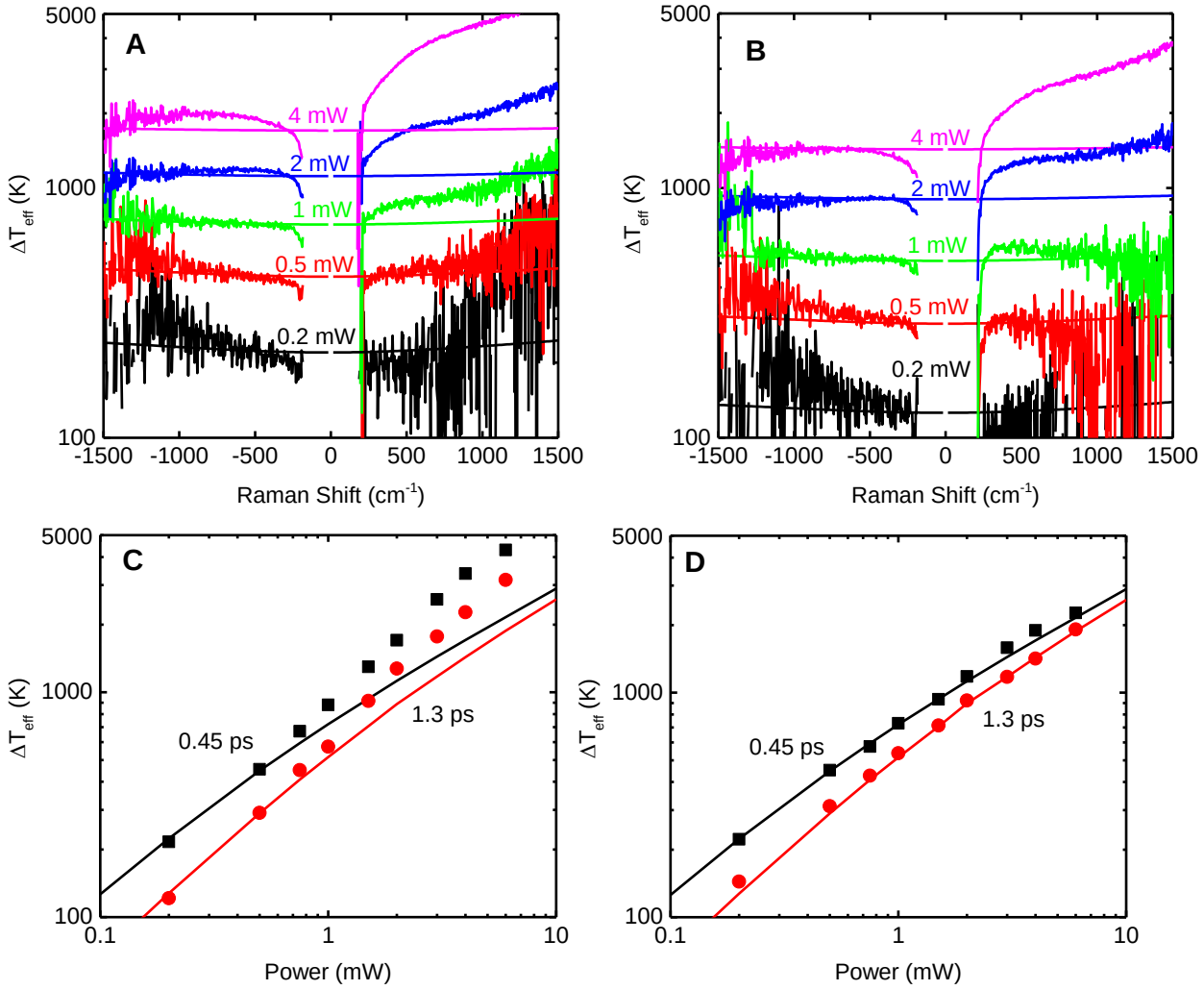

Figure 4.4 (A, B) Change in the effective temperature relative to room temperature ΔT_{eff} = T_{eff}-300 K of Raman scattering by AuNRs with absorption peak at 787 nm excited by laser pulses of **(A)** 0.45 ps and **(B)** 1.3 ps width. ΔT_{eff} calculated from the data using Eq. 4.4 are shown as lines that show some noise. ΔT_{eff} calculated using Eq. 4.4 and 4.8 with the optical cross-section σ_{abs} as a fitting parameter are shown as smooth lines. The best fit to the data for -1500 cm^{-1}<Δω<1500 cm^{-1} gives σ_{abs}=2700 nm^2. **(C, D)** ΔT_{eff} of the measurement at a Raman shift of **(C)** -500 cm^{-1} and **(D)** 500 cm^{-1} with laser pulse duration of 0.45 ps (black squares) and 1.3 ps (red circles). The solid lines show the predicted values of ΔT_{eff} as a function of laser power

using σ_{abs}=2700 nm^2.

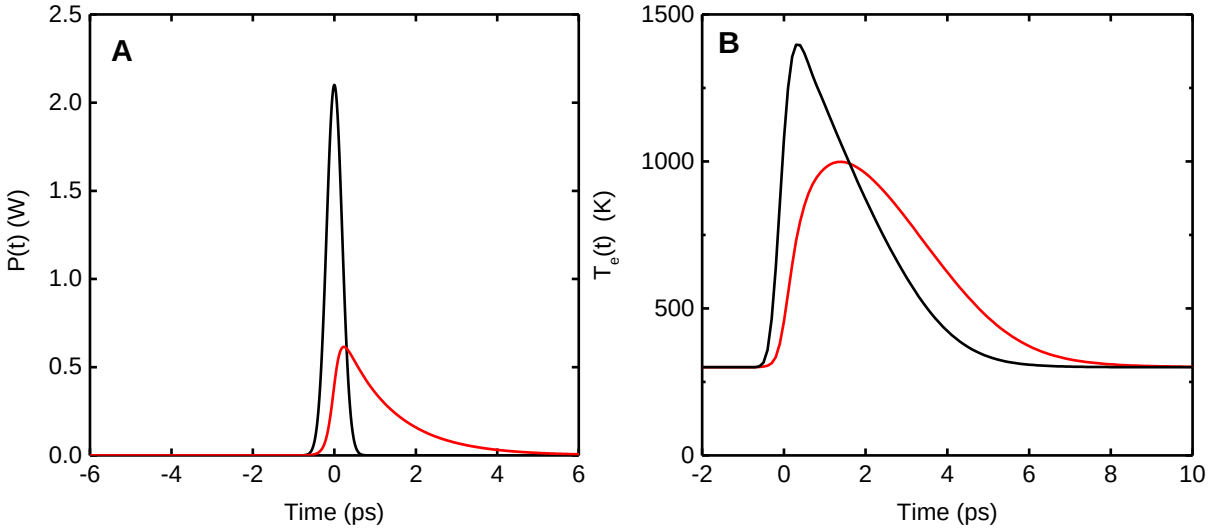

Figure 4.5 (A) Laser pulse shapes calculated by Eqs. 4.6 and 4.7 for Gaussian pulse with FWHM=0.45 ps (black) and the pulse with FWHM=1.3 ps (red) after traveling through the etalon. The average laser power is 1 mW in both cases. **(B)** Evolution of the AuNR electron temperature during one laser pulse excitation calculated by Eqs. 4.5, 4.6 and 4.7. Pulse with 0.45 ps width (black); pulse with 1.3 ps width (red).

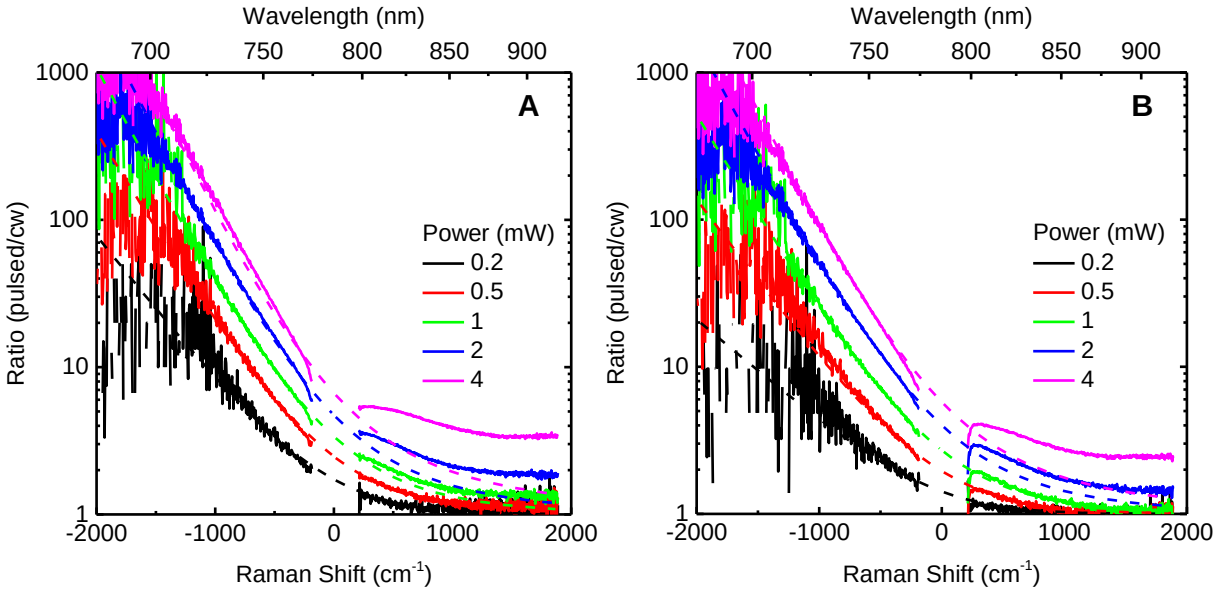

Figure 4.6 Ratio of the normalized emission spectra (S/P) of aspect-ratio 3.8 AuNRs excited by 785 nm laser of different average laser powers at pulsed mode with **(A)** 0.45 ps pulse width or **(B)** 1.3 ps pulse width vs. at cw mode. (solid curves: data; dashed lines: calculated from Eqs. 4.5 and 4.8 with σ_{abs}=2700 nm^2)

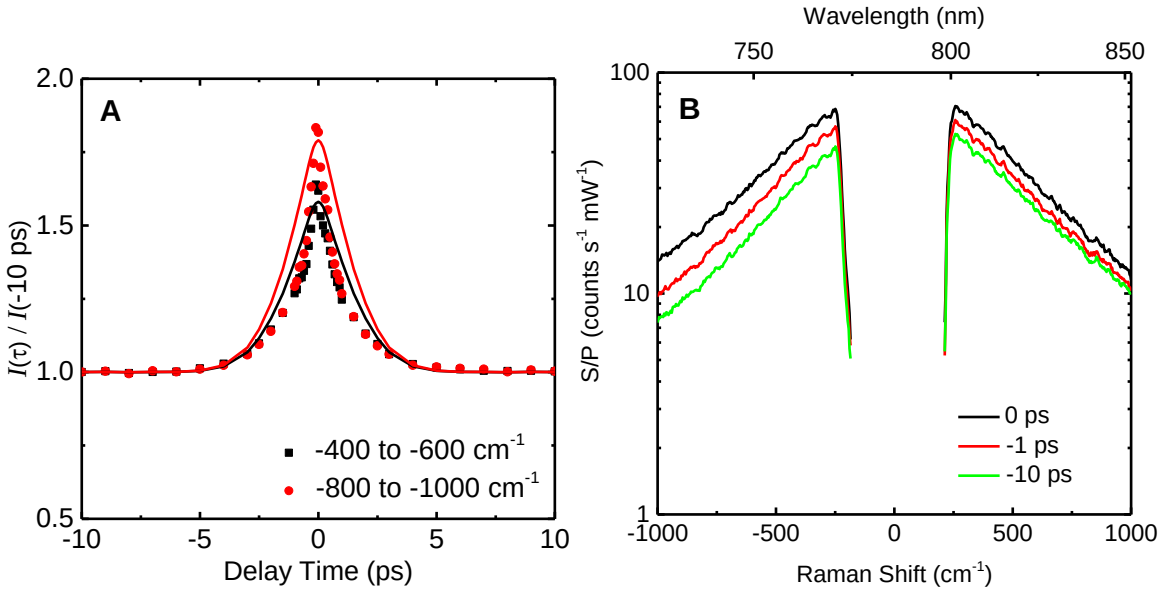

Figure 4.7 (A) Ratios of integrated intensity at various delay times *I(τ)* vs. -10 ps *I*(-10 ps) with data at -400 to -600 cm^{-1} (black square), -800 to -1000 cm^{-1}(red circle) and the model calculation at -500 cm^{-1} (black line) and -900 cm^{-1} (red line). **(B)** Emission spectra of aspect ratio 3.8 AuNRs excited by two 0.45 ps laser pulses at different delay times. These spectra are not corrected for variations in the efficiency of the spectrometer. The short period oscillations in the data as a function of frequency shift are caused by variations in the quantum efficiency of the CCD sensor.

4.5 REFERENCES

1. Murphy, C. J.; Sau, T. K.; Gole, A. M.; Orendorff, C. J.; Gao, J.; Gou, L.; Hunyadi, S. E.; Li, T. Anisotropic Metal Nanoparticles: Synthesis, Assembly, and Optical Applications. *J. Phys. Chem. B* **2005**, *109*, 13857–13870.
2. Aroca, R. F.; Alvarez-Puebla, R. A.; Pieczonka, N.; Sanchez-Cortez, S.; Garcia-Ramos, J. V. Surface-Enhanced Raman Scattering on Colloidal Nanostructures. *Adv. Colloid Interface Sci.* **2005**, *116*, 45–61.
3. Brown, R. J. C.; Milton, M. J. T. Nanostructures and Nanostructured Substrates for Surface-Enhanced Raman Scattering (SERS). *J. Raman Spectrosc.* **2008**, *39*, 1313–1326.
4. Jiang, Y.; Horimoto, N. N.; Imura, K.; Okamoto, H.; Matsui, K.; Shigemoto, R. Bioimaging with Two-Photon-Induced Luminescence from Triangular Nanoplates and Nanoparticle Aggregates of Gold. *Adv. Mater.* **2009**, *21*, 2309–+.
5. Wang, H.; Huff, T. B.; Zweifel, D. A.; He, W.; Low, P. S.; Wei, A.; Cheng, J.-X. In Vitro and in Vivo Two-Photon Luminescence Imaging of Single Gold Nanorods. *Proc. Natl. Acad. Sci. U. S. A.* **2005**, *102*, 15752–15756.
6. Furtak, T. E.; Reyes, J. A Critical Analysis of Theoretical Models for the Giant Raman Effect from Adsorbed Molecules. *Surf. Sci.* **1980**, *93*, 351–382.
7. Mooradian, A. Photoluminescence of Metals. *Phys. Rev. Lett.* **1969**, *22*, 185–187.
8. Heritage, J. P.; Bergman, J. G.; Pinczuk, A.; Worlock, J. M. Surface Picosecond Raman Gain Spectroscopy of a Cyanide Monolayer on Silver. *Chem. Phys. Lett.* **1979**, *67*, 229–232.
9. Otto, A.; Akemann, W.; Pucci, A. Normal Bands in Surface-Enhanced Raman Scattering

(SERS) and Their Relation to the Electron-Hole Pair Excitation Background in SERS. *Isr. J. Chem.* **2006**, *46*, 307–315.

10. Bosnick, K. A.; Jiang; Brus, L. E. Fluctuations and Local Symmetry in Single-Molecule Rhodamine 6G Raman Scattering on Silver Nanocrystal Aggregates†. *J. Phys. Chem. B* **2002**, *106*, 8096–8099.
11. Mooradian, A. Photoluminescence of Metals. *Phys. Rev. Lett.* **1969**, *22*, 185–187.
12. Shahbazyan, T. V. Theory of Plasmon-Enhanced Metal Photoluminescence. *Nano Lett.* **2013**, *13*, 194–198.
13. Varnavski, O. P.; Mohamed, M. B.; El-Sayed, M. A.; Goodson, T. Relative Enhancement of Ultrafast Emission in Gold Nanorods. *J. Phys. Chem. B* **2003**, *107*, 3101–3104.
14. Imura, K.; Nagahara, T.; Okamoto, H. Plasmon Mode Imaging of Single Gold Nanorods. *J. Am. Chem. Soc.* **2004**, *126*, 12730–12731.
15. Varnavski, O. P.; Goodson, T.; Mohamed, M. B.; El-Sayed, M. A. Femtosecond Excitation Dynamics in Gold Nanospheres and Nanorods. *Phys. Rev. B* **2005**, *72*, 235405.
16. Goldys, E. M.; Sobhan, M. A. Fluorescence of Colloidal Gold Nanoparticles Is Controlled by the Surface Adsorbate. *Adv. Funct. Mater.* **2012**, *22*, 1906–1913.
17. Jiang, X.-F.; Pan, Y.; Jiang, C.; Zhao, T.; Yuan, P.; Venkatesan, T.; Xu, Q.-H. Excitation Nature of Two-Photon Photoluminescence of Gold Nanorods and Coupled Gold Nanoparticles Studied by Two-Pulse Emission Modulation Spectroscopy. *J. Phys. Chem. Lett.* **2013**, *4*, 1634–1638.
18. Beversluis, M. R.; Bouhelier, A.; Novotny, L. Continuum Generation from Single Gold

Nanostructures through near-Field Mediated Intraband Transitions. *Phys. Rev. B* **2003**, *68*, 115433.

19. Bouhelier, A.; Bachelot, R.; Lerondel, G.; Kostcheev, S.; Royer, P.; Wiederrecht, G. P. Surface Plasmon Characteristics of Tunable Photoluminescence in Single Gold Nanorods. *Phys. Rev. Lett.* **2005**, *95*, 267405.
20. Chang, W.-S.; Willingham, B.; Slaughter, L. S.; Dominguez-Medina, S.; Swanglap, P.; Link, S. Radiative and Nonradiative Properties of Single Plasmonic Nanoparticles and Their Assemblies. *Acc. Chem. Res.* **2012**, *45*, 1936–1945.
21. Fang, Y.; Chang, W.-S.; Willingham, B.; Swanglap, P.; Dominguez-Medina, S.; Link, S. Plasmon Emission Quantum Yield of Single Gold Nanorods as a Function of Aspect Ratio. *ACS Nano* **2012**, *6*, 7177–7184.
22. Yorulmaz, M.; Khatua, S.; Zijlstra, P.; Gaiduk, A.; Orrit, M. Luminescence Quantum Yield of Single Gold Nanorods. *Nano Lett.* **2012**, *12*, 4385–4391.
23. Klein, M. V. Equivalence of Resonance Raman Scattering in Solids with Absorption Followed by Luminescence. *Phys. Rev. B* **1973**, *8*, 919–921.
24. Solin, J. R.; Merkelo, H. Resonant Scattering or Absorption Followed by Emission. *Phys. Rev. B* **1975**, *12*, 624–629.
25. Solin, J. R.; Merkelo, H. Reply to "Comment on `Resonant Scattering or Absorption Followed by Emission' ."*Phys. Rev. B* **1976**, *14*, 1775–1776.
26. Shen, Y. R. Distinction between Resonance Raman Scattering and Hot Luminescence. *Phys. Rev. B* **1974**, *9*, 622–626.

27. Shen, Y. R. Comment on “Resonant Scattering or Absorption Followed by Emission.”*Phys. Rev. B* **1976**, *14*, 1772–1774.

28. Hochstrasser, R. M.; Novak, F. A. The Effect of Fluctuations on Emission Spectra: Practical Distinctions between Raman and Fluorescence Spectra. *Chem. Phys. Lett.* **1977**, *48*, 1–6.

29. Courtens, E.; Szöke, A. Time and Spectral Resolution in Resonance Scattering and Resonance Fluorescence. *Phys. Rev. A* **1977**, *15*, 1588–1603.

30. Kono, H.; Nomura, Y.; Fujimura, Y. A Theoretical Study of Origins of Resonance Raman and Resonance Fluorescence Using a Split-Up of the Emission Correlation Function. In *Advances in Chemical Physics*; Prigogine, I.; Rice, S. A., Eds.; John Wiley & Sons, Inc., 2007; pp. 403–462.

31. Ponosov, Y. S.; Streltsov, S. V. Measurements of Raman Scattering by Electrons in Metals: The Effects of Electron-Phonon Coupling. *Phys. Rev. B* **2012**, *86*, 045138.

32. Farhat, H.; Berciaud, S.; Kalbac, M.; Saito, R.; Heinz, T. F.; Dresselhaus, M. S.; Kong, J. Observation of Electronic Raman Scattering in Metallic Carbon Nanotubes. *Phys. Rev. Lett.* **2011**, *107*.

33. Kawabata, A.; Kubo, R. Electronic Properties of Fine Metallic Particles. II. Plasma Resonance Absorption. *J. Phys. Soc. Jpn.* **1966**, *21*, 1765.

34. Jain, P. K.; Lee, K. S.; El-Sayed, I. H.; El-Sayed, M. A. Calculated Absorption and Scattering Properties of Gold Nanoparticles of Different Size, Shape, and Composition: Applications in Biological Imaging and Biomedicine. *J. Phys. Chem. B* **2006**, *110*, 7238–7248.

35. Klein, M. V. Electronic Raman Scattering. In *Theory of Light Scattering in Condensed*

Matter; Bendow, B.; Birman, J. L.; Agranovich, V. M., Eds.; Springer US: Boston, MA, 1976; pp. 461–473.

36. Kneipp, J.; Kneipp, H.; Kneipp, K. SERS—a Single-Molecule and Nanoscale Tool for Bioanalytics. *Chem. Soc. Rev.* **2008**, *37*, 1052–1060.

37. Ward, D. R.; Corley, D. A.; Tour, J. M.; Natelson, D. Vibrational and Electronic Heating in Nanoscale Junctions. *Nat. Nanotechnol.* **2011**, *6*, 33–38.

38. Hartland, G. V. Coherent Excitation of Vibrational Modes in Metallic Nanoparticles. *Annu. Rev. Phys. Chem.* **2006**, *57*, 403–430.

39. Ekici, O.; Harrison, R. K.; Durr, N. J.; Eversole, D. S.; Lee, M.; Ben-Yakar, A. Thermal Analysis of Gold Nanorods Heated with Femtosecond Laser Pulses. *J. Phys. Appl. Phys.* **2008**, *41*, 185501.

40. Martin, R. M.; Varma, C. M. Cascade Theory of Inelastic Scattering of Light. *Phys. Rev. Lett.* **1971**, *26*, 1241–1244.

41. Hartland, G. V. Optical Studies of Dynamics in Noble Metal Nanostructures. *Chem. Rev.* **2011**, *111*, 3858–3887.

42. Groeneveld, R. H. M.; Sprik, R.; Lagendijk, A. Femtosecond Spectroscopy of Electron-Electron and Electron-Phonon Energy Relaxation in Ag and Au. *Phys. Rev. B* **1995**, *51*, 11433–11445.

43. Sau, T. K.; Murphy, C. J. Seeded High Yield Synthesis of Short Au Nanorods in Aqueous Solution. *Langmuir* **2004**, *20*, 6414–6420.

44. Gole, A.; Murphy, C. J. Polyelectrolyte-Coated Gold Nanorods: Synthesis, Characterization

and Immobilization. *Chem. Mater.* **2005**, *17*, 1325–1330.

45. Zou, R.; Zhang, Q.; Zhao, Q.; Peng, F.; Wang, H.; Yu, H.; Yang, J. Thermal Stability of Gold Nanorods in an Aqueous Solution. *Colloids Surf. Physicochem. Eng. Asp.* **2010**, *372*, 177–181.

46. Kang, K.; Koh, Y. K.; Chiritescu, C.; Zheng, X.; Cahill, D. G. Two-Tint Pump-Probe Measurements Using a Femtosecond Laser Oscillator and Sharp-Edged Optical Filters. *Rev. Sci. Instrum.* **2008**, *79*.

47. Huang, J.; Park, J.; Wang, W.; Murphy, C. J.; Cahill, D. G. Ultrafast Thermal Analysis of Surface Functionalized Gold Nanorods in Aqueous Solution. *ACS Nano* **2013**, *7*, 589–597.

CHAPTER 5

PHOTOTHERMAL MOLECULAR RELEASE TRIGGERED BY ULTRAFAST LASER PULSES AS MONITORED BY SURFACE -ENHANCED RAMAN SCATTERING

5.1 INTRODUCTION

The photothermal molecular release system based on polymer wrapping layers on the GNR surface with continuous-wave laser irradiation has been introduced in Chapter 2 of this thesis. It has been noticed that the molecular release rate with cw laser excitation is mild and slow with only 6% release after 1 hour of laser irradiation.[1] In order to obtain a higher molecular release rate and percentage in the drug delivery system, new methods need to be applied to improve the efficiency of the release. As it has been discussed in Section 1.1, since pulsed laser irradiation can induce transient large localized temperature rise around GNR,[2,3] it is expected to accelerate the release rate with such high temperature excursion with laser pulses. Light-triggered drug release with pulsed lasers has also been reported in previous work,[4,5] in which high power laser pulses were used to irradiate at the SPR peak position of gold nanoparticles to break Au-S bonds or even to melt the nanoparticles to release bound molecules.[6–10] However, whether or not the released molecules still remain active for therapy after high power pulsed laser irradiation should be considered in the scenario.

Surface-enhanced Raman scattering (SERS) was first discovered on molecules absorbed on rough metal surface several decades ago.[11] With the development of controlled fabrication and synthesis of metallic nanostructures as substrates, SERS spectroscopy has become a popular

analytical tool in sensing of chemical and biological molecules due to its high sensitivity and selectivity.[12,13] Two mechanisms proposed for SERS, the electromagnetic and chemical mechanisms were introduced in Section 1.6. Compared to the electromagnetic enhancement factor over 10^5 or 10^6 in solution, the chemical enhancement factor is only 10 to 10^2.[14] In the experimental design of this thesis, Raman reporter molecules were electrostatically bound on the surface coatings including the CTAB bilayer and several numbers of polyelectrolyte layers on the GNR surface without direct interaction with the metal surface, the chemical enhancement can be generally ignored. Thus, we focus the discussion on the electromagnetic enhancement. In the case of spherical nanoparticles as SERS substrate, the surface-enhanced Raman enhancement factor (EF) can be described by the equations[12] below:

$$EF = \frac{|E_{out}|^2 |E'_{out}|^2}{|E_0|^4} = 4|g|^2 |g'|^2 \quad (5.1)$$

where E_0 is magnitude of electromagnetic field of the incident light; E_{out} is the magnitude of electromagnetic field outside the particle after the field enhancing, which is approximated as $|E_{out}|^2=2|E_0|^2|g|^2$; g is the enhancement coefficient; the prime symbol indicates the field evaluated at the scattered light.

The enhancement factor can also be measured experimentally in an easier way, in which EF of the molecule Raman signal excited by a single wavelength incident light can be described by the equation below:

$$EF = \frac{[I_{SERS} / N_{surf}]}{[I_{NRS} / N_{vol}]} \quad (5.2)$$

where I_{SERS} is the surface-enhanced Raman intensity; I_{NRS} is the normal Raman intensity; N_{surf} is the number of molecules bound on the surface of substrates in the excitation spot size; and N_{vol} is the number of molecules in the excitation volume without enhancing substrates.

The electromagnetic field decays with the distance from the spherical particle surface with a factor of r^{-3} and the SERS signal is proportional to $|E|^4$. Considering the overall surface area is proportional to r^2, thus the total enhancement factor of a shell of adsorbed Raman reporters should have a r^{-10} distance-dependence as described by the following equation[12]:

$$I_{SERS} = \left(\frac{a+r}{a} \right)^{-10} \tag{5.3}$$

where a is the average radius of the field-enhancing particle; and r is the distance of the Raman reporter molecule from the substrate surface. Distance-dependent surface-enhanced Raman scattering was investigated in research works,[15–21] where the experimental results vary with different substrates and methods, which do not simply obey this r^{-10} distance-dependence rule.

In this chapter, surface-enhanced Raman scattering signal of the Raman reporters were detected to investigate the accelerated molecular release by localized heating with ultrafast laser pulses. This protocol allows *in situ* signal monitoring of the molecular release to get eliminate the extra step for the separation of bound and released reporters molecules in Chapter 2. To test the feasibility of this method, the distance-dependent SERS from GNR surfaces was first investigated, and the other factors such as thermal degradation and photo bleaching of Raman reporters by laser pulses were also evaluated in the process.

5.2 RESULTS AND DISCUSSION

Distance-dependent SERS on Gold Nanoparticle Surfaces

SERS phenomenon can be observed even if the Raman reporters are not directly attached to the substrate. The idea of using SERS to monitor drug release is based on concept that when the molecules are close to GNR surface in this case (~ 4 nm away from GNR surface, with the EF~10^5 or 10^6), large SERS signals can be observed; while molecules are released from the GNR surface the SERS signal decreased exponentially with the distance and barely any SERS signal can be observed. However, the control experiments of the distance-dependent SERS EF should still be tested, since it varies with substrate size, shape and experiment environments. Some research work on the distance-dependent SERS EF are summarized in Table 5.1. In order to investigate the average SERS enhancement factor change with distance away from the GNR surface, the positively charged Raman reporter molecules Nile Blue A (NBA) were immobilized on GNR surface with different numbers of PEL spacer layers to produce layered assemblies GNR+PAA+$(PAH+PAA)_n$+NBA+PAH (n=0,1,2,3). The complexation of positively-charged NBA and negatively-charged PAA was immediately found after the mix of NBA and PAA, since the color of NBA solution changed from blue to purple and an obvious change of absorption and Raman spectra of NBA solution was observed, while no obvious changes were found when NBA was mixed with negatively-charged PAH. NBA molecules were electrostatically immobilized on the PAA coatings on GNR surface and SERS signals from NBA were detected.

The average number of NBA molecules on each GNR surface was quantified. During

sample preparation, NBA supernatants were collected after the centrifugation of the NBA-incubated sample. A calibration curve based on optical absorption spectra of NBA standards in 2 mg/mL PAH with the concentration from 0.1 μM to 1 mM was created, and the concentration of NBA in supernatant $[NBA]_{supernatant}$ was calculated based on the calibration curve. Standard aqueous solution of NBA in 2 mg/mL PAH was used here to match the real composition of the NBA supernatant during the sample preparation. The absorption spectrum of NBA has a maximum at 637 nm both in water and in 2 mg/mL PAH, and no obvious change of the absorption spectra can be observed between NBA in water and NBA in PAH solution, which indicated no strong interaction existing between NBA and PAH. Then the concentration of the bound NAB ($[NBA]_{bound}$) was calculated with the equation: $[NBA]_{bound} = [NBA]_{incubation}-[NBA]_{supernatant}$, where $[NBA]_{incubation}$ is the original concentration of NBA for incubation. It was found that the average $[NBA]_{bound}$ in the final sample was always below 4 μM even if $[NBA]_{incubation}$ was as large as 100 μM. $[NBA]_{incubation}$ should be carefully chosen, since if $[NBA]_{incubation}$ is much larger than $[NBA]_{bound}$, the calculated $[NBA]_{bound}$ should also have a large uncertainty; if $[NBA]_{incubation}$ is too small, the detected signal to noise ratio can be large. Thus $[NBA]_{incubation}$ of either 2 μM or 10 μM was chosen after multiple rounds of testing. The SERS spectra of samples with different PEL spacer layers normalized by acquisition time and laser power are shown in Fig. 5.1. The Raman peak from the NBA ring bending vibrational mode[22,23] at 590 cm^{-1} was used as an representative Raman signal, and the peak signal was found to drop quickly with the increasing number of PEL spacer layers. Finally, the average number of NBA on each GNR was calculated by dividing $[NBA]_{bound}$ with [GNR], where [GNR] was 2 nM in these

experiments, and plotted in Fig. 5.2a. It was found that 10 μM incubation concentration gave larger numbers of bound NBA on each GNR than 2 μM incubation concentration, which indicated a binding equilibrium between NBA and GNR+PAA during the sample preparation. With the increasing number of spacing PEL, the surface of GNR+PEL should also increase to provide more binding sites for NBA theoretically. However, it was found that the number of NBA per GNR dropped greatly from 1 PEL spacer layer to 3 spacer layers and then increased again when it reaches 5 and 7 PEL spacer layers. This phenomenon was also found in previous studies from our research group,[24,25] but no clear explanation has be provided so far.

The background of the Raman spectra were subtracted using the NuSpec software in the DeltaNu Advantage 785 Raman system. The integrated areas of the 590 cm^{-1} Raman peak of different samples are plotted in Fig. 5.2b, and it was found that the intensity dropped quickly with increasing number of PEL spacer layers. The SERS enhancement factors can be calculated based on Eq. 5.2, in which I_{SERS} is the integrated SERS peak area at 590 $cm^{-1}$of a sample (as plotted in Fig. 5.2b); N_{sur} is $[NBA]_{bound}$; I_{NRS} is the integrated normal Raman peak area at 590 cm^{-1} of 200 μM NBA in 10 mg/mL PAA (to match the environment of NBA on GNR surface); N_{vol} is 200 μM. Since the Raman detection was performed on the same instrument with the same laser parameters, the number of NBA molecules in the laser beam can be represented by the concentration of NBA molecules. The absorbance of the GNR+NBA and the NBA+PAA was kept the same to make sure the two samples have the same incident power through the laser optical path in the cuvette. The SERS enhancement factors were plotted in Fig. 5.2c and the EF

dropped exponentially with the number of PEL layers. The distance was around 4 nm with 1 PEL spacer layer, 6 nm with 3 PEL spacer layer, 8 nm with 5 PEL spacer layers and ~10 nm with 7 PEL spacer layers from the previous DLS study in Chapter 3.[26] Thus the SERS EF was found to drop approximately exponentially with the distance from GNR surface. The SERS enhancement factors of samples with the same spacer layers prepared from either 2 μM or 10 μM NBA incubation concentrations should have the same value theoretically, however, the numbers still had some deviations shown in Fig. 5.2c, which should be further tested quantitatively in more experiments. But we can conclude from these tests that if the NBA molecule is released from the GNR+PAA+NBA+PAH system and diffuses to a position of 10 nm away from GNR surface, the SERS signal can drop more than 95% and using SERS to monitor the molecular release in this case is reasonable. It should be noticed that the electric field intensity at a certain distance around the anisotropic gold nanorod is not constant, and the electric field around the tips of gold nanorod are much higher than that around the sides. Thus the enhancement factors calculated here are only average EFs around the GNRs. The results of distance-dependent SERS EF dropping quickly with increasing spacer thickness however still observable over 10 nm away from substrate are consistent with the findings of other works.[15-21]

The SERS enhancement factors were also tested for gold nanoparticles (GNPs) of different aspect ratios. Samples of GNP+PAA+NBA+PAH were prepared for GNPs with absorption peak at 530 nm, 710 nm and 800 nm respectively. SERS enhancement factors were calculated in the same method mentioned above and summarized in Table 5.2. It was shown that GNRs of AR=2.8

have the larger SERS EF than AR 1.1 and 4.0 GNRs, the results are also in agreement with the previous studies from our research group.[27] These results were explained as a combined effect of SERS enhancement and extinction of the excitation light in the laser path.[27]

Table 5.1 Distance-dependent surface-enhanced Raman scattering enhancement studies from previous research works.

Substrate	Spacer	Reporter	Findings
Ag toroid array	ssDNA	AAA tract	Enhancement over 30 nm from the substrate.[15]
roughened Ag	alkanethiols	benzene	EF~2.1×10^3, decreasing with distance. Enhancement studies 0.6-2.7 nm from substrate. [17]
Oval gold nanoparticles	dsDNA	Rh6G	EF decreasing with distance. Enhancement over 20 nm from GNP.[18]
In/Ag island films	arachidic acid	Rh6G	EF~10^2-10^3, decreasing with distance. Enhancement over 16 nm from substrate.[19]
Ag nanoparticles	SiO_2 layer	adenosine	EF~10^6, decreasing slightly within 30 nm and abruptly after 30 nm from Ag particle.[20]
Ag nanorod arrays	oligos	adenine tracts	EF decreasing with distance. Effective sensing distance is within 5 nm from Ag nanorod surface.[21]

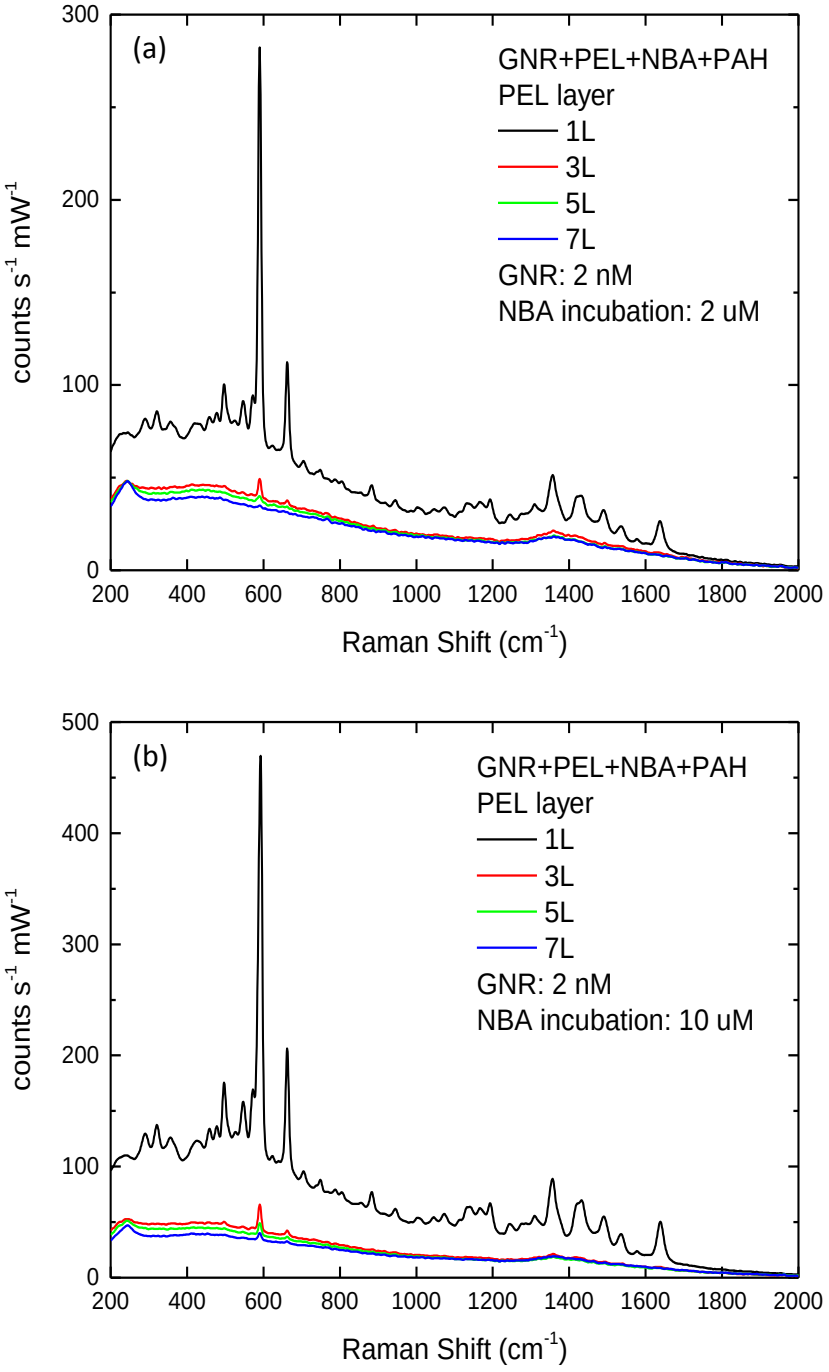

Figure 5.1 Surface-enhanced Raman spectra of nile blue A on the surface of GNRs of aspect ratio 4 with different numbers of polyelectrolyte spacer layers and nile blue A original incubation concentrations (a) 2 μM and (b) 10 μM.

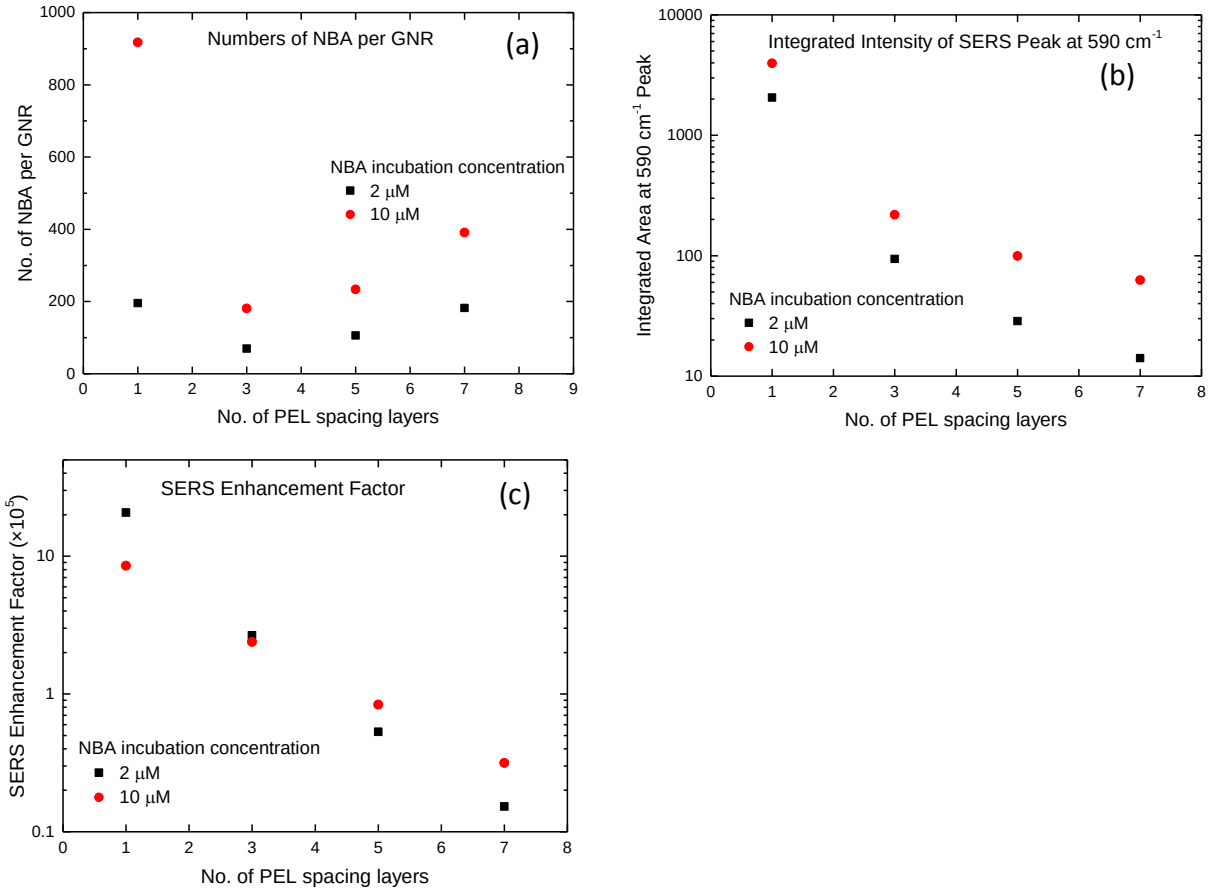

Figure 5.2 Distance-dependent SERS EF of NBA on GNR surface of samples with different original NBA incubation concentrations: (a) the number of NBA on each GNR, (b) the integrated area of the 590 cm^{-1} Raman peak, (c) the SERS enhancement factors.

Table 5.2 SERS enhancement factors of gold nanoparticles with different aspect ratios.

GNP peak λ_{abs} (nm)	530	710	800
[GNP] (nM)	2	2	2
GNR AR	1.1	2.8	4.0
$[NBA]_{incubation}$ (μM)	10	10	10
$[NBA]_{bound}$ (μM)	1.46	0.95	2.96
# of NBA/GNP	732	475	1480
Enhancement factors	1.47×10^5	2.16×10^6	1.97×10^5

Note: Raman reporter molecules were immobilized in GNP+PAA+NBA+PAH samples, and the distance from the reporters to GNP surface is estimated around 4 nm.[26]

Molecular Release vs. Photon Damaging by Ultrafast Laser Pulses

Molecular release by laser pulses was tested with the sample structure of GNR+PAA+NBA+ PAH, in which the Raman reporters are close to GNR surface to give large SERS signal and the temperature change is also larger when it is closer to GNR surface. GNRs with absorption peaks close to 785 nm were chosen to match the laser wavelength of the instrument to generate the most. Pulsed laser irradiation with controlled parameters was attended for the initiate molecular release. Raman spectra were acquired with 1 mW cw excitation to exclude the possibility of continuous molecular release during the 30 s spectra acquisition period. SERS intensities before and after laser pulse irradiation were compared.

SERS signal before and after laser pulse irradiation was evaluated by several parameters: average laser power, laser pulse duration, irradiation time, numbers of PEL wrapping layer and GNR aspect ratio. First of all, cw laser irradiation for 3 min at the power of 1 mW was proved not to induce SERS signal change. (1) Fig. 5.3a shows the SERS signal ratio after and before 30 s laser pulse irradiation decreased with the increasing average power. There was no obvious molecular release when the average power of laser pulses was below 0.05 mW. As the power increased up to 5 mW, more than 80% of SERS signal of NBA was lost only after 30 s irradiation. During the measurement, it was also found that the SERS signal was not stable after irradiation by laser pulse power above 2mW, the SERS signal starts recover after only 20 s, which might be attributed by the PEL+NBA expansion and retraction in the PVA media. (2) Fig. 5.3b shows the data with laser pulse duration of 1.3 ps instead of 0.45 ps as used in all the other

experiments of the section. This part of the experiment was designed to test the possibility of photo bleaching of NBA. Expansion of the laser pulse reduces the incident light intensity, which was supposed to reduce the degree of photo bleaching. However, no obvious difference of the SERS ratio could be found by changing the laser pulse duration. This indicates that either no photo-bleaching or thermal degradation happened or expansion of the pulse duration to 1.3 ps was not effective enough to induce any change. (3) Fig. 5.3c shows the SERS ratio with different irradiation time by either 0.2 mW or 1 mW laser pulses. It was found the decreased gradually with increasing irradiation time. (4) The SERS ratios were compared between samples with one or two polyelectrolyte wrapping layers at different pulsed laser powers and were plotted in Fig. 5.3d. The trends were generally the same with slight differences. An additional wrapping layer did not affect the signal change as obviously as that of the work in Chapter 2. Some evidence could be extracted from these plots to show there was molecular release upon laser irradiation the rate depended on the laser power, irradiation time and wrapping layers. However, the hypothesis could only be solid if there was no photo bleaching or thermal damage to the NBA in the experiments.

In fact, surface-enhanced femtosecond stimulated Raman spectroscopy has been reported and sample degradation was observed on the minute time scale,[3,28] in which the SPR of the plasmonic nanoparticle was playing a significant role. In order to test the sample degradation in our experiments and examine the importance of plasmonic enhancement of the EM field as well as the transient temperature change. Gold nanospheres were used there for as a control.

GNS+PAA+NBA+PAH was prepared and the SERS ratio before and after laser illumination was measured with the same procedures. Fig. 5.4a shows that though both the temperature rise and plasmon enhancement are larger in the GNR sample, while the SERS signal decreased to the same extent for both GNR and GNS samples. (GNR+PAA+NBA+PAH sample had an absorption of 30% at 785 nm during the measurement while GNS+PAA+NBA+PAH sample had an absorption of 15% at 785 nm during the measurement.) In this case pure photothermal molecular release cannot explain the SERS signal decrease after laser pulses irradiation. Very likely, both photothermal release and photon degradation can attribute to the final results. Another set of control experiments of GNR+PAA+NBA+PAH immobilized on quartz substrate was examined by laser pulse irradiation, so that the possibility of molecular release can be excluded. Continuous-wave laser irradiation at the power of 1 mW and 5 mW did not affect the SERS signal. Pulsed laser irradiation at the power below 0.5 mW did not affect the SERS signal either and signal decrease took place above 0.5 mW laser power. In this way, photon degradation of NBA SERS was verified, both the Raman molecules degradation and the plasmon bleaching can result in the signal drop.

In conclusion, SERS is sensitive for molecular detection. In order to evaluate the method of photothermal molecular release with femtosecond laser pulses monitoring with SERS, distance-dependent SERS EF was examined around GNRs. SERS EF was found to decrease exponentially with the distance from the GNR surface. SERS signal decreased after laser pulse irradiation and the decreasing rate depended on laser power, irradiation time and wrapping

layers. Control experiments involving GNS+NBA in PVA gel and GNR+NBA on quartz substrate revealed the sample degradation during femtosecond laser pulse irradiation. Both molecular release and sample degradation can contribute to the SERS signal decrease and laser power should be carefully chosen to avoid sample damaging while still ensure the molecular release rate.

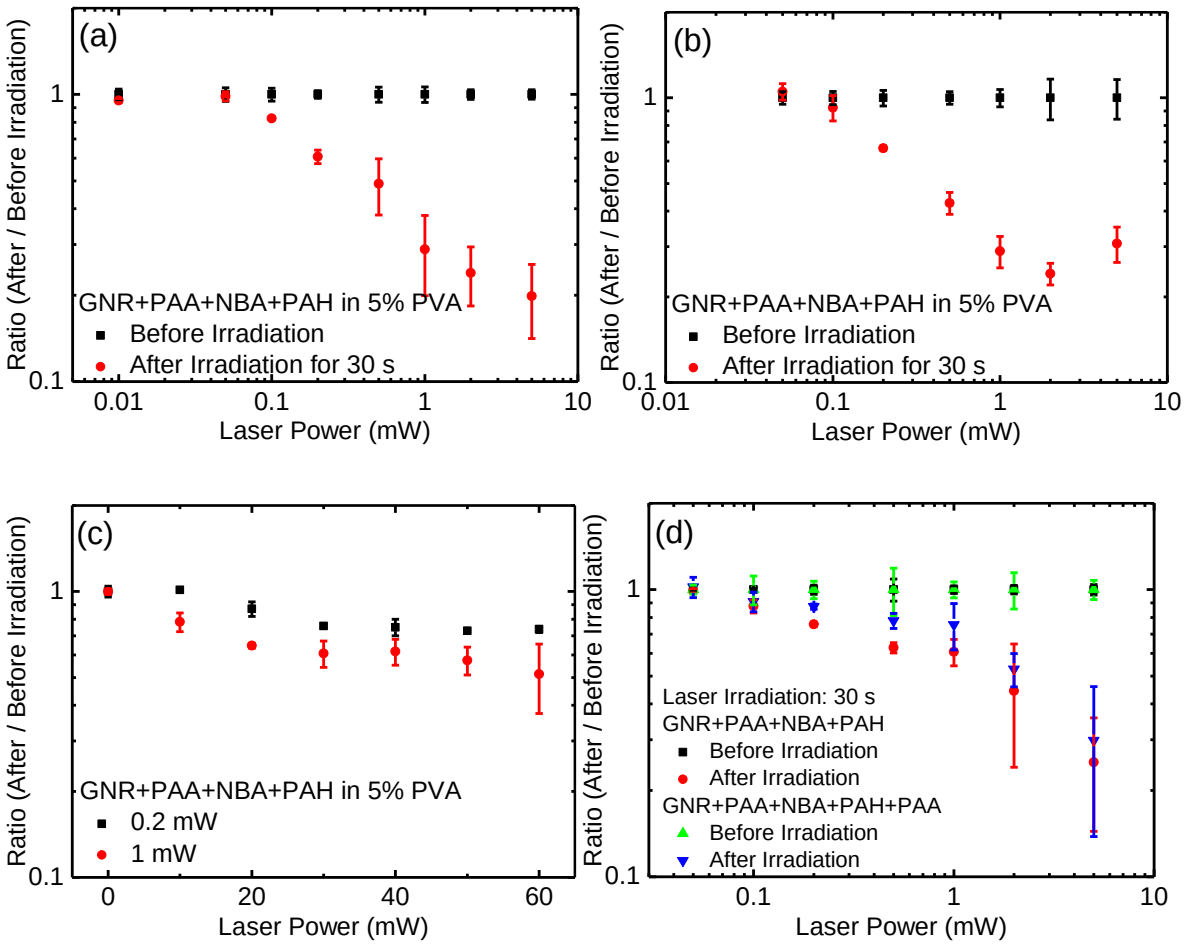

Figure 5.3 NBA SERS ratios of signal after and before laser pulse irradiation with (a) different average laser pulse power; (b) pulse duration extended to 1.3 ps; (c) different laser irradiation time; (d) different numbers of PEL wrapping layers.

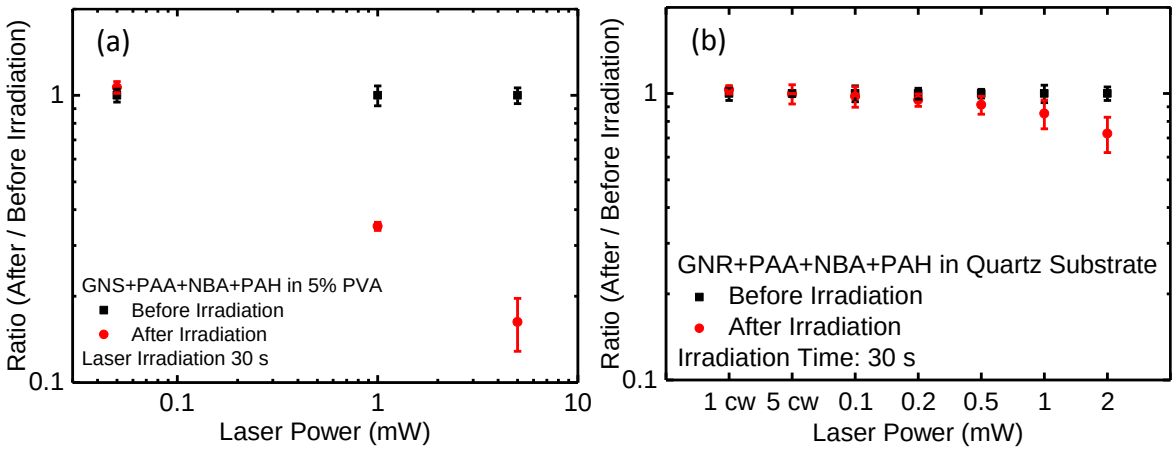

Figure 5.4 NBA SERS ratios of signal after and before laser pulse irradiation with the sample of (a) GNS+PAA+NBA+PAH in 5% PVA; (b) GNR+PAA+NBA+PAH immobilized on quartz substrate.

5.3 FUTURE WORK

Molecular release triggered by laser pulses should have the advantages of faster release rate and larger release percentage. SERS monitoring of drug release in real biomedical applications is more realistic than the centrifugation measurements in the work of Chapter 2. (1) Though we can suggest the feasibility of using SERS to quantify the molecular release due to the large distance-dependent SERS enhancement as we have tested in section 5.2, more repeats of the current experiments as well as new experiments need to be performed if we want to get more quantitative results or dig more deeply into the mechanisms of distance-dependent SERS EF. In this work, we still assumed all the reporters were at the same distance away from the GNR surface, which may not strictly follow the actual situation since we do not even know whether the first PAA layer was evenly coated around GNRs that has also been emphasized in section 3.3. During sample preparation, aggregation should be strictly avoided, since the aggregation of particles can generate SERS "hot spots" that will have SERS signals increased by orders of magnitude. (2) In the pulsed laser-triggered molecular release, it has been observed that high power laser pulses could induce SERS signal bleaching. This phenomenon limited the SERS application in this scenario, and also indicated that laser pulse can degrade loaded drug molecules. Increasing the laser power can definitely increase the release rate and percentage, but it also makes the signal bleaching worse. Expanding the laser pulse duration can decrease the temporal power intensity to reduce the possibility of signal bleaching. Though 1.3 ps is still not large enough to reduce the bleaching, longer pulse duration over 10 ps should be tested. However, if the pulse duration is too large, there might not be large enough temperature rise around the

GNRs to give a fast release rate. Above all, we need to find a proper threshold of laser power and pulse duration to ensure effective release rate and prevent signal bleaching of the molecules. In order to find the proper parameters, GNR+Raman reporters immobilized on substrates without aggregations should be prepared and the maximum laser power that won't induce signal bleaching should be figured out. Molecular release tests in solutions can only be performed under laser powers and pulse durations that won't induce signal bleaching.

5.4 MATERIALS AND METHODS

Sample Preparation: Raman reporter molecules Nile blue A perchlorate (NBA) (positively charged in neutral aqueous solution) were electrostatically wrapped in polyelectrolyte (PEL) layers (PAA M.W. 15,000 is negatively charged and PAH M.W. 15,000 is positively charged) on the surface of GNRs through layer-by-layer procedures. GNRs of aspect ratio ~4 and absorption peak ~785 nm were used here; GNSs of aspect ratio <1.2 and absorption peak ~ 520 nm were used as control. In order to control the distance of NBA from the surface of GNRs, different numbers of PEL spacer layers are designed to make samples of GNR+PAA+$(PAH+PAA)_n$+NBA+PAH (n=0,1,2,3) are prepared. In order to control the number of PEL wrapping layers, samples of GNR+PAA+NBA+PAH and GNR+PAA+NBA+PAH+PAA are prepared in aqueous solutions. All the samples are dialyzed in water for 72 hours to get rid of the unbound free NBA molecules, fresh nanopure water are replaced every 24 hours. The concentration of GNR is the final aqueous sample is kept around 2 nM.

Sample Measurement: In the measurement of distance-dependent SERS signal from GNR+NBA, the Advantage DeltaNu 785 nm Raman system was used take acquire Raman spectra of the sample. The system has a cw laser power of 45 mW and the spot size at focal plane has a radius of 15 μm. A cylindrical glass vial with the diameter of 5 mm was used as sample holder. The acquisition time is 2 s for 5 runs and the final data was the average of the 5 spectra for each sample.

In the measurement of laser pulse-induced molecular release, GNRs of concentration of 2

nM was mixed with the same volume of 10% polyvinyl alcohol (PVA M.W. 146,000~168,000) gels to get the final sample of 1 nM GNR in 5% PVA gels. Sample was well mixed through stirring and sonication and was put into a quartz cuvette of 200 μm optical path for measurement. A home-built time-resolved Raman spectroscopy with the laser mode tunable between continuous-wave and femtosecond pulsed was used for the laser irradiation and spectra acquisition. The laser spot on the sample had a radius of 4.7 um. SERS signals of NBA before and after laser pulse irradiation were taken with a 785 nm continuous-wave laser excitation at the power of ~1 mW with the acquisition time of 20 s for 3 runs, the final spectrum was the average of 3 spectra. The average power and irradiation time of the pulsed laser vary in each test. A new spot on the sample is applied in each test. The Stokes Raman peak at 590 cm^{-1} from the ring vibrational bending mode of nile blue A is the indication of number of NBA molecules on GNR surface. The SERS signals after and before laser pulse irradiation were compared.

5.5 REFERENCES

1. Huang, J.; Jackson, K. S.; Murphy, C. J. Polyelectrolyte Wrapping Layers Control Rates of Photothermal Molecular Release from Gold Nanorods. *Nano Lett.* **2012**, *12*, 2982–2987.
2. Keblinski, P.; Cahill, D. G.; Bodapati, A.; Sullivan, C. R.; Taton, T. A. Limits of Localized Heating by Electromagnetically Excited Nanoparticles. *J. Appl. Phys.* **2006**, *100*, 054305.
3. Baffou, G.; Rigneault, H. Femtosecond-Pulsed Optical Heating of Gold Nanoparticles. *Phys. Rev. B* **2011**, *84*, 035415.
4. Dreaden, E. C.; Alkilany, A. M.; Huang, X.; Murphy, C. J.; El-Sayed, M. A. The Golden Age: Gold Nanoparticles for Biomedicine. *Chem. Soc. Rev.* **2012**, *41*, 2740–2779.
5. Li, N.; Zhao, P.; Astruc, D. Anisotropic Gold Nanoparticles: Synthesis, Properties, Applications, and Toxicity. *Angew. Chem. Int. Ed.* **2014**, *53*, 1756–1789.
6. De Puig, H.; Cifuentes Rius, A.; Flemister, D.; Baxamusa, S. H.; Hamad-Schifferli, K. Selective Light-Triggered Release of DNA from Gold Nanorods Switches Blood Clotting On and Off. *PLoS ONE* **2013**, *8*, e68511.
7. Alper, J.; Crespo, M.; Hamad-Schifferli, K. Release Mechanism of Octadecyl Rhodamine B Chloride from Au Nanorods by Ultrafast Laser Pulses. *J. Phys. Chem. C* **2009**, *113*, 5967–5973.
8. Huschka, R.; Barhoumi, A.; Liu, Q.; Roth, J. A.; Ji, L.; Halas, N. J. Gene Silencing by Gold Nanoshell-Mediated Delivery and Laser-Triggered Release of Antisense Oligonucleotide and siRNA. *ACS Nano* **2012**, *6*, 7681–7691.
9. Wijaya, A.; Schaffer, S. B.; Pallares, I. G.; Hamad-Schifferli, K. Selective Release of Multiple

DNA Oligonucleotides from Gold Nanorods. *ACS Nano* **2009**, *3*, 80–86.

10. Kuo, T.-R.; Hovhannisyan, V. A.; Chao, Y.-C.; Chao, S.-L.; Chiang, S.-J.; Lin, S.-J.; Dong, C.-Y.; Chen, C.-C. Multiple Release Kinetics of Targeted Drug from Gold Nanorod Embedded Polyelectrolyte Conjugates Induced by Near-Infrared Laser Irradiation. *J. Am. Chem. Soc.* **2010**, *132*, 14163–14171.
11. Albrecht, M. G.; Creighton, J. A. Anomalously Intense Raman Spectra of Pyridine at a Silver Electrode. *J. Am. Chem. Soc.* **1977**, *99*, 5215–5217.
12. Stiles, P. L.; Dieringer, J. A.; Shah, N. C.; Van Duyne, R. P. Surface-Enhanced Raman Spectroscopy. *Annu. Rev. Anal. Chem.* **2008**, *1*, 601–626.
13. Bell, S. E. J.; Stewart, A. Quantitative SERS Methods. In *Surface Enhanced Raman Spectroscopy*; Schlücker, S., Ed.; Wiley-VCH Verlag GmbH & Co. KGaA, 2010; pp. 71–86.
14. Campion, A.; Kambhampati, P. Surface-Enhanced Raman Scattering. *Chem. Soc. Rev.* **1998**, *27*, 241–250.
15. Liu, F. M.; Köllensperger, P. A.; Green, M.; Cass, A. E. G.; Cohen, L. F. A Note on Distance Dependence in Surface Enhanced Raman Spectroscopy. *Chem. Phys. Lett.* **2006**, *430*, 173–176.
16. Shanthil, M.; Thomas, R.; Swathi, R. S.; George Thomas, K. Ag@SiO2 Core–Shell Nanostructures: Distance-Dependent Plasmon Coupling and SERS Investigation. *J. Phys. Chem. Lett.* **2012**, *3*, 1459–1464.
17. Kennedy, B. J.; Spaeth, S.; Dickey, M.; Carron, K. T. Determination of the Distance Dependence and Experimental Effects for Modified SERS Substrates Based on

Self-Assembled Monolayers Formed Using Alkanethiols. *J. Phys. Chem. B* **1999**, *103*, 3640–3646.

18. Singh, A. K.; Khan, S. A.; Fan, Z.; Demeritte, T.; Senapati, D.; Kanchanapally, R.; Ray, P. C. Development of a Long-Range Surface-Enhanced Raman Spectroscopy Ruler. *J. Am. Chem. Soc.* **2012**, *134*, 8662–8669.

19. Kovacs, G. J.; Loutfy, R. O.; Vincett, P. S.; Jennings, C.; Aroca, R. Distance Dependence of SERS Enhancement Factor from Langmuir-Blodgett Monolayers on Metal Island Films: Evidence for the Electromagnetic Mechanism. *Langmuir* **1986**, *2*, 689–694.

20. Kukushkin, V. I.; Van'kov, A. B.; Kukushkin, I. V. Long-range nature of surface-enhanced Raman scattering. *JETP Letters,* **2013**, *98*, 64-69.

21. Marotta, N. E.; Beavers, K. R.; Bottomley, L. A. Limitations of Surface Enhanced Raman Scattering in Sensing DNA Hybridization Demonstrated by Lable-Free DNA oligos as Molecular Rulers of Distance-Dependent Enhancement. *Anal. Chem.* **2013**, *85*, 1440-1446.

22. Fan, M.; Wang, P.; Escobedo, C.; Sinton, D.; Brolo, A. G. Surface-Enhanced Raman Scattering (SERS) Optrodes for Multiplexed on-Chip Sensing of Nile Blue A and Oxazine 720. *Lab. Chip* **2012**, *12*, 1554–1560.

23. Reigue, A.; Augui é, B.; Etchegoin, P. G.; Le Ru, E. C. CW Measurements of Resonance Raman Profiles, Line-Widths, and Cross-Sections of Fluorescent Dyes: Application to Nile Blue A in Water and Ethanol. *J. Raman Spectrosc.* **2013**, *44*, 573–581.

24. Sivapalan, S. T.; Vella, J. H.; Yang, T. K.; Dalton, M. J.; Haley, J. E.; Cooper, T. M.; Urbas, A. M.; Tan, L.-S.; Murphy, C. J. Off-Resonant Two-Photon Absorption Cross-Section

Enhancement of an Organic Chromophore on Gold Nanorods. *J. Phys. Chem. Lett.* **2013**, *4*, 749–752.

25. Sivapalan, S. T.; DeVetter, B. M.; Yang, T. K.; Schulmerich, M. V.; Bhargava, R.; Murphy, C. J. Surface-Enhanced Raman Spectroscopy of Polyelectrolyte-Wrapped Gold Nanoparticles in Colloidal Suspension. *J. Phys. Chem. C* **2013**, *117*, 10677–10682.
26. Huang, J.; Park, J.; Wang, W.; Murphy, C. J.; Cahill, D. G. Ultrafast Thermal Analysis of Surface Functionalized Gold Nanorods in Aqueous Solution. *ACS Nano* **2013**, *7*, 589–597.
27. Sivapalan, S. T.; DeVetter, B. M.; Yang, T. K.; van Dijk, T.; Schulmerich, M. V.; Carney, P. S.; Bhargava, R.; Murphy, C. J. Off-Resonance Surface-Enhanced Raman Spectroscopy from Gold Nanorod Suspensions as a Function of Aspect Ratio: Not What We Thought. *ACS Nano* **2013**, *7*, 2099–2105.
28. Frontiera, R. R.; Henry, A.-I.; Gruenke, N. L.; Van Duyne, R. P. Surface-Enhanced Femtosecond Stimulated Raman Spectroscopy. *J. Phys. Chem. Lett.* **2011**, *2*, 1199–1203.